

Design and Implementation of Components for
Renewably-Powered Base-Stations with Heterogeneous
Access Channel

PhD Thesis

Vianney Anis

Centre for excellence in Signal and Image Processing
Department of Electronic and Electrical Engineering
University of Strathclyde, Glasgow

June 25, 2021

This thesis is the result of the author's original research. It has been composed by the author and has not been previously submitted for examination which has led to the award of a degree.

The copyright of this thesis belongs to the author under the terms of the United Kingdom Copyright Acts as qualified by University of Strathclyde Regulation 3.50. Due acknowledgement must always be made of the use of any material contained in, or derived from, this thesis.

Signed:

Date: June 25, 2021

Abstract

Providing high-speed broadband services in remote areas can be a challenging task, especially because of the lack of network infrastructure. As typical broadband technologies are often expensive to deploy, they require large investment from the local authorities. Previous studies have shown that a viable alternative is to use wireless base stations with high-throughput point to point (PTP) backhaul links. With base stations comes the problem of powering their systems, it is tackled in this thesis by relying on renewable energy harvesting, such as solar panels or wind turbines. This thesis, in the context of the sustainable cellular network harvesting ambient energy (SCAVENGE) project, aims to contribute to a reliable and energy efficient solution to this problem, by adjusting the design of an existing multi-radio energy harvesting base station.

In Western Europe, 49 channels of 8 MHz were used for analogue TV transmissions, ranging from 470 MHz (Channel 21) to 862 MHz (Channel 69); this spectrum, now partially unused due to the digital television (DTV) switch-over, has been opened to alternative uses by the regulatory authorities. Using this newly freed ultra high frequency (UHF) range, also known as TV white space (TVWS), can offer reliable low-cost broadband access to housings and businesses in low-density areas. While UHF transmitters allow long range links, the overcrowding of the TV spectrum limits the achievable throughput; to increase the capacity of such TVWS rural broadband base station the UHF radio has previously been combined with a lower-range higher-throughput GHz radio like Wireless Fidelity (WiFi).

From the regulatory constraints of TVWS applications arises the need for frequency-agile transceivers that observe strict spectral mask requirements, this guided previous works towards discrete Fourier transform (DFT) modulated filter-bank multi-carrier (FBMC) systems. These systems are numerically efficient, as they permit the up-and-down conversion of the 40 TV channels at the cost of a single channel transceiver and the modulating transform. Typical implementations rely on power-of-two fast Fourier transforms (FFTs); however the smallest transform covering the full

40 channels of the TVWS spectrum is a 64 points wide, thus involving 24 unused channels. In order to attain a more numerically-efficient implemented design, we introduce the use of mixed-radix FFTs modulating transform. Testing various sizes and architectures, this approach provides up to 6.7% of energy saving compared to previous designs.

Different from orthogonal frequency-division multiplexing (OFDM), FBMC systems are generally expected to be more robust to synchronisation errors, as oversampled FBMC systems can include a guard band, and even in a doubly-dispersive channel, inter-carrier interference (ICI) can be considered negligible. Even though sub-channels can be treated independently—i.e. without the use of cross-terms—they still require equalisation. We introduce a per-band equalisation, amongst different options, a robust and fast blind approach based on a concurrent constant modulus (CM)/decision directed (DD) fractionally-space equaliser (FSE) is selected. The selected approach is capable of equalising a frequency-selective channel. Furthermore the proposed architecture is advantageous in terms of power consumption and implementation cost.

After focussing on the design of the radio for TVWS transmission, we address a multi-radio user assignment problem. Using various power consumption and harvesting models for the base station, we formulate two optimisation problems, the first focuses on the base station power consumption, while the second concentrates on load balancing. We employ a dynamic programming approach to optimise the user assignment. The use of such algorithms could allow a downsizing of the power supply systems (harvesters and batteries), thus reducing the cost of the base station. Furthermore the algorithms provide a better balance between the number of users assigned to each network, resulting in a higher quality of service (QoS) and energy efficiency.

Contents

Abstract	ii
Contents	iv
Abbreviations	viii
List of Symbols	xiii
List of Figures	xviii
List of Tables	xxii
List of Publications	xxiii
Acknowledgements	xxiv
1 Introduction	1
1.1 Scenario and Motivation	1
1.1.1 Legacy Broadband Access Solutions	1
1.1.2 Wireless Broadband for Rural Areas	2
1.2 Problem Statement	3
1.3 Contributions	5
1.3.1 Baseband Unit Implementation	5
1.3.2 Multi-Radio Network User Assignment	5
1.4 Thesis Overview	6
2 Background	7
2.1 TV White Space for Rural Broadband	7
2.2 Software Defined Radio Implementation	9
2.2.1 FPGA Architecture	9
2.2.2 Zynq SDR	13

2.2.3	MATLAB [®] hardware (HW)/software (SW) Co-Design Workflow	14
2.3	Oversampled FFT Modulated FBMC	16
2.3.1	System Description	16
2.3.2	Design Example	20
2.4	Equalisation for Oversampled FFT Modulated FBMC for TVWS Operation	21
2.4.1	Equalisation for Multi-Carrier System	21
2.4.2	Constant Modulus Equalisation	22
2.5	Multi-Radio Base Station User Assignment	25
2.6	Chapter Summary	26
3	FFT Size Optimisation for Oversampled FFT Modulated FBMC Systems	27
3.1	Motivation and Rationale	27
3.2	FFT Design for FBMC Systems	28
3.2.1	40 Point FFT	29
3.2.2	Radix-5 FFT Block	30
3.2.3	Complexity	34
3.3	Filter Design	35
3.3.1	Stage 1 Filter	35
3.3.2	Stage 2 Filter	37
3.4	FPGA Implementation	38
3.4.1	Word-Length Considerations	39
3.4.2	Serialisation of the Filters	40
3.4.3	Transform Structure	41
3.5	Results	44
3.5.1	System Performance	44
3.5.2	Footprint	48
3.5.3	Power Consumption	49
3.6	Chapter Summary and Conclusions	50
4	Per-Band Equalisation for Oversampled FBMC Systems	51
4.1	Motivation and Rationale	51
4.2	Equaliser Design	53
4.2.1	Equaliser Structure	53
4.2.2	Concurrent Constant Modulus / Decision Directed Algorithm	54
4.3	FPGA Implementation	56
4.3.1	Word-Length Considerations	56

4.3.2	Step Size Representation	57
4.4	Results	57
4.4.1	Performances	57
4.4.2	Footprint	58
4.4.3	FPGA Timing Constraints	59
4.4.4	Power Consumption	60
4.5	Chapter Summary and Conclusions	61
5	Multi-Radio Access Network Assignment	62
5.1	Motivation and Rationale	62
5.2	Base Station Design	64
5.2.1	Radio Systems	64
5.2.2	Power Supply and Storage	65
5.2.3	Control System	65
5.3	Models	66
5.3.1	Time Keeping	66
5.3.2	Network Model	66
5.3.3	Power Consumption Model	70
5.3.4	Power Generation and Storage Models	73
5.4	Load Focussed Optimisation	75
5.4.1	Resources Optimisation	75
5.4.2	Reformulation for Dynamic Programming	77
5.4.3	Cost Function	78
5.4.4	Transition Penalty Function	79
5.5	Energy/Load Balanced Optimisation	80
5.5.1	Optimisation Problem	80
5.5.2	Reformulation for Dynamic Programming	81
5.5.3	Cost Function	81
5.5.4	Transition Penalty Function	82
5.6	Dynamic Programming	83
5.6.1	Algorithm	83
5.6.2	Cost Aggregation	83
5.6.3	Optimum GHz Range Selection	84
5.7	Load/Energy Balanced Approach: Results	84
5.7.1	Test Scenarios and Methodology	84
5.7.2	Results and Analysis	85
5.8	Load Focussed Approach: Results	87

5.8.1	Test Scenarios and Methodology	87
5.8.2	Result and Analysis	89
5.9	Chapter Summary and Conclusions	97
6	Conclusions & Future Work	98
6.1	Thesis Summary	98
6.1.1	FFT Size Optimisation for FBMC Systems	98
6.1.2	Per-Band Equalisation for Oversampled FBMC Systems	99
6.1.3	Multi-Radio Access Network Assignment	99
6.2	Future Work	99
	References	102

Abbreviations

ADC analogue-to-digital converter

ADSL asymmetric digital subscriber line

ARM advance reduced instruction set computing (RISC) machine

AGWN additive white Gaussian noise

BER bit error rate

CM constant modulus

CPLD complex programmable logic device

DAC digital-to-analogue converter

DD decision directed

DFT discrete Fourier transform

DSP digital signal processor

DTV digital television

FBMC filter-bank multi-carrier

FDD frequency division duplex

FFT fast Fourier transform

FIFO first-in first-out

FIR finite impulse response

FPGA field programmable gates array

FSE fractionally-space equaliser

HDL hardware description language

HW hardware

I²C inter-integrated circuit

IC integrated circuit

ICI inter-carrier interference

ISI inter-symbol interference

ICT information and communications technology

IF intermediate frequency

I/O input/output

LMS least mean square

LUT look-up table

MAC multiplication-accumulation

MSE mean squared error

NGA next generation access

OfCom office of communications

OFDM orthogonal frequency-division multiplexing

OQAM offset-quadrature amplitude modulation

PMSE programme-making and special events

PPF polyphase filter

PSD power spectral density

PSK phase-shift keying

PTMP point to multi-points

PTP point to point

QAM quadrature amplitude modulation

QoS quality of service

QPSK quadrature phase-shift keying

RAM random access memory

RAN radio access network

RAT radio access technology

RF radio frequency

RFSoC radio frequency system on chip

RISC reduced instruction set computing

ROM read-only memory

Rx receiver

SCAVENGE sustainable cellular network harvesting ambient energy

SDR software defined radio

SNR signal-to-noise ratio

SoC system on chip

SQNR signal-to-quantization-noise ratio

SW software

TVWS TV white space

Tx transmitter

UHF ultra high frequency

UK United Kingdom

USRP universal software radio peripheral

VHDL very high speed integrated circuit (VHSIC) HDL

VHSIC very high speed integrated circuit

WiFi Wireless Fidelity

List of Symbols

Sets

\mathbb{C} Set of complex numbers

\mathbb{R} Set of real numbers

\mathbb{R}^+ Set of positive real numbers, such as $0 \in \mathbb{R}^+$

\mathbb{Z} Set of integers

\mathbb{N} Set of non-negative integers

$\{a, b, \dots, z\}$ Set including the listed elements

Constants

c Speed of light

Operators and functions

$f : X \rightarrow Y$ Definition of a function f which maps elements x of a set X
 $x \mapsto f(x)$ to corresponding images $f(x)$ in a set Y

$x \mapsto f(x)$ Map an element x to an image $f(x)$

$X \rightarrow Y$ Map a set X to a set Y

e^{\square} Exponential function

$e^{j\square}$ Complex exponential function

$\text{Re}\{z\}$ Real part of a $z \in \mathbb{C}$

$\text{Im}\{z\}$ Imaginary part of a $z \in \mathbb{C}$

\square^* Complex conjugate operator

\square^T Transposition operator

\square^H Hermitian transpose operator

$\nabla \square$ Nabla operator, gradient or first order derivative

$\frac{\partial f(x)}{\partial x}$ Partial derivative of f in x

$\Delta \square$ Laplace operator, second order derivative $\Delta \square = \nabla \cdot \nabla \square$

$\square \cdot \square$ Dot-product

$E\{\square\}$ Expectation operator

Block Diagram

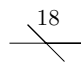
 Antenna

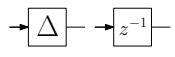
 Power amplifier

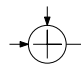
 Analog filter

 analogue-to-digital converter (ADC)

 digital-to-analogue converter (DAC)

 Digital bus of width 18 bits

 Delay operation, Δ single delay, z^{-k} k samples delay

 Adder

 Multiplier

 Logic and arithmetic processing unit

 Downsampling operation, here factor 2

 Upsampling operation, here factor 2

Signals Chapters 2, 3 and 4

f Frequency

n, ν, l Discrete time indexes

$\square^{(i)}$ Used to denote variations of designs

$h_a^{(i)}[l], p_a^{(i)}[l]$ Prototype filter, time domain

$H_a^{(i)}(z), P_a^{(i)}(z)$ Prototype filter, z -domain

\mathbf{w} Equaliser filter coefficient vector

$\mathbf{w}_{m,i}[n]$ Equaliser filter coefficient vector, for channel m and phase number i in a polyphase structure at time index n

R Wordlength

R_{rx} Wordlength at the ADC in the receiver

R_a Wordlength in stage $a \in \{1, 2, 3\}$

Constants Chapters 2, 3 and 4

f_s or F_s Sampling frequency

Ω_c Constant phase value in radians

$K_a^{(i)}$ Oversampling factor for stage $a \in \{1, 2, 3\}$ of the FBMC system in design (i)

$L_a^{(i)}$ Filter length for stage $a \in \{1, 2, 3\}$ of the FBMC system in design (i)

$B_{\text{T},a}^{(i)}$ Transition band for the filter in stage $a \in \{1, 2, 3\}$ in design (i)

γ Target CM for a CM equaliser

μ, μ_{CM} or μ_{DD} Step-size for equalisers, CM and DD for CM and DD algorithms respectively

Variables Chapter 5

t Global time index

δ_t Discrete time increment

τ Local time index

m, d, h Indexes used to count months, days within month and hours within day and decompose global time to the different required time scales

$r(t)$ Function that sets the reach of the base station at a time t

- $X_S(m, d)$ Random variable, total amount of solar energy harvested on a day d of month m , one time step δ_t
- $X_W(m, d)$ Random variable, amount of wind energy harvested at noon on day d of month m , one time step δ_t
- $E_S(t)$ Amount of solar energy harvested during time step t
- $E_W(t)$ Amount of wind energy harvested during time step t
- $E_B(t)$ Amount of energy stored into battery at end of time step t
- $E_{BS}(t)$ Amount of energy consumed by base station during time step t
- $N_{UHF}(t, r(t))$ Number of user allocated to the UHF network at time t given an assignment function $r(t)$
- $N_{GHz}(t, r(t))$ Number of user allocated to the GHz network at time t given an assignment function $r(t)$
- $N_a(t)$ Number of active users at time t
- $C(t)$ Cost space corresponding to a 24-hour window centred on time t for the dynamic programming algorithm
- $c_{\tau, n}(t)$ Coefficient corresponding to state (τ, n) of cost space $C(t)$
- $C^{\text{power}}(t)$ Power balance related cost space
- $c_{\tau, n}^{\text{power}}(t)$ Coefficient corresponding to state (τ, n) of cost space $C^{\text{power}}(t)$
- $C^{\text{load}}(t)$ Power balance related cost space
- $c_{\tau, n}^{\text{load}}(t)$ Coefficient corresponding to state (τ, n) of cost space $C^{\text{load}}(t)$
- $P^{\text{up}}(t)$ Penalty matrix associated to an increase of reach between time τ and $\tau + 1$
- $P^{\text{down}}(t)$ Penalty matrix associated to a decrease of reach between time τ and $\tau + 1$
- $\hat{C}(t)$ Aggregated cost space
- $\hat{C}^{(+)}(t)$ Aggregated cost space in positive time
- $\hat{C}^{(-)}(t)$ Aggregated cost space in negative time
- $\nu(t)$ TVWS load factor time t , performance metric

Constants Chapters 5

K Number of time steps δ_t in 12 hours

$D(m)$ Function that returns the number of days in the month number m

$\Gamma(\alpha)$ Gamma function

σ_i Standard deviation of normal distribution

α_B Battery self-discharge coefficient

η_B Energy conversion systems efficiency

$N_{\text{UHF,max}}$ Maximum number of user allocated to the UHF network for acceptable performance

A Set of all possible $r(t)$ functions

List of Figures

1.1	Survey of broadband QoS, office of communications (OfCom) (2014) [10].	2
1.2	Multi-network access scenario, as presented in [28].	4
2.1	TV spectrum after switch-over for the UK in 2009, Ofcom [22].	8
2.2	Ofcom spectral requirements for n^{th} channel [22].	8
2.3	Early FPGA architecture, including look-up table (LUT), input/outputs (I/Os) and interconnection network.	9
2.4	Modern FPGA architecture including LUT, I/Os, high speed I/Os, multipliers, digital signal processor (DSP) blocks, random access memory (RAM), advance RISC machine (ARM) core, peripherals and interconnection network.	11
2.5	Simplified block diagram of the DSP48E1 from the series 7 Xilinx field programmable gates arrays (FPGAs).	12
2.6	Zynq SDR system architecture, based on a Xilinx ZC706 and Analog Devices AD-FMCOMMS4 evaluation boards.	13
2.7	Mathworks software defined radio (SDR)HW/SW co-design work-flow, use-cases (a), (b) and (c).	15
2.8	Zynq SDR considered system architecture	16
2.9	Two-stage TVWS filter-bank transmitter (Tx) (above) and receiver (Rx) (below) with a polyphase filter (PPF) in stage 1 and an FBMC system in stage 2, as proposed in [54].	17
2.10	Stage 1 filter $h_1^{(i)}[\ell]$; the transition bandwidth $B_{T,1}^{(i)}$ depends on the decimation ratio $K_1^{(i)}$ as described in [54].	18
2.11	Stage 2 prototype filter with passband width of 8 MHz as described in [54].	18
2.12	Downconversion, equivalence between a simple finite impulse response (FIR) filter followed by a downsampler and a polyphase network down-converter.	19
2.13	Filter design prototype for stage 1 FBMC system as described in [1].	20
2.14	Filter design prototype for stage 2 FBMC system as described in [1].	20

2.15	Power spectral density (PSD) of signals after stage 1 using bit-true and cycle-accurate simulations as described in [1].	21
2.16	PSD of signals after stage 2 using bit-true and cycle-accurate simulations as described in [1].	21
2.17	Constant modulus equaliser block diagram.	22
2.18	CM algorithm output equalising a quadrature phase-shift keying (QPSK) constellation submitted to a channel introducing inter-symbol interference (ISI) only.	24
2.19	Effect of frequency offset on the CM algorithm equalising a QPSK constellation.	25
3.1	40 point mixed-radix FFT, build by cascading radix-5 and radix-8 FFTs in a fully parallel structure.	30
3.2	Radix-5 FFT implemented using purely real or imaginary gains as presented in [94].	34
3.3	Stage 1 filter 64-point FFT FBMC frequency response $ H_1(e^{j2\pi f/f_s}) $ and corresponding spectral mask.	36
3.4	Stage 1 filter 40-point FFT FBMC frequency response $ H_1(e^{j2\pi f/f_s}) $ and corresponding spectral mask.	36
3.5	Stage 2 filter 64-point FFT FBMC frequency response $ P_2(e^{j2\pi f/f_s}) $. . .	38
3.6	Stage 2 filter 40-point FFT FBMC frequency response $ P_2(e^{j2\pi f/f_s}) $. . .	39
3.7	Oversampled FFT modulated FBMC system, as implemented in this work.	39
3.8	Implementation of a 4-tap direct-form FIR filter.	40
3.9	Implementation of a 4-tap FIR filter serialised by a factor of 4.	41
3.10	Unserialised FBMC synthesis bank.	42
3.11	Unserialised FBMC analysis bank.	43
3.12	Serialised 40-point mixed-radix FFT.	44
3.13	PSD after stage 1 in 40-point system, all available channels active. . . .	45
3.14	PSD after stage 1 in 64-point system, all available channels active. . . .	45
3.15	PSD after stage 2 in 40-point system, 1 active channel.	46
3.16	PSD after stage 2 in 64-point system, 1 active channel.	46
3.17	PSD after stage 2 in 40-point system, 8 active channels.	47
3.18	PSD after stage 2 in 64-point system, 8 active channels.	47
3.19	Area usage on Zynq Z7045, are displayed the main type of resources: LUT, flip-flops, DSP48E1 and RAM blocks.	48
3.20	Dynamic power consumption estimate, for each of the proposed designs.	50

4.1	Example of impact of radio frequency (RF) delays of (a) 0, (b) 96, (c) 192, (d) 288, and (e) 384 samples on the impulse response of a transceiver system subchannel impulse response.	52
4.2	Transmission over the m th subchannel $f_m[n]$	53
4.3	$T/3$ -spaced subchannel equaliser with carrier frequency and phase correction, and decision device.	53
4.4	Results for FSE-CM/DD adaptive algorithm, showing ensemble-averaged errors for different signal-to-noise ratios (SNRs).	58
4.5	Dynamic power consumption of different equalisers.	60
5.1	Multi-radio off-grid base station, system block diagram.	64
5.2	Multi-network access scenario, a community is served by a single base station located at the centre of the village.	67
5.3	Half-normal spatial distributions of users, with respect to their distance from the base station.	68
5.4	Multi-radio base station located on the side of the community.	68
5.5	Gamma spatial distributions of users, with respect to their distance from the base station.	69
5.6	Mean load variation throughout the day, Tiree [19] and Maier [107] models.	70
5.7	GHz radio power consumption for a given maximum reach from the base station.	72
5.8	Average daily energy generation on Tiree, Scotland [19].	73
5.9	Sun power generation variation, average instant power against the time of the day.	74
5.10	Set of the achievable states by the base station depending on the selected reach r	77
5.11	Two days simulation in January at full harvesting capacity.	85
5.12	Mean hourly GHz network reach on a day in January and July under full and reduced harvesting capacity.	86
5.13	Mean GHz radio power consumption.	86
5.14	Average numbers of TVWS users.	87
5.15	Community size: battery level, (i) 10% lower percentile with a TVWS only base station, (ii) lower percentile with the WiFi network at full power, (iii) mean battery level under optimisation and (iv) 90% percentiles under optimisation.	90

5.16	Community size: TVWS network load factor $\nu(t)$ over the course of a day, (i) 90% upper percentile with a TVWS only base station, (ii) 90% upper percentile with the WiFi network at full power, (iii) mean under optimisation and (iv) 90% percentiles under optimisation.	91
5.17	User distributions: battery level, (i) 10% lower percentile with a TVWS only base station, (ii) lower percentile with the WiFi network at full power, (iii) mean battery level under optimisation and (iv) 90% percentiles under optimisation.	92
5.18	User distributions: evolution of the TVWS network load factor $\nu(t)$ over the course of a day, (i) 90% upper percentile with a TVWS only base station, (ii) 90% upper percentile with the WiFi network at full power, (iii) mean under optimisation and (iv) 90% percentiles under optimisation.	93
5.19	Harvesters performances: battery level, (i) 10% lower percentile with a TVWS only base station, (ii) lower percentile with the WiFi network at full power, (iii) mean battery level under optimisation and (iv) 90% percentiles under optimisation.	95
5.20	Harvesters performances: evolution of the TVWS network load factor $\nu(t)$ over the course of a day, (i) 90% upper percentile with a TVWS only base station, (ii) 90% upper percentile with the WiFi network at full power, (iii) mean under optimisation and (iv) 90% percentiles under optimisation.	96

List of Tables

2.1	FPGA resources Xilinx Zynq Z7045 used inChapter 3, and Virtex 7 7VX550T targeted in Chapter 4.	13
3.1	Stage 1 filter characteristics	35
3.2	Oversampled FFT modulated FBMC, FPGA area footprint, Xilinx Z7045.	49
4.1	Resources requirements CM algorithm, Virtex 7 7VX550T.	59
4.2	Resources requirements FSE-CM, Virtex 7 7VX550T.	59
4.3	Resources requirements CM/DD, Virtex 7 7VX550T.	59
4.4	Resources requirements FSE-CM/DD, Virtex 7 7VX550T.	60
5.1	User spatial distributions parameters.	69
5.2	Power consumption model parameters extracted from [28].	72

List of Publications

1. V. Anis, C. Delaosa, L. H. Crockett, and S. Weiss, “Energy-efficient implementation of a wideband transceiver system with per-band equalisation and synchronisation,” in *2018 IEEE Wireless Communications and Networking Conference*, (Barcelona, Spain), pp. 1–6, Apr. 2018
2. V. Anis, J. Guo, S. Weiss, and L. Crockett, “FPGA Implementation of a TVWS Up- And Downconverter Using Non-Power-of-Two FFT Modulated Filter Banks,” in *2019 27th European Signal Processing Conference (EUSIPCO 2019)*, Sept. 2019
3. V. Anis and S. Weiss, “Multi-Radio Access Network Assignment Using Dynamic Programming,” in *The 27th International Conference on Software, Telecommunications and Computer Networks (SoftCOM 2019)*, Sept. 2019
4. Scavenge-Consortium, *D2.1-WP2 Energy Models: Intermediate Report*. Feb. 2018
5. Scavenge-Consortium, *D2.2-WP2 Energy Models: Final Report*. Dec. 2019
6. Scavenge-Consortium, *D4.1-WP4 Resources Optimisation: Intermediate Report*. Feb. 2018
7. Scavenge-Consortium, *D4.2-WP4 Resources Optimisation- Final Report*. Aug. 2019

Acknowledgements

This work has received funding by the European Union Horizon 2020 research and innovation programme under the Marie Skłodowska-Curie grant agreement No 675891 (SCAVENGE).

I would like to express my gratitude to Prof. Stephan Weiss for his encouragements and support throughout both my PhD and the SCAVENGE project. I would also like to thank all the members of the SCAVENGE project, both students and supervisory team, with whom I enjoyed meeting and collaborating with. More specifically are to be noted the immense help of Ibrahim Fawaz, with whom I co-managed a workpackage for the project, but also Dr Marco Miozzo and Dr Paolo Dini from CTTC for the support they both provided as workpackage and project coordinators respectively.

I must also mention the people at the Toshiba Bristol Innovation and Research Laboratory (BRIL) for welcoming me during my secondment in the context of the SCAVENGE project, providing me with very useful insight with regards to my implementation work. I must also thank Toshiba for offering me the opportunity of becoming a full-time employee at BRIL and being supportive while I worked toward finishing my PhD.

I would also like to acknowledge the Glasgow branch of Mathworks and its employees, I had the chance to work with as an intern. They provided me with experience useful both toward the completion of my PhD and my future career.

I was very fortunate to meet many friendly and inspiring individuals from the university, the SCAVENGE consortium and the research community in signal processing and communication systems, which all provided me great advice, encouragements and support.

Chapter 1

Introduction

1.1 Scenario and Motivation

While information and communications technologies (ICTs) are responsible for an increasing share in the world's electrical energy usage [8], a large part of the population still has no or only limited access to the internet [9]. This is true even in economically developed countries, such as the United Kingdom (UK) [10], where rural communities only benefit from low quality, low throughput broadband services, mainly because of economic constraints on the infrastructures, or the lack thereof [11, 12]. The work presented in this thesis aims to explore reliable and energy efficient solutions to this problem, in the context of the sustainable cellular network harvesting ambient energy (SCAVENGE) project. The SCAVENGE project is a Horizon 2020, Marie Skłodowska Curie Action innovative training network (grant agreement number: 675891), whose main objective is to tackle sustainable design, protocols, architectures and algorithms for next generation 5G cellular networks. The overall purpose of the SCAVENGE project is to allow mobile systems and especially their constituent base stations, femto, small-cells, mobile devices and sensors to take advantage of sources harvesting ambient energy (such as renewable sources).

1.1.1 Legacy Broadband Access Solutions

Broadband access is typically provided using asymmetric digital subscriber line (ADSL) technology. The service is distributed countrywide on an optical fibre network, and is then dispatched locally through the legacy copper twisted pair telephone network. In small isolated communities, the deployment of such technology is often deemed too expensive to be economically viable and is usually not profitable for service providers. While other technologies such as satellite broadband solutions are available, they often come at high set-up and operation costs; rural broadband is then largely subsidised by

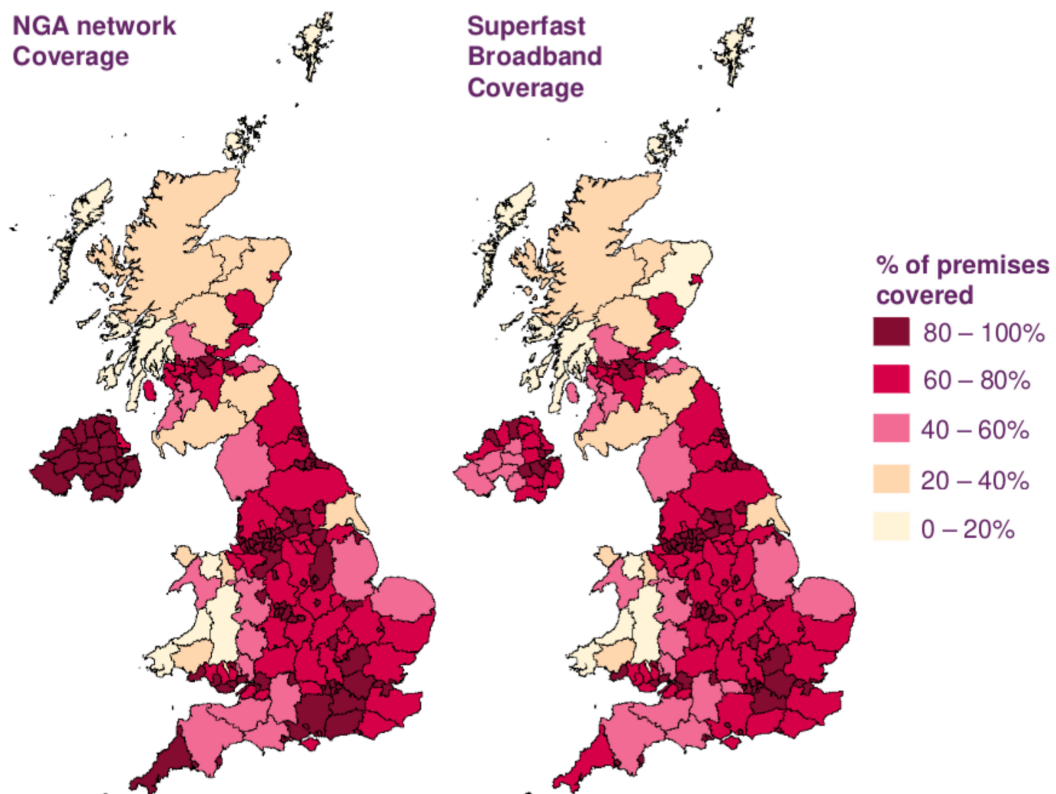


Figure 1.1: Survey of broadband QoS, OfCom (2014) [10].

the local authorities. In addition to the cost and challenges of the communication network deployment, issues with the access to electricity, or the reliability of the electrical power supply can represent further complications.

The quality of service (QoS) of broadband access in rural areas is often limited, and reliable access can be very challenging. Figure 1.1 presents the coverage offered in the UK by next generation access (NGA) and superfast broadband [13]; the rural parts of the UK such as Scotland exhibit low to very low QoS, with office of communications (OfCom) data showing that fast broadband reaching less than 50% of the households in some areas, when modern life requires high quality broadband both for businesses and individual users.

1.1.2 Wireless Broadband for Rural Areas

A viable solution for rural broadband is to use wireless base stations with a wireless high-throughput point to point (PTP) backhaul links [14]. The suitability of wireless technologies for rural broadband has been studied in developing territories [15–18]

and developed countries [14, 19, 20], both from technical and economical standpoints. Technologies such as Wireless Fidelity (WiFi) are commonly used for broadband access, providing cheap access to the internet both in urban and rural environments. Additionally to WiFi, several wireless technologies were proposed in the context of rural broadband access, including TV white space (TVWS) approaches [19, 21]. The use of TVWS has been strongly motivated by the spectrum release that followed the digital television (DTV) switch-over in numerous countries such as the UK [22]. This newly available spectrum, referred as TVWS, offers opportunities for new applications such as programme-making and special events (PMSE) devices and mobile networks to which channels above 700 MHz have been reassigned [23]. The use of TVWS for broadband access is especially interesting in rural areas, where broadband QoS is low and few TV channels are used. Using a TVWS network in those low-density areas can offer reliable low-cost internet access to housings and businesses [19].

Adding to the network access issues, an unavailable or unreliable power grid at the base station site can represent further challenges and costs. An adequate solution to deal with this issue is the introduction of energy harvesters [24–26]. The use of renewable energy harvesting, however, strongly affects the available power, as explored in the context of the SCAVENGE project [4, 5]. Two approaches for the power systems are then possible: either the energy system needs to be over-dimensioned as in [19], or resource management has to be introduced [6, 7, 27].

1.2 Problem Statement

The scenario presented in Section 1.1 comes with its own set of challenges. Such remote off-grid base stations have already been implemented on the isles of Bute and Tiree using off-the-shelf radios [19], which while they simplify the design of the base station, might not achieve the best possible balance between high throughput and low power consumption. In energy harvesting communication networks, the available electrical power is a critical resource, which has to be used carefully [4–7]. Due to these constraints, an off-grid wireless base station then requires radio systems with low power consumption, while still meeting the legal requirements for transmission and offering a satisfactory broadband service to the end users.

To provide broadband in remote areas, previous studies [14–18, 20] used wireless base stations which have been successfully powered by various energy harvesters. The

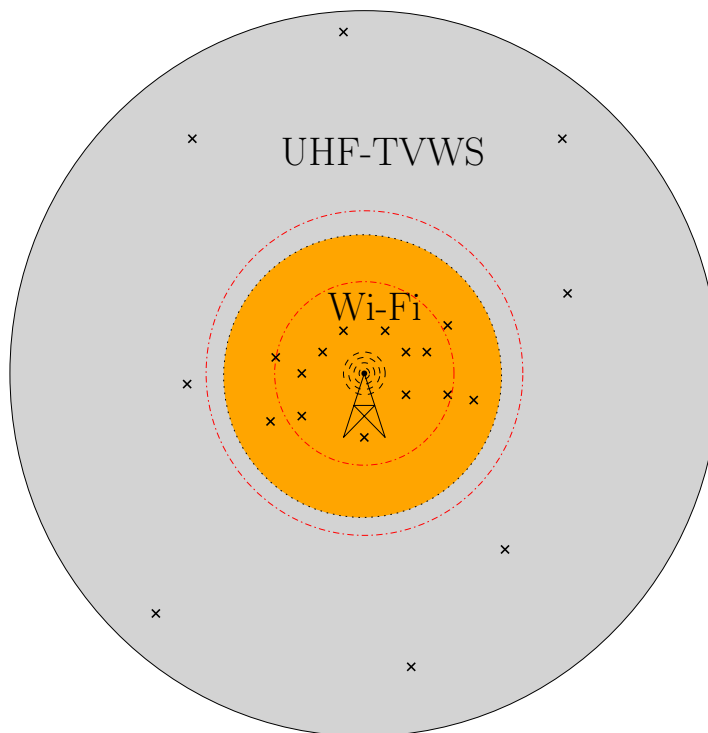


Figure 1.2: Multi-network access scenario, as presented in [28].

broadband access solution proposed by [19] and explored further in this thesis relies on the concurrent use of WiFi and TVWS radio access networks (RANs). While a ultra high frequency (UHF), e.g. TVWS, transmitter allows a longer link than a GHz radio, e.g. WiFi, at a comparable transmission power, due to the better propagation characteristics of the lower frequencies [29], the overcrowding of the TV spectrum [30] limits the achievable throughput by TVWS technologies, thus justifying the addition of a GHz radio to the base station to improve QoS.

Transmissions in the TVWS frequency bands require frequency-agile and/or easily reconfigurable radio systems with very low out of band emissions [22]. These characteristics are needed because the available spectrum varies in time, space and frequency, additionally the TVWS transmission should not interfere with the TV services. As depicted in Figure 1.2 and detailed in Chapter 5, the user spatial distribution in rural environments into the form of clusters, villages, surrounded by sporadically placed users renders the rural area well suited for the use of multiple radio access technologies (RATs) taking advantage of the different propagation characteristics, thus allowing to serve both the close-by and farther away users, while providing good data rates [28]. The use of multiple radios provides an opportunity for optimisation; several studies

showed that energy savings and QoS improvements are achievable by optimising the user assignment in heterogeneous network scenarios [31, 32].

1.3 Contributions

In this thesis two main research challenges are presented. The first is to contribute to the design of a low-power baseband unit for TVWS broadband access, focussing successively on a multi-carrier and equaliser implementation on a software defined radio (SDR) platform. The second challenge is to extend the optimisation of the power efficiency of the base station further, by using a multi-radio user assignment system, between two RANs in order to reduce the power consumption of the base station, while maintaining QoS.

1.3.1 Baseband Unit Implementation

The contributions of this thesis focus on two main aspects of base-band processing, the multi-carrier system and the equalisation. For the first, this thesis focusses on over-sampled fast Fourier transform (FFT) modulated filter-bank multi-carrier (FBMC) systems, more specifically considering the design of the modulating transform; for the second, a concurrent constant modulus (CM) / decision directed (DD) fractionally-space equaliser (FSE) is proposed. All implementations were performed using a SDR approach [33, 34], in a Matlab hardware (HW)/software (SW) co-design environment [35]. This thesis aims to standardise simulation, implementation and testing methodologies, providing the first steps toward the implementation of a full transceiver system. Each field programmable gates array (FPGA) implementation is complemented by a power consumption analysis using the Xilinx Vivado tools [36]; these results are then used, conjointly with the other metrics, to determine the best-suited design for a low-power rural broadband access base station.

1.3.2 Multi-Radio Network User Assignment

Previous work [24–26] introduced the use of renewable energy to tackle both planning issues and access to electrical power, as the best base station site might be outside the reach of the electrical grid. Two approaches are then possible to maintain service: either the energy system needs to be over-dimensioned [19] or resource management has to be introduced [27]. Various resource management techniques have been proven effective in energy harvesting networks [6, 7, 31, 32, 37]; the problem considered in this work was previously optimised using a load-focussed user assignment optimisation

algorithm based on a belief propagation algorithm [28].

To treat this multi-radio user assignment problem, two approaches are chosen, using various power consumption and production models for the base station presented in [21], corresponding optimisation problems are formulated and then submitted to a dynamic programming algorithm. The overall energy savings are then compared by way of simulations taking into consideration the variation in harvested energy, as well as changes in user activity, against scenarios in which the WiFi radio is set to the maximum legal transmission power, or in which the base station uses a single TVWS radio to provide the entire community with broadband.

1.4 Thesis Overview

The background for the work presented in this thesis is introduced in Chapter 2, which describes the rules for TVWS transmission, as defined by OfCom, as well as design constraints and techniques used throughout this thesis for SDR implementation. The chapter also introduces an oversampled FFT modulated FBMC system, and equalisation techniques for FBMC systems, as well as the user assignment problem of a multi-RAT base station for rural broadband access. In Chapter 3, a novel approach in the implementation of FFT-modulated FBMC systems is described, which moves away from typical power-of-two implementation of the discrete Fourier transform (DFT), in order to only up/down-convert the required number of channels, i.e. 40, to cover the entirety of the TVWS spectrum. In Chapter 4, an energy efficient equalisation techniques for FPGA implementation is detailed, making concurrent use of CM and DD coefficient update processes. In Chapter 5, a new approach, based on dynamic programming, for the user assignment problem is presented in an energy harvesting multi-RAT rural broadband base station scenario. The optimisation focuses on the energy saving and QoS improvement that such user assignment algorithm can bring to an off-grid rural broadband wireless base station. In Chapter 6, we summarise and conclude the work presented in Chapters 3, 4 and 5 and introduce some future work which falls in the scope of this thesis.

Chapter 2

Background

This chapter introduces some of the prior knowledge required for a better understanding of Chapters 3, 4 and 5. Scenarios and background relevant to the use of TV white space (TVWS) for rural broadband are detailed in Section 2.1. General information about software defined radio (SDR) and field programmable gates array (FPGA) implementation is presented in Section 2.2, which also elaborates on the selected SDR platform and the implementation work-flow used in this thesis. Background about fast Fourier transform (FFT) modulated filter-bank multi-carrier (FBMC) system is given in Section 2.3. An introduction to equalisation for oversampled FFT modulated FBMC is provided in Section 2.4. Previous work and considerations related to multi-radio access networks (RANs) optimisation are presented in Section 2.5.

2.1 TV White Space for Rural Broadband

Depending on the geographical area, the TV-spectrum is divided in 6 MHz or 8 MHz channels. In Western Europe 49 ultra high frequency (UHF) channels of 8 MHz were used for analogue TV transmission, ranging from 470 MHz (Channel 21) to 862 MHz (Channel 69) [38]. As shown in Figure 2.1, the transition from analogue-TV to digital television (DTV) reduced the number of channels needed, multiplexing techniques allowing a single 6-8 MHz channel to hold multiple TV programs simultaneously. The newly available spectrum, also known as TVWS opened the horizons for a multitude of applications, ranging from wireless microphones (programme-making and special events (PMSE)) to internet access, while channels 50 to 69 were already reallocated to mobile phones [23, 39]. After the analogue TV switch-off, office of communications (OfCom), the regulatory organisation for broadcast, telecommunications and postal industries in the United Kingdom (UK), provided a set of rules for emission in the TVWS and associated trial conditions [22]. Those regulations include spectral



Figure 2.1: TV spectrum after switch-over for the UK in 2009, Ofcom [22].

requirements, given in Figure 2.2, and channel sharing rules, to protect the TV transmissions from leakage by eventual TVWS transmission. As such when transmitting in TVWS out-of-band emission are limited to -55dB and -69dB in the adjacent and next adjacent channels respectively. These spectral requirements affect the design of the baseband computation, on which Chapters 3 and 4 of this thesis focusses, as well as the design of the radio frequency (RF) frontend.

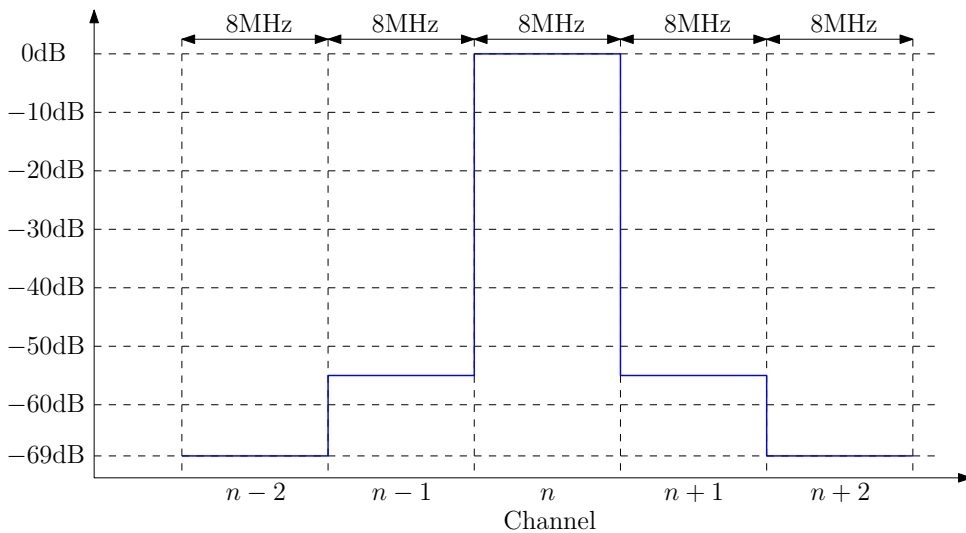


Figure 2.2: Ofcom spectral requirements for n^{th} channel [22].

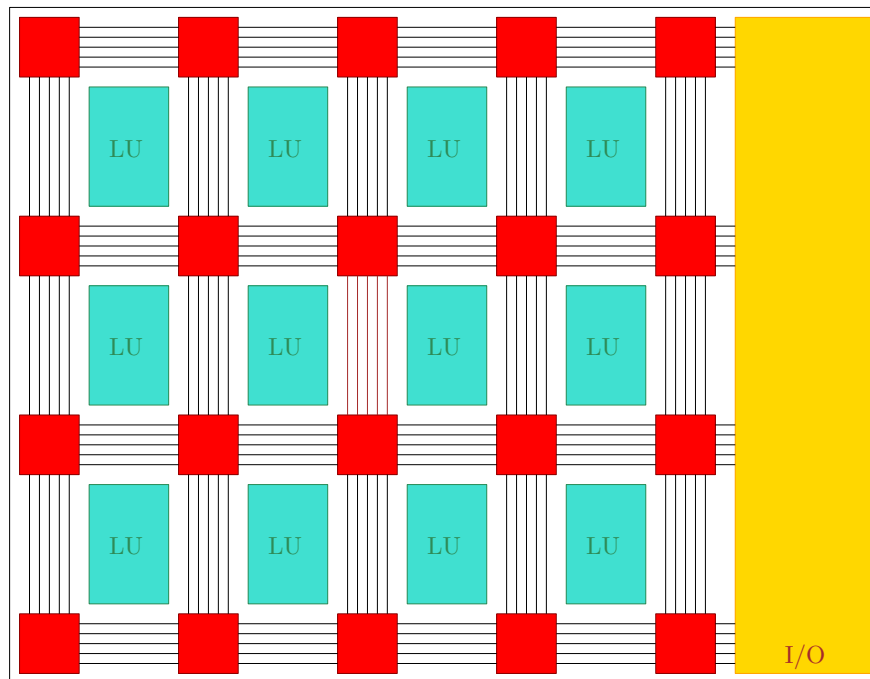


Figure 2.3: Early FPGA architecture, including look-up table (LUT), input/outputs (I/Os) and interconnection network.

2.2 Software Defined Radio Implementation

Understanding of SDR and FPGA architectures is critical to justify some of the design choices and constraints used in Chapter 3 and Chapter 4, this section gives an overview of those architectures, highlighting the main specificities relevant to the implementation of baseband signal processing for SDR platforms.

2.2.1 FPGA Architecture

FPGAs were first introduced in the 1985 by Xilinx [40]; they were initially designed as a collection of reprogrammable LUTs with a reconfigurable interconnection network, as shown in Figure 2.3. Similar to complex programmable logic device (CPLD), FPGAs use random access memory (RAM) technology instead of read-only memory (ROM). Since the introduction of the first FPGA, the technology has substantially evolved, not only in terms of the number of LUTs and interconnections available, but also by the addition of new specialised slices within FPGAs. These incorporations may look as if they reduce the flexibility of FPGAs, but greatly increase their computation power, leading to more advance algorithms being implemented on newer generations of devices. Initially, these added slices were discrete fixed-point multipliers and adders, which would

later be replaced by multiplication-accumulation (MAC) units, optimised for filter implementation. Other additions to FPGAs include dedicated RAM blocks, high throughput I/O serial transceivers, and more recently soft-cores such as advance reduced instruction set computing (RISC) machine (ARM) cores. The connectivity of FPGAs was also improved by the addition of advanced peripherals, such as inter-integrated circuit (I²C), ethernet and memory controllers, as shown in Figure 2.4. The implementation of most of these specialised slices using LUTs and standard I/O resources is possible but not advisable, as it would be a very costly solution, because of the resource usage and the high interconnection cost, while likely providing lower performance. Furthermore, the high interconnection requirements can induce an underutilisation of the computational resources of the FPGA. This is due to the fact that the FPGAs slices are not fully interconnected and that the routing of a large and complex systems might render unused resources inaccessible or prove to be an unsolvable routing problem on an underused FPGA; this is due to timing and critical path constraints, related to signal propagation within the device.

Modern FPGAs provide a highly reconfigurable and massively parallel computation structure allowing high performances signal processing, e.g. up to 21897 GMAC/s on a Virtex Ultrascale+ from Xilinx. However, the high flexibility comes at a cost, as placing and routing operations have become increasingly complex, requiring lengthy synthesis and implementations computation steps, as well as careful design.

Xilinx DSP48 Slice

The DSP48E1 slice is one of the most critical resource for signal processing applications in modern Xilinx FPGAs [41, 42]. Each DSP48E1 slice implements one 18×25 bits two's-complement multiplier, completed by a pre-adder (25 bits output) to facilitate the implementation of symmetric filters, as well as a 48 bits accumulator/arithmetic unit, optimised for filter implementation. The slice also includes resources for up and down conversion, as well as various registers, for the implementation of the tap delay line in finite impulse response (FIR) filters. A simplified block diagram is presented in Figure 2.5; the resources of a single DSP48E1 slice allow to implement a one coefficient filtering operation, as long as an adequate word-length is selected; a growth by one bit above the maximum word-length at the input of the slice increases the number of required multipliers to four, as detailed in [41, 42].

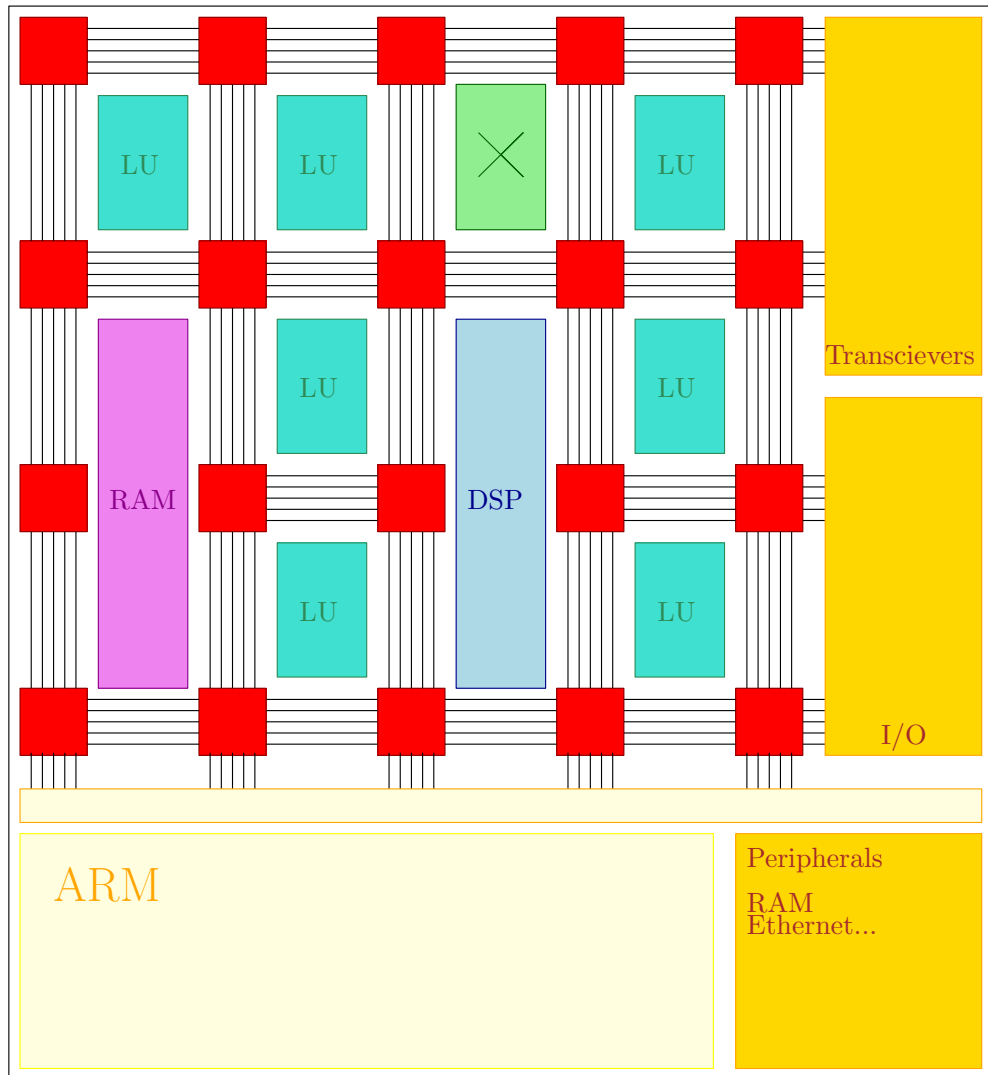


Figure 2.4: Modern FPGA architecture including LUT, I/Os, high speed I/Os, multipliers, digital signal processor (DSP) blocks, RAM, ARM core, peripherals and inter-connection network.

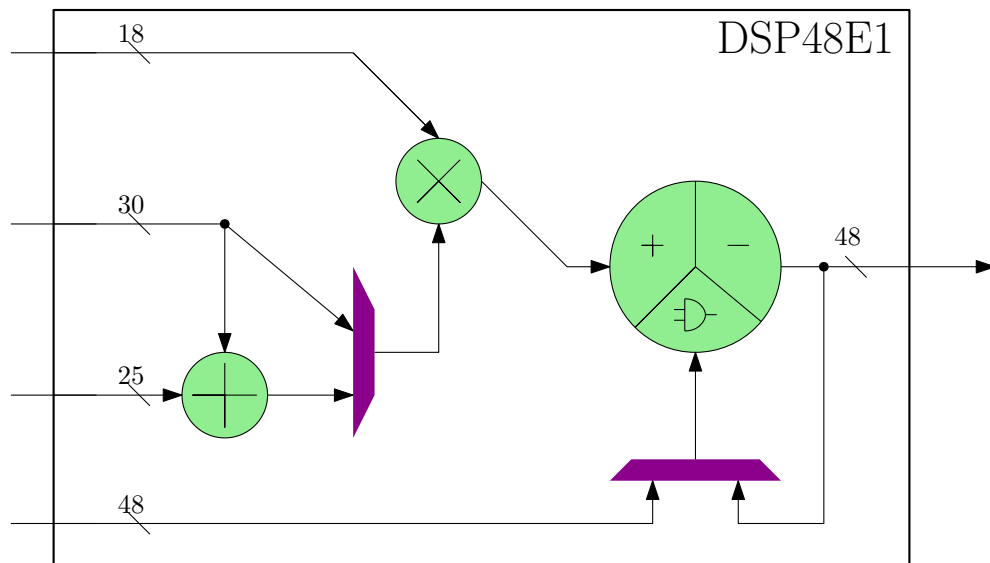


Figure 2.5: Simplified block diagram of the DSP48E1 from the series 7 Xilinx FPGAs.

Performance Metrics

This section introduces the performance metrics used to measure implementation costs in Chapters 3 and 4. Two main metrics are used resources usage and power consumption extracted from the Vivado tools from Xilinx [43, 44], the first is a common metric for FPGA implementations, while the power consumption is used to determine the most energy efficient approach for future implementations. Estimating the power consumption of an FPGA is a complex problem, this thesis use the power analysis tool included in Xilinx Vivado and while the exact process for estimation is outside the scope of this thesis, there are a several elements that affect power consumption. There are two types of power consumption sources within integrated circuits (ICs), related to state transitions and signal propagation. Adequate models, usually provided by the manufacturers, can be used to estimate the power consumption of a device. Within FPGAs those costs are related to

- processing related costs, i.e. LUTs, DSP48E1, RAM and I/Os, these costs are closely related to the use of these resources as well as running frequency, with the DSP48E1 blocks representing the highest power consumption cost per unit;
- signal routing costs are linked to the route and place process of the FPGA implementation, and the variations in signal propagation path length and running frequency.

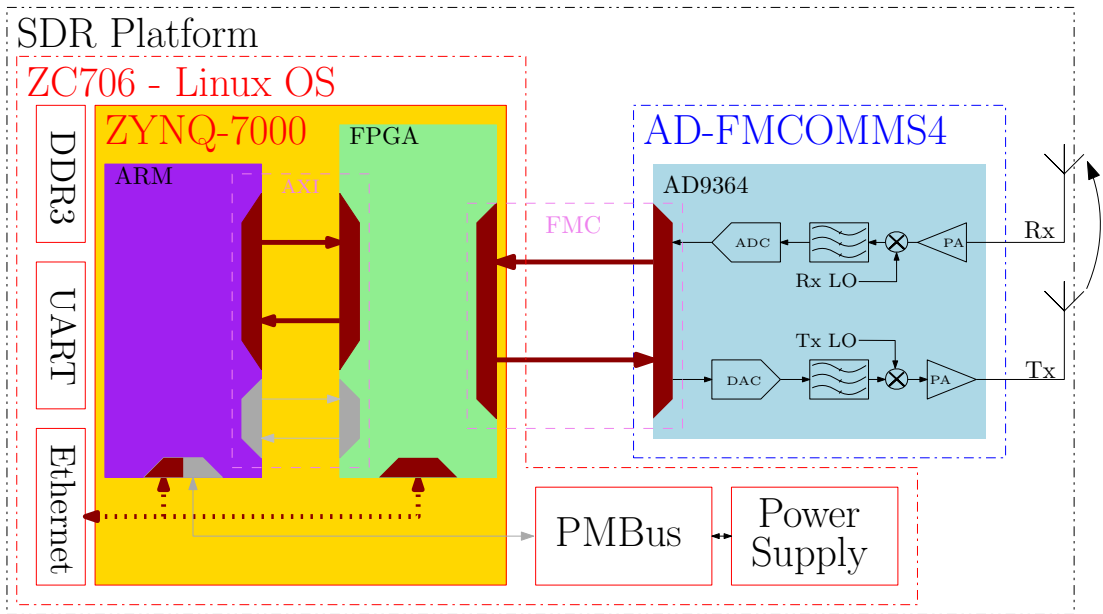


Figure 2.6: Zynq SDR system architecture, based on a Xilinx ZC706 and Analog Devices AD-FMCOMMS4 evaluation boards.

2.2.2 Zynq SDR

The implementations in Chapter 3 assume a Zynq-SDR as the targeted platform. The platform, of which a simplified block diagram is given Figure 2.6, employs a ZC706 evaluation board [45] from Xilinx and a AD-FMCOMMS4 evaluation board [46] from Analog Devices. The first includes a Xilinx Zynq 7045 system on chip (SoC) [47], which implement both an ARM dual core processor and an average size FPGA. The computational resources of the Zynq 7045 FPGA, used in Chapter 3, together with those for the Virtex 7VX550T device used in Chapter 4 are presented in Table 2.1.

The RF frontend provided by the Analog-Devices AD-FMCOMMS4 evaluation board is based on the AD9364 [48] chip from the same manufacturer, the main charac-

Table 2.1: FPGA resources Xilinx Zynq Z7045 used in Chapter 3, and Virtex 7 7VX550T targeted in Chapter 4.

	Zynq Z7045	Virtex 7 7VX550T
Logic Cells (K)	350	554
Block RAM (Mb)	19.1	42.4
DSP Slices	900	2880
Maximum I/O Pins	362	600
Maximum Transceiver Count	16	80

teristics of the RF frontend are:

- carrier frequency range: from 70 MHz to 6.0 GHz ,
- channel bandwidth from < 200 kHz to 56 MHz ,
- 1 receiver (Rx) and 1 transmitter (Tx) RF chains,
- 12 bits analogue-to-digital converter (ADC),
- 12 bits digital-to-analogue converter (DAC).

While this platform does not provide the sufficient bandwidth for full coverage of the TV spectrum, it allows to conduct feasibility studies, using fast prototyping by way of the hardware (HW)/software (SW) co-design workflow from MATLAB[®]. Furthermore, this platform shares characteristics with several SDR systems including more advance devices, this study could then be used as a stepping stone towards more advanced platforms such as universal software radio peripheral (USRP) N310/N320 [49, 50] or Xilinx' radio frequency system on chip (RFSoc) chips [51].

2.2.3 MATLAB[®] HW/SW Co-Design Workflow

To allow fast prototyping, the implementations presented in Chapter 3 and Chapter 4 were performed using the HW/SW co-design work-flow [35] and hardware description language (HDL) Coder [52] respectively, provided by Mathworks for its MATLAB[®] and Simulink products. In this section an overviews of the process is given.

The design and implementation process, using the MATLAB[®] HW/SW co-design work-flow, can be divided in 5 main steps.

1. **Floating-point algorithm design and simulation**, during this step the user needs to pay attention to the sampling frequency and validate the performance of the algorithm.
2. **Conversion to fixed-point**, this critical step is performed by setting strategic values and using auto-propagation tools of the MATLAB[®] Fixed-point Toolbox [53]. To confirm the fixed-point performance of the algorithm, a thorough check of the results of the simulation is necessary; this allows to ensure that all word-lengths, number representation and precisions stay within the requirements for an efficient use of the computational resources of the FPGA, while only affecting the performances of the implemented algorithm within requirements, when compared to the floating point design.

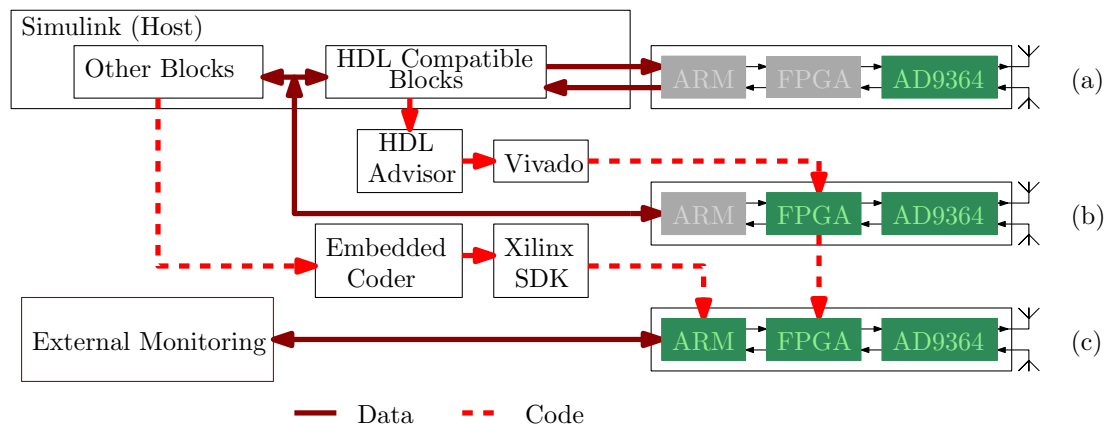


Figure 2.7: Mathworks SDRHW/SW co-design work-flow, use-cases (a), (b) and (c).

3. **Hardware code generation and FPGA synthesis and implementation**, several important parameters are set during this step, such as clocking related option, type of optimisation, i.e. area, speed, or compile time optimisation, etc. HDL code is generated by the HDL Coder, while the synthesis, implementation, bit stream generation and transfer to device are managed by Vivado tools, in an all integrated process within the MATLAB[®] ecosystem [35].
4. The **software interface design** step is important, as this interface needs to manage the device configuration, the data movements, data post-processing and visualisation. The quality of this interface is critical for an accurate and efficient validation of the system behaviour and performances [35].
5. **Validation** is necessary to confirm the system behaviour and performances and need to be undertaken very carefully.

One will note that while performing these steps, small changes can lead to great discrepancy, as well as low performance and inefficient FPGA resource usage. A typical issue is a inadequately selected word-length at the input of multiplication, leading to a higher than expected implementation cost.

There are several ways to use the workflow to implement SDR systems, with three main use cases available when using the workflow together with a Zynq-SDR platform shown in Figure 2.7:

- (a) in this scenario all the data is processed by the host; while this is the easiest operation mode to use, performance is limited by the host and its ability to handle and process data.

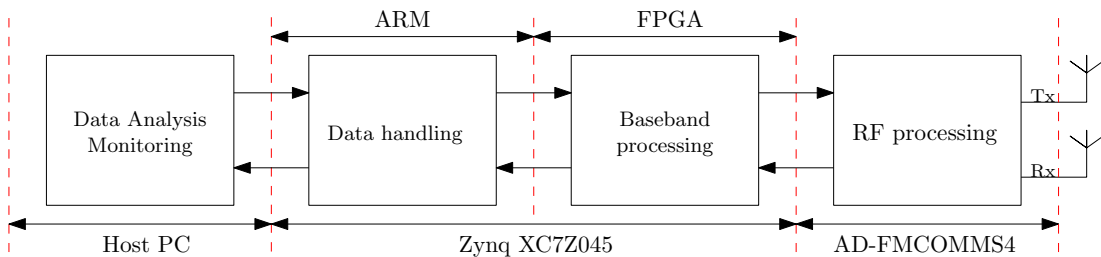


Figure 2.8: Zynq SDR considered system architecture

- (b) performance can be increased by moving some of the expensive signal processing onto the FPGA, allowing a reduction of the data processed by the host. This use case takes advantage of the massively parallel architecture of the FPGA allowing for more efficient implementations of signal processing algorithms.
- (c) the embedded mode reduces the host role to a monitoring role, by using C/C++ code generation tools and cross-compilation to move higher level functionalities onto the ARM core of the Zynq platform, bringing the design closer to a production system.

This thesis mainly implements scenarios (a) and (b), with (a) employed for development and debugging purposes, while (b) is used as the final architecture for the tested algorithms, leading to the overall system architecture shown in Figure 2.8.

2.3 Oversampled FFT Modulated FBMC

This section describes an FFT modulated FBMC system as summarised in [54] and shown in Figure 2.9. In this thesis, the FBMC systems are used to efficiently up- and down-convert 40 channels from the TV spectrum. More specifically, this thesis considers an oversampled FBMC systems, for the advantages they provide in terms of synchronisation and equalisation, as well as channels separation performances.

2.3.1 System Description

Different from orthogonal frequency-division multiplexing (OFDM), discrete Fourier transform (DFT) modulated FBMC systems allocate the energy and information related to samples both in time and frequency. At baseband, i.e. before modulation, the energy of a single sample is spread in the time-domain by the successive use of an upsampling operation followed by FIR filter, on the receiver side the inverse operations are used to reconstruct the sample. The ratio depends on the prototype filter length; as such systems implementing long prototype filters have most of the information related

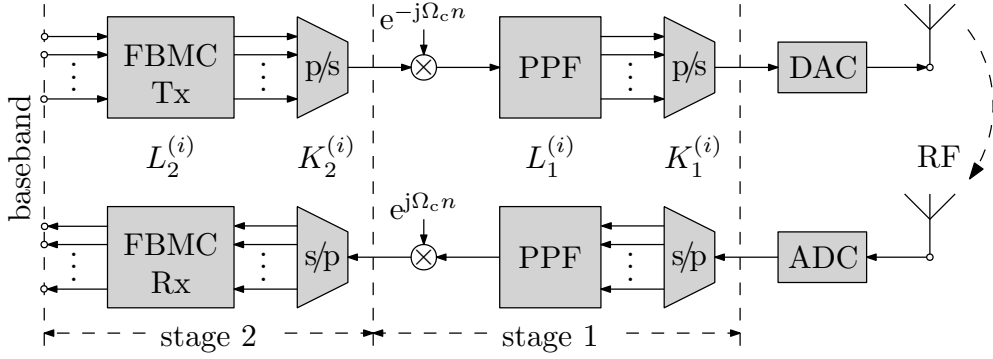


Figure 2.9: Two-stage TVWS filter-bank Tx (above) and Rx (below) with a polyphase filter (PPF) in stage 1 and an FBMC system in stage 2, as proposed in [54].

to a sample spread over time, leading to difficult synchronisation, but lower inter-carrier interference (ICI), while shorter prototype filters would induce leakage into the adjacent channels, thus spreading information through the spectrum, increasing dependence between channels and introducing more ICI.

For the system proposed in [54], on the receiver side the conversion from baseband to digital RF is performed in two stages. Seen from the receiving antenna, a first stage (stage 1) converts the RF signal to a lower intermediate frequency (IF) signal whose rate enables it to be handled by an FPGA, depending on the selected hardware this part of the FBMC transceiver might be implemented in the analogue domain, as in Chapter 3, or digital domain as in [54]. A second stage, namely stage 2, is responsible for the multiplexing the 40 TVWS channels into a single baseband signal in the Tx branch, and the demultiplexing from the equivalent single baseband signal in the receiver branch back into the 40 TVWS channels.

Stage 1:

When fully implemented in the digital domain, on the receiver side, i.e. the lower branch in Figure 2.9, an ADC acquires data at an RF sampling rate f_s with a word length R_{rx} . A bandpass filter extracts the 320 MHz wide UHF band that contains the 40 8 MHz wide TVWS channels, and due to the band limitation imposed by the filter, enables a reduction of the sampling rate by a factor $K_1^{(i)}$, where the index i denotes different design options. The decimation of the signal implicitly results in a demodulation; a modulation correction, $e^{j\Omega_c n}$ in Figure 2.9, then aligns the 40 TVWS channels in the baseband between DC and 320 MHz .

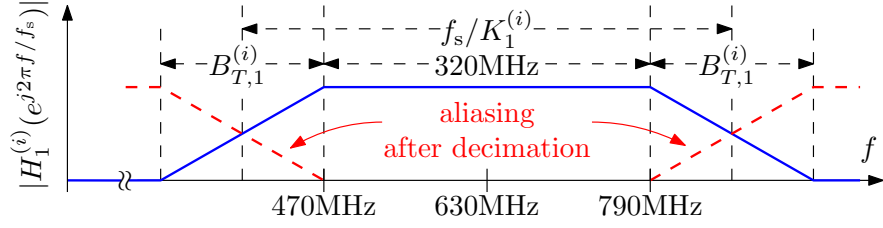


Figure 2.10: Stage 1 filter $h_1^{(i)}[\ell]$; the transition bandwidth $B_{T,1}^{(i)}$ depends on the decimation ratio $K_1^{(i)}$ as described in [54].

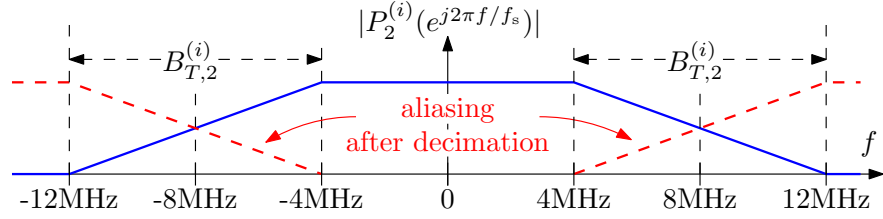


Figure 2.11: Stage 2 prototype filter with passband width of 8 MHz as described in [54].

To efficiently implement the receiver stage 1, the bandpass filter $h_1^{(i)}[\ell]$, of length $L_1^{(i)}$, whose magnitude response $|H_1^{(i)}(e^{j\Omega})|$ and associated transition bands $B_{T,1}^{(i)}$ are characterised in Figure 2.10. The filter is implemented in a polyphase network, enabling to swap the decimation by $K_1^{(i)}$ with the filtering, using the Noble identity [55] presented in Figure 2.12. This reduces the computational cost by a factor of $K_1^{(i)}$, keeping the same filter length but operating at a lower frequency. Additionally, the downconversion enhances the signal-to-quantization-noise ratio (SQNR) by potentially increasing the effective word length by $\Delta R = \log_4 K_1^{(i)}$ bits, under random noise conditions [56].

The transmitter operates analogously, and the baseband signal is implicitly up-converted to RF by expansion. To ensure that the resulting RF signal sits between 470 and 790 MHz, the baseband signal is modulation-corrected prior to upsampling, and interpolated by a filter matched to $|H_1^{(i)}(e^{j\Omega})|$ in Figure 2.10. Again, an efficient polyphase implementation minimises the implementation cost, and the word length can potentially be reduced at RF by $\Delta R_1 = \log_4 K_1^{(i)}$ bits without affecting the SQNR [56].

Stage 2:

The conversion between the 40 TVWS channels and the baseband signal required for stage 1 is performed with the help of an oversampled DFT modulated filter-bank with $K_2^{(i)}$ channels, operating as a transmultiplexer. The design is based on a 8 MHz wide prototype $p_2^{(i)}(\ell)$, with a filter length $L_2^{(i)}$, as characterised in Figure 2.11, the transition

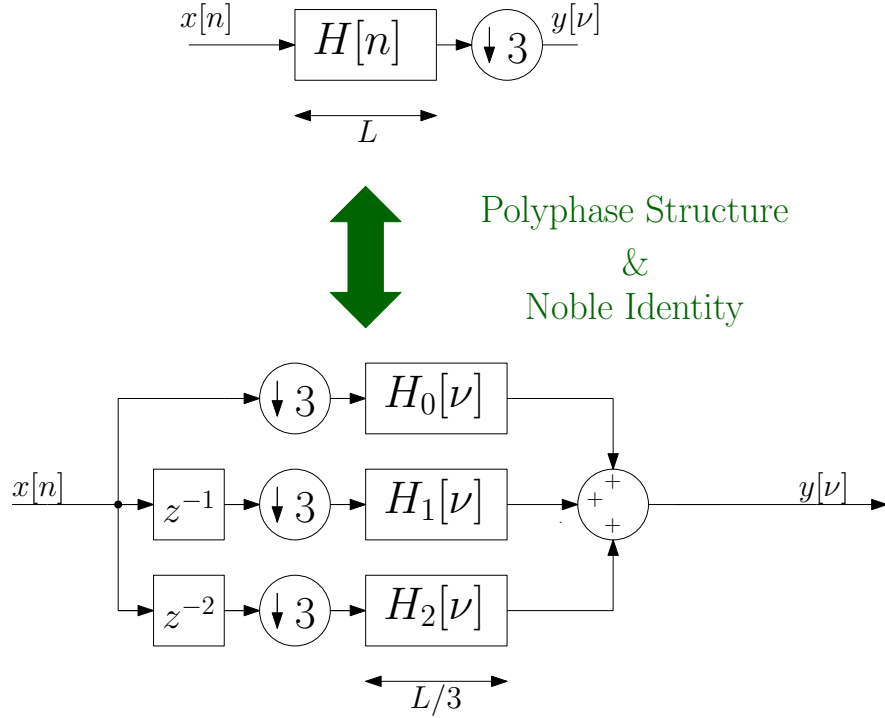


Figure 2.12: Downconversion, equivalence between a simple FIR filter followed by a downsampler and a polyphase network downconverter.

band $B_{T,2}^{(i)}$ as in stage 1 depends on the oversampling ratio $K_2^{(i)}$ respectively. In this design, a 5.3MHz signal is transmitted over each 8 MHz wide TV channel sampled at 16 MHz, i.e., the input signal is oversampled by a factor of $K_3^{(i)} = 3$. This provides a sufficient transition band, but will also enable advanced synchronisation and equalisation as detailed in Chapter 4.

The prototype filter $P_2^{(i)}$ is modulated by a DFT to the $K_2^{(i)}$ different band positions, which in the receiver operate as band selection filters to extract band-limited TVWS channels which subsequently can be decimated by $K_2^{(i)}/K_3^{(i)}$. In the transmitter, these filters follow an expansion by $K_2^{(i)}/K_3^{(i)}$ and fulfil the purpose of interpolation filters. Similarly to stage 1, the band limitation and expansion/decimation implies a potential gain in word length by $\Delta R_2 = \log_4(K_2^{(i)}/K_3^{(i)})$.

An efficient polyphase representation of the FBMC blocks ensures that the filtering is always operated as the lower rate. Further, a DFT filter-bank enables a factorisation into a polyphase network consisting of operations that only involve real-valued prototype filter, and a $K_2^{(i)}$ -point DFT [57, 58]. As a result, the FBMC implementation for

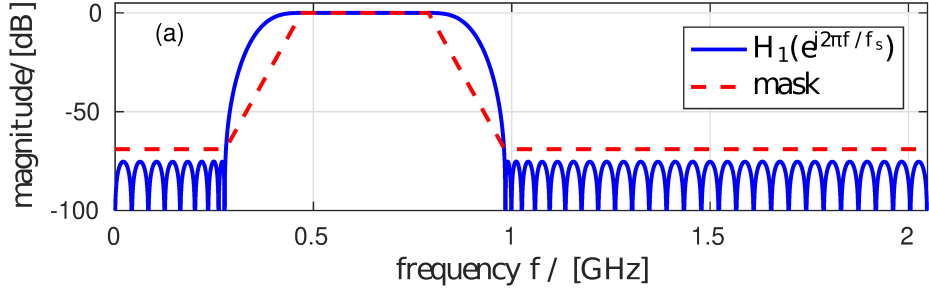


Figure 2.13: Filter design prototype for stage 1 FBMC system as described in [1].

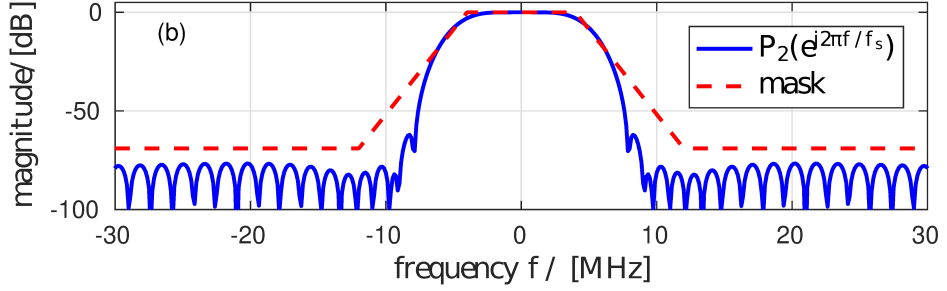


Figure 2.14: Filter design prototype for stage 2 FBMC system as described in [1].

40 channels is just as costly as the conversion of a single channel, plus the cost of the DFT operation [54, 57, 59].

2.3.2 Design Example

The following example focuses on the design with $K_1 = 4$, $K_2 = 64$ and a sampling frequency at RF of 2.688 GHz as in [1]. A filter $h_1[\ell]$ for stage 1 based on a minimax design, and a prototype $p_2[n]$ of length L_2 constructed by an iterative weighted least squares approach for oversampled filter-bank design [60], require respective lengths of $L_1 = 46$ and $L_2 = 320$ to ensure that the overall design satisfies the mask requirements [61], as demonstrated for magnitude responses of filters $h_1[\ell]$ and $p_2[n]$ in Figures 2.13 and 2.14 respectively, where the transition bands $B_{T,1}^{(i)}$ and $B_{T,2}^{(i)}$ respectively are computed as presented in [54].

To achieve 16 bits word length accuracy at the ADC/DAC, the up- and downconversion process is operated with 16 bits words, but only 12 bits accuracy is required for the baseband signals coming from the upconverter and going out of the downconverter. If all TVWS channels are occupied, this results in the PSD at RF shown in Figure 2.15, which satisfy the required masks. The PSD of the multiplexed signal at the output

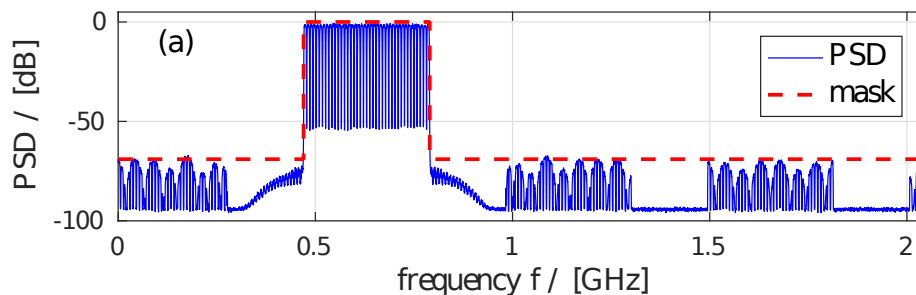


Figure 2.15: Power spectral density (PSD) of signals after stage 1 using bit-true and cycle-accurate simulations as described in [1].

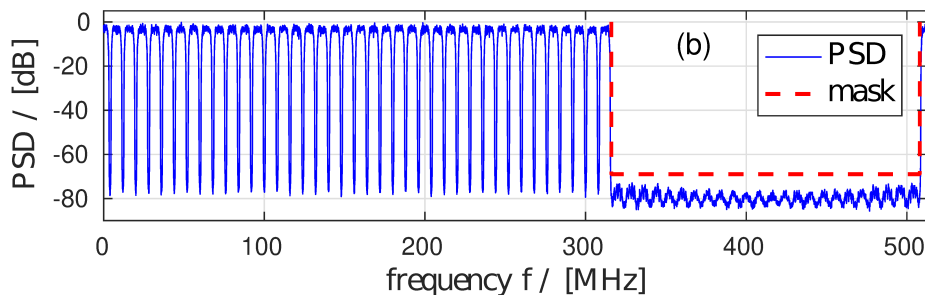


Figure 2.16: PSD of signals after stage 2 using bit-true and cycle-accurate simulations as described in [1].

of the transmitter stage 2 is shown in Figure 2.16. The graph also shows how the TVWS channels occupy the lower 40 of the overall 64 channels, while the upper ones are unoccupied and create design freedom for the stage 1 prototype filter.

2.4 Equalisation for Oversampled FFT Modulated FBMC for TVWS Operation

This section provides background on the equalisation of FFT modulated oversampled FBMC systems, presented in Section 2.3 related to Chapter 4.

2.4.1 Equalisation for Multi-Carrier System

The equalisation of multi-carrier systems is a well studied area of research, both for OFDM [62–65] and FBMC systems [66–71]. Compared to OFDM and critically sampled FBMC systems, such as FBMC offset-quadrature amplitude modulation (OQAM) [68, 69, 72, 73], oversampled FBMC systems are less affected by ICI. Indeed, the oversampled FBMC systems, introduced in Section 2.3 and further detailed in Chapter 3

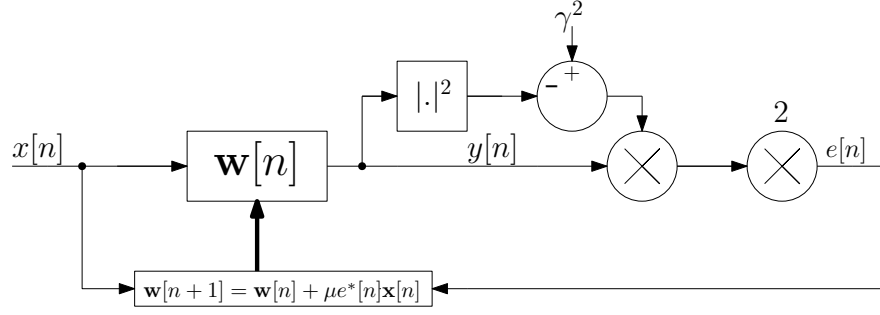


Figure 2.17: Constant modulus equaliser block diagram.

include wide garde-bands between channels [55], resulting in almost fully independent (i.e. non-overlapping) channels, allowing the per-channel equalisation presented in Chapter 4. In contrast OFDM and FBMC OQAM system, both critically sampled are on the other hand more subject to ICI, require cross-channel equalisation, including at least adjacent channels [74, 75].

The target application for the oversampled FFT modulated FBMC system presented in this thesis, by only utilising a few of the modulated channels and sharing the rest of the spectrum with the TV services, differs from the typical frequency division duplex (FDD) multiplexing application where the modulated channels are used to differentiate between users within a single service, e.g. mobile networks; this further justify the use of a per-channel equalisation scheme.

This thesis presents an equaliser based on a constant modulus (CM) approach, for which the background is provided in the following section.

2.4.2 Constant Modulus Equalisation

The CM algorithm is a well-known blind equalisation technique [76–80] and this section details the algorithm and its derivation. The CM algorithm is a stochastic gradient descent technique applied to a CM cost function ξ_{CM} [76], defined as the mean squared error (MSE) between the squared modulus of the output signal of the equaliser $y[n]$ and a target squared modulus γ :

$$\xi_{\text{CM}}[n] = \text{E}\left\{(\gamma^2 - |y[n]|^2)^2\right\}, \quad (2.1)$$

where $\text{E}\{\cdot\}$ is the expectation operator. The use of squared modulus reduces greatly the implementation cost of the algorithm, as it cancels the square root operation of the

modulus, such as:

$$|y[n]|^2 = \left(\sqrt{\operatorname{Re}\{y[n]\}^2 + \operatorname{Im}\{y[n]\}^2} \right)^2 = \operatorname{Re}\{y[n]\}^2 + \operatorname{Im}\{y[n]\}^2. \quad (2.2)$$

However, it renders the cost function ξ_{CM} dual quadratic with respect to the adaptive filter coefficients $\mathbf{w}[n]$. Given an input signal $x[n]$ stored into a tap-delay line $\mathbf{x}[n]$ and an adaptive filter $\mathbf{w}[n]$ the equaliser output $y[n]$ can be expressed as:

$$y[n] = \mathbf{w}^{\text{H}}[n] \cdot \mathbf{x}[n]. \quad (2.3)$$

As a consequence of its biquadratic characteristics, the CM cost function ξ_{CM} presents local minima, the optimisation problem thus exhibits a manifold of solutions, limiting the performance of the CM algorithm, this is however balanced by the fact this function only requires the received signal, to oppose to other stochastic gradient descent techniques such as least mean square (LMS) algorithm, which requires a delayed version of the transmitted signal $d[n] = x[n - \delta_n]$ to be fed to the algorithm [81].

The CM algorithm uses a stochastic gradient approach to update the filter coefficients $\mathbf{w}[n]$, such as

$$\mathbf{w}[n + 1] = \mathbf{w}[n] + \mu \nabla \hat{\xi}_{\text{CM}}[n], \quad (2.4)$$

where μ is the step size between updates and the cost function estimate $\hat{\xi}_{\text{CM}}$ is obtained by dropping the expectation operator from (2.1) and the gradient $\nabla \hat{\xi}_{\text{CM}}[n]$ is obtained using Wirtinger derivatives [82]:

$$\begin{aligned} \nabla \hat{\xi}_{\text{CM}}[n] &= \frac{\partial}{\partial \mathbf{w}^*[n]} (\gamma^2 - |y[n]|^2)^2 = 2 (\gamma^2 - |y[n]|^2) \frac{\partial}{\partial \mathbf{w}^*[n]} (-y[n]y^*[n]) \\ &= -2 (\gamma^2 - |y[n]|^2) \left(\frac{\partial \mathbf{w}^{\text{H}}[n] \mathbf{x}[n]}{\partial \mathbf{w}^*[n]} \cdot y^*[n] + y[n] \cdot \frac{\partial \mathbf{w}^{\text{T}}[n] \mathbf{x}^*[n]}{\partial \mathbf{w}^*[n]} \right) \\ &= -2 (\gamma^2 - |y[n]|^2) (\mathbf{x}[n]y^*[n] + 0), \end{aligned} \quad (2.5)$$

leading to a update equation:

$$\mathbf{w}[n + 1] = \mathbf{w}[n] + 2\mu (\gamma^2 - |y[n]|^2) y^*[n] \mathbf{x}[n], \quad (2.6)$$

then assuming an error function

$$e[n] = 2 (\gamma^2 - |y[n]|^2) y[n], \quad (2.7)$$

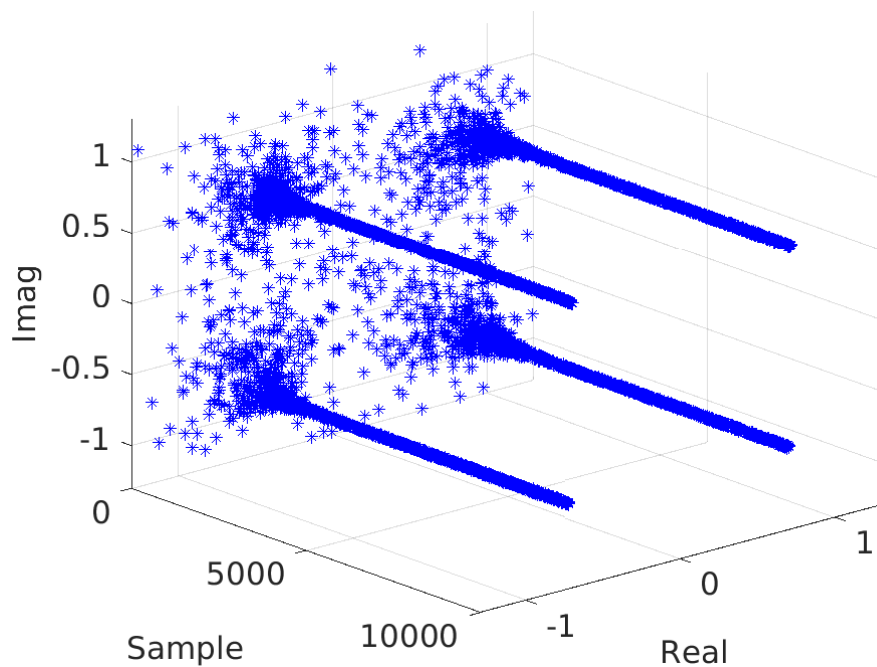


Figure 2.18: CM algorithm output equalising a quadrature phase-shift keying (QPSK) constellation submitted to a channel introducing inter-symbol interference (ISI) only.

(2.6) can be rewritten as a typical LMS update equation:

$$\mathbf{w}[n+1] = \mathbf{w}[n] + \mu e^*[n]\mathbf{x}[n]. \quad (2.8)$$

A block diagram is presented in Figure 2.17. The CM algorithm is very well suited for phase-shift keying (PSK) signals providing blind equalisation, it is however ineffective to correct constellation rotation induced by the phase or frequency offset, due to the presence of local minima within the cost function ξ_{CM} , defined in (2.1), which does not take into consideration any phase-related information. The impact of a frequency offset on the output of the CM algorithm is shown in Figure 2.19. Another limitation of the CM cost function reside in the value of the gradient estimate $\nabla \hat{\xi}_{CM}[n] = 0$ when $\mathbf{w}[n] = 0$, which prevents the update of the coefficients (2.4). Although it is unlikely that the algorithm will converge toward $\mathbf{w}[n] = 0$, one need to be careful with the initialisation of the CM algorithm so: $\mathbf{w}[0] \neq 0$. As the cost function is biquadratic and multi-modal with local minima, different initialisations also implies different solutions.

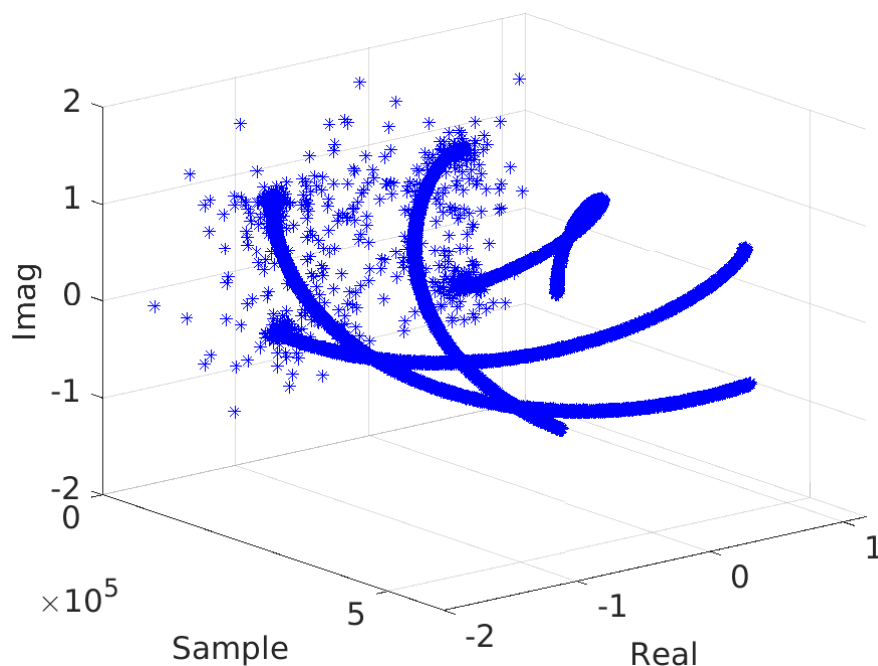


Figure 2.19: Effect of frequency offset on the CM algorithm equalising a QPSK constellation.

2.5 Multi-Radio Base Station User Assignment

Multi-radio load assignment optimisation algorithms and their benefits with respect to the power consumption have previously been studied on mobile devices, using Wireless Fidelity (WiFi) and Bluetooth [83]. In [84, 85] more general approaches considering the quality of service (QoS) are presented, in a scenario where the available power is limited by the battery capacity on mobile devices always offering more connectivity.

Previous work on rural broadband access introduced the concurrent use of WiFi and TVWS RAN to take advantage of the spatial repartitioning of users in rural environment, with users regrouped into clusters—villages—surrounded by sporadically placed homes [19]. The concurrent use of multiple radio access technologys (RATs) within a single base station provides degrees of freedom, which in turns makes it possible to optimise the performance of the base station, both in terms of QoS [28] and energy efficiency [21]. Optimisation of multiple radio systems at the base station is often focused on the use of different types of base stations (small versus macro base stations) [86] and not a single base station basis with multiple radio technologies [21, 28].

With respect to rural broadband base stations, previous work [24–26] introduced the

use of renewable energy to tackle both planning issues and access to electrical power, as the best base station site might be off-grid. Two approaches are then possible to maintain service : either the energy system needs to be over-dimensioned to guarantee a minimum service [19] or resource management schemes have to be introduced [27]. Various resource management techniques have been proven effective in energy harvesting communication networks [28, 31, 32, 37].

2.6 Chapter Summary

In this chapter, we gave a short overview of the prior knowledge required to better understand the research presented in the following chapters, more specifically we focussed on information that is relevant to justify some of the research direction and design decision taken in the coming chapter. We introduced the use of TVWS radio system to provide broadband in rural areas, as well as previous work relevant to this problem and the FBMC transceiver systems this thesis explores further. Furthermore, we detailed some of the design constraints and considerations of FPGA implementation, we also quickly described the design process used for the SDR type implementation performed in this thesis. We also gave background on equalisation for oversampled FFT modulated FBMC systems as well as some information on user assignment for multi-radio base station.

Chapter 3

FFT Size Optimisation for Oversampled FFT Modulated FBMC Systems

Oversampled fast Fourier transform (FFT) modulated filter-bank multi-carrier (FBMC) systems, introduced in Section 2.3, have, in most applications, higher computational complexity than orthogonal frequency-division multiplexing (OFDM) systems. To keep the implementation cost low, further optimisation might be required. Compared to traditional implementations, this chapter explores the optimisation of the modulating transform, by adjusting the size of the transform and the structure of the FBMC system to increase the energy efficiency of the transceiver. After introducing the motivation for this work in Section 3.1, this chapter presents the derivations for the design of a custom 40-point multi-radix FFT, in Section 3.2, details about the design of the filters are presented in Section 3.3, while field programmable gates array (FPGA) implementation methodology and results are given in Sections 3.4 and 3.5 respectively.

3.1 Motivation and Rationale

The main objective of the work presented in this chapter is to determine the viability of the use of non power-of-two FFTs in FBMC systems for TV white space (TVWS) transmissions. In order to cover the integrity of the TVWS spectrum previous implementation work opted for FBMC systems, shown in Figure 2.9, using a 64-point FFT [54], thus covering 64 8 MHz channels. However, TVWS applications after the digital television (DTV) switch-over only required 40 8 MHz channels to be fully accessed, a number reduced further by spectrum reallocations; using a 64 channels thus leads to a minimum of 24 redundant channels and the associated computation cost.

As FBMC systems allocate most of the energy of a sample in its respective channel, to oppose to OFDM where large amount of energy leaks in adjacent channels, the importance of unused channels in FBMC system is largely reduced, rendering the extra FFT coefficients unimportant [87]. This fact is amplified by the high attenuation required with adjacent channels, to comply with the regulations for TVWS transmission [39], consequently the energy of the signals leaking into unused channels of the transceiver system is low with respect to the noise floor. The unused FFT coefficients can then be deemed unnecessary, thus justifying the idea of building a custom FFT that cover exactly the required number of channels.

For the designs presented in [59], and summarised in Section 2.3, it was found that a higher decimation or expansion in stage 1, and therefore a lower decimation or expansion in stage 2, leads to a more numerically efficient design than vice versa. This motivates further the use of a 40-point FFT instead of a larger power-of-two FFT which would allow for a full coverage of the TVWS spectrum. Nonetheless, the FPGA implementation in [54] ignored this optimality, as it had to rely on power-of-two FFTs inside the FBMC system due to design constraints. With $N = 2^k \geq 40$, $k \in \mathbb{N}$, the smallest possible number of channels covering the TVWS spectrum is $N = 64$, thus involving 24 unused channel that need to be zero-padded in the transmitter and discarded in the receiver.

Furthermore, since the DTV switch-over channels above 700 MHz have been re-assigned to mobile services [23] reducing the number of potentially usable channels to 30. This reduction in the number of available channels provides the system with 10 and 34 unused channels for the 40-point and 64-point system respectively, allowing for large transition band in the design of the filter for stage 1 (described in Section 2.3.2). While in theory, a 32-point transform could be enough to cover the integrity of the available spectrum, it would not provide sufficient transition bands and increase the design constraints on stage 1, making it complex and costly to implement. The 40-point size was chosen as a compromise of implementation complexity between stages 1 and 2.

3.2 FFT Design for FBMC Systems

To produce a 40 channel wide FBMC system, one either needs to rely on a 40 point discrete Fourier transform (DFT), or in order to attain a more numerically efficient design opt for a mixed-radix architecture [88], factorising $N = 40$ in $N = 40 = 2^3 \times 5$, i.e. building a 40-point FFT from a number of 8-point and 5-point FFTs. While the

8-point section can rely on readily available power-of-two FFT blocks, generated in this work using the Cooley-Tukey algorithm [89], the radix-5 block requires an explicit realisation [90, 91].

3.2.1 40 Point FFT

A mixed-radix 40-point FFT, using a radix-5 FFTs later described in Section 3.2.2 and standard 8-point FFTs can be derived from a 40-point DFT of an input vector $\mathbf{x} = [x_0, \dots, x_n, \dots, x_{N-1}]$, $N = 40$ the transform size, such as the corresponding DFT coefficient X_k are defined as

$$X_k = \sum_{n=0}^{N-1} x_n e^{-2j\pi \frac{kn}{N}} \quad (3.1)$$

with $N = M \times L = 40$ with $L = 8$ and $M = 5$. The formula in (3.1) can be re-indexed using $n = n_L + Mn_M$, $n_L \in \{0 \dots M-1\}$, $n_M \in \{0 \dots L-1\}$ and $k = Lk_L + k_M \in \mathbb{N}$, $k_L \in \{0 \dots L-1\}$, $k_M \in \{0 \dots M-1\}$, such as

$$\begin{aligned} X_{k_M+Lk_L} &= \sum_{n_L=0}^{L-1} \sum_{n_M=0}^{M-1} x_{n_L+Mn_M} e^{-2j\pi \frac{(n_L+Mn_M)(k_M+Lk_L)}{M \times L}} \\ &= \sum_{n_L=0}^{L-1} \sum_{n_M=0}^{M-1} x_{n_L+Mn_M} e^{-2j\pi \frac{n_L k_M}{N}} e^{-2j\pi \frac{n_L k_L}{M}} e^{-2j\pi \frac{n_M k_M}{L}} e^{-2j\pi n_M k_L} \end{aligned} \quad (3.2)$$

however $e^{-2j\pi n_M k_L} = 1$, thus leading to

$$X_{k_M+Lk_L} = \sum_{n_L=0}^{L-1} W_N^{n_L k_M} \left\{ \sum_{n_M=0}^{M-1} x_{n_L+Mn_M} e^{-2j\pi \frac{n_L k_L}{M}} \right\} e^{-2j\pi \frac{n_M k_M}{L}} \quad (3.3)$$

where the coefficient

$$W_N^{n_L k_M} = e^{-2j\pi \frac{n_L k_M}{N}} \quad (3.4)$$

are the twiddle factor applied between the two FFT operations. While the terms $\sum_{n=0}^{L-1} x_n e^{-2j\pi \frac{kn}{L}}$ and $\sum_{n=0}^{M-1} x_n e^{-2j\pi \frac{kn}{M}}$ represent the $L = 8$, $M = 5$ -point FFTs respectively. The transform is then implemented in two stages, for which either five 8-point FFTs are followed by a reorganisation with application of the twiddle factor defined in (3.4) and eight radix-5 FFTs, or vice versa. For the latter organisation, a flow graph is shown in Figure 3.1.

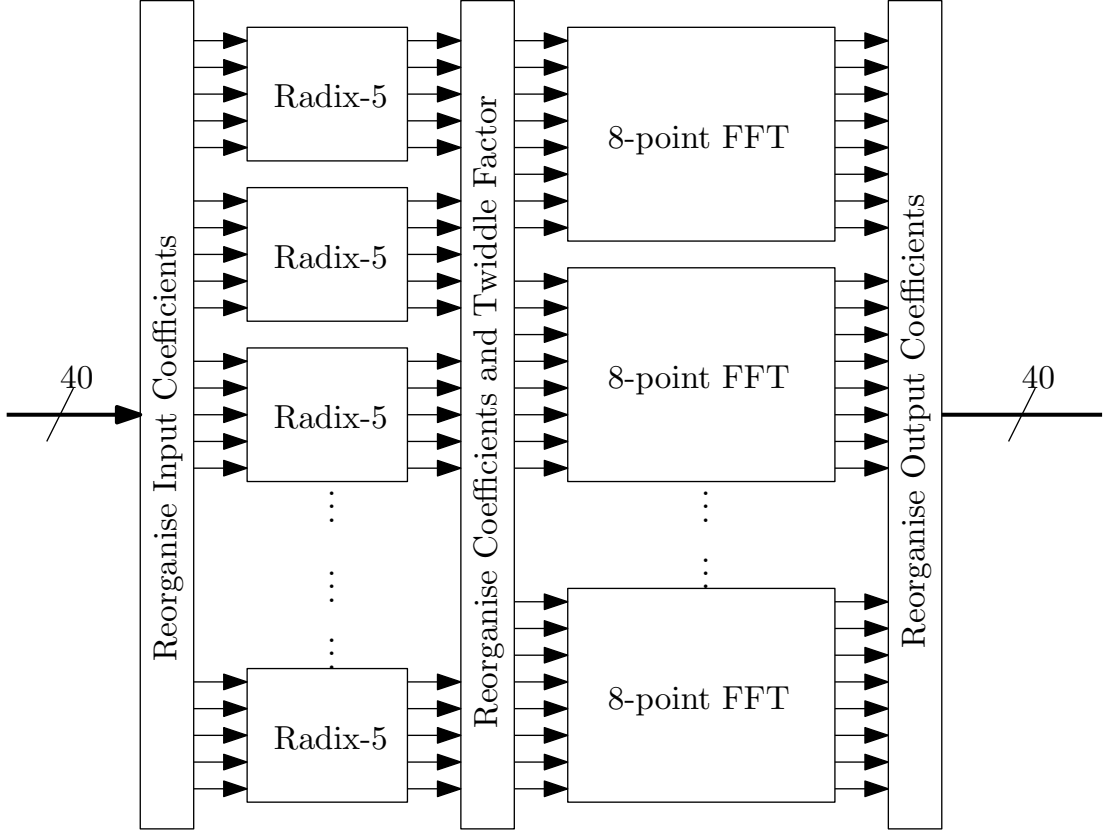


Figure 3.1: 40 point mixed-radix FFT, build by cascading radix-5 and radix-8 FFTs in a fully parallel structure.

3.2.2 Radix-5 FFT Block

A radix- N FFT can be derived from an N -point DFT. Given time domain coefficients $x_n, n = \{0, \dots, (N - 1)\}$, N Fourier coefficients $X_k, k = \{0, \dots, (N - 1)\}$ are calculated via evaluation of

$$X(e^{j\Omega}) = \sum_{n=0}^{N-1} x_n e^{-j\Omega n} \quad (3.5)$$

at sample points

$$X_k = X(e^{j\Omega_k}), \quad (3.6)$$

$\Omega_k = 2\pi k/N$. With time domain samples x_n in a vector $\mathbf{x} \in \mathbb{C}^N$, and the Fourier coefficients in a vector $\underline{X} \in \mathbb{C}^N$, the DFT can be written as

$$\underline{X} = \mathbf{T}\mathbf{x}. \quad (3.7)$$

Defining the factors $W_N^k = e^{-j2\pi k/N}$, the DFT matrix for an example of $N = 5$ is

$$\mathbf{T} = \begin{bmatrix} W_5^0 & W_5^0 & W_5^0 & W_5^0 & W_5^0 \\ W_5^0 & W_5^1 & W_5^2 & W_5^3 & W_5^4 \\ W_5^0 & W_5^2 & W_5^4 & W_5^6 & W_5^8 \\ W_5^0 & W_5^3 & W_5^6 & W_5^9 & W_5^{12} \\ W_5^0 & W_5^4 & W_5^8 & W_5^{12} & W_5^{16} \end{bmatrix}. \quad (3.8)$$

To reduce the implementation cost, various solutions have been presented in the literature [90–94]; they generally differ by trade-offs between the number of adders and multipliers; this work uses the approach described in [94] and detailed below. Exploiting the periodicity of the complex exponential, whereby

$$W_N^k = W_N^{k \pmod{N}} = e^{-j2\pi k/N}, \quad (3.9)$$

the DFT matrix can be restructured as

$$\mathbf{T} = \begin{bmatrix} 1 & 1 & 1 & 1 & 1 \\ 1 & W_5^1 & W_5^2 & \overline{W_5^2} & \overline{W_5^1} \\ 1 & W_5^2 & \overline{W_5^1} & W_5^1 & \overline{W_5^2} \\ 1 & \overline{W_5^2} & W_5^1 & \overline{W_5^1} & W_5^2 \\ 1 & \overline{W_5^1} & \overline{W_5^2} & W_5^2 & W_5^1 \end{bmatrix}, \quad (3.10)$$

with the complex conjugate $\overline{W_5^k} = W_5^{-k}$. This lead to the following set of equations:

$$\begin{aligned} X_0 &= x_0 + x_1 + x_2 + x_3 + x_4, \\ X_1 &= x_0 + x_1 W_5^1 + x_2 W_5^2 + x_3 \overline{W_5^2} + x_4 \overline{W_5^1}, \\ X_2 &= x_0 + x_1 W_5^2 + x_2 \overline{W_5^1} + x_3 W_5^1 + x_4 \overline{W_5^2}, \\ X_3 &= x_0 + x_1 \overline{W_5^2} + x_2 W_5^1 + x_3 \overline{W_5^1} + x_4 W_5^2, \\ X_4 &= x_0 + x_1 \overline{W_5^1} + x_2 \overline{W_5^2} + x_3 W_5^2 + x_4 W_5^1. \end{aligned} \quad (3.11)$$

$X_{\{1,2,3,4\}}$ from (3.11) are decomposed, in order to isolate the samples x_n multiplied by the real (respectively imaginary) part $\text{Re}\{W_5^k\}$ (respectively $\text{Im}\{W_5^k\}$) of the coefficients W_5^k . This decomposition aims to produce a low complexity radix-5 transform,

which only utilise purely real or imaginary gains, such as

$$\begin{aligned}
 X_1 &= x_0 + \operatorname{Re}\{W_5^1\}(x_1 + x_4) + \operatorname{jIm}\{W_5^1\}(x_1 - x_4) + \operatorname{Re}\{W_5^2\}(x_2 + x_3) \\
 &\quad + \operatorname{jIm}\{W_5^2\}(x_2 - x_3), \\
 X_2 &= x_0 + \operatorname{Re}\{W_5^2\}(x_1 + x_4) + \operatorname{jIm}\{W_5^2\}(x_1 - x_4) + \operatorname{Re}\{W_5^1\}(x_2 + x_3) \\
 &\quad - \operatorname{jIm}\{W_5^1\}(x_2 - x_3), \\
 X_3 &= x_0 + \operatorname{Re}\{W_5^2\}(x_1 + x_4) - \operatorname{jIm}\{W_5^2\}(x_1 - x_4) + \operatorname{Re}\{W_5^1\}(x_2 + x_3) \\
 &\quad + \operatorname{jIm}\{W_5^1\}(x_2 - x_3), \\
 X_4 &= x_0 + \operatorname{Re}\{W_5^1\}(x_1 + x_4) - \operatorname{jIm}\{W_5^1\}(x_1 - x_4) + \operatorname{Re}\{W_5^2\}(x_2 + x_3) \\
 &\quad - \operatorname{jIm}\{W_5^2\}(x_2 - x_3).
 \end{aligned} \tag{3.12}$$

To simplify the expressions above lets define

$$A_x = x_1 + x_4, \quad B_x = x_2 + x_3, \quad C_x = x_1 - x_4, \quad D_x = x_2 - x_3, \tag{3.13}$$

considering that the members A_x and B_x are multiplied by the same coefficients and that the members C_x and D_x have factors of opposite values in X_1 (resp. X_2) and X_4 (resp. X_3), then applying

$$\begin{aligned}
 \operatorname{Re}\{W_5^1\} &= \cos\left(\frac{2\pi}{5}\right), \quad \operatorname{Re}\{W_5^2\} = \cos\left(\frac{4\pi}{5}\right), \\
 \operatorname{Re}\{W_5^1\} + \operatorname{Re}\{W_5^2\} &= -\frac{1}{2}, \\
 \operatorname{Im}\{W_5^1\} &= -\sin\left(\frac{2\pi}{5}\right), \quad \operatorname{Im}\{W_5^2\} = -\sin\left(\frac{4\pi}{5}\right),
 \end{aligned} \tag{3.14}$$

$X_{\{1,2,3,4\}}$ in the set of equations (3.12) can be rewritten as

$$\begin{aligned}
 X_1 &= x_0 - \frac{1}{2}A_x - \cos\left(\frac{4\pi}{5}\right)(A_x - B_x) \\
 &\quad + j\left[\left(\sin\left(\frac{2\pi}{5}\right) + \sin\left(\frac{4\pi}{5}\right)\right)C_x - \sin\left(\frac{4\pi}{5}\right)(C_x + D_x)\right], \\
 X_2 &= x_0 - \frac{1}{2}B_x + \cos\left(\frac{4\pi}{5}\right)(A_x - B_x) \\
 &\quad - j\left[\left(-\sin\left(\frac{2\pi}{5}\right) + \sin\left(\frac{4\pi}{5}\right)\right)C_x - \sin\left(\frac{4\pi}{5}\right)(C_x + D_x)\right], \\
 X_3 &= x_0 - \frac{1}{2}B_x + \cos\left(\frac{4\pi}{5}\right)(A_x - B_x) \\
 &\quad + j\left[\left(-\sin\left(\frac{2\pi}{5}\right) + \sin\left(\frac{4\pi}{5}\right)\right)C_x - \sin\left(\frac{4\pi}{5}\right)(C_x + D_x)\right], \\
 X_4 &= x_0 - \frac{1}{2}A_x - \cos\left(\frac{4\pi}{5}\right)(A_x - B_x) \\
 &\quad - j\left[\left(\sin\left(\frac{2\pi}{5}\right) + \sin\left(\frac{4\pi}{5}\right)\right)C_x - \sin\left(\frac{4\pi}{5}\right)(C_x + D_x)\right],
 \end{aligned} \tag{3.15}$$

which if defining

$$\begin{aligned}
 \alpha_0 &= \frac{1}{2}, \quad \alpha_1 = \cos\left(\frac{4\pi}{5}\right), \quad \alpha_2 = \sin\left(\frac{2\pi}{5}\right) + \sin\left(\frac{4\pi}{5}\right), \\
 \alpha_3 &= -\sin\left(\frac{2\pi}{5}\right) + \sin\left(\frac{4\pi}{5}\right), \quad \alpha_4 = \sin\left(\frac{4\pi}{5}\right),
 \end{aligned} \tag{3.16}$$

becomes

$$\begin{aligned}
 X_0 &= x_0 + x_1 + x_2 + x_3 + x_4, \\
 X_1 &= x_0 - \alpha_0 A_x - \alpha_1(A_x - B_x) + j[\alpha_2 C_x - \alpha_4(C_x + D_x)], \\
 X_2 &= x_0 - \alpha_0 B_x + \alpha_1(A_x - B_x) - j[\alpha_3 D_x - \alpha_4(C_x + D_x)], \\
 X_3 &= x_0 - \alpha_0 B_x + \alpha_1(A_x - B_x) + j[\alpha_3 D_x - \alpha_4(C_x + D_x)], \\
 X_4 &= x_0 - \alpha_0 A_x - \alpha_1(A_x - B_x) - j[\alpha_2 C_x - \alpha_4(C_x + D_x)].
 \end{aligned} \tag{3.17}$$

This leads to the radix-5 flow graph of [94] depicted in Figure 3.2, and selected here for implementation due to its low number of complex valued operations. In its presented form, as multiplication by -1 and $\pm j$ can be implemented trivially without using multipliers, this radix-5 FFT block requires 12 multipliers, to perform 6 real-valued gains on complex-valued signals and 36 adders for 18 additions of complex-valued signals.

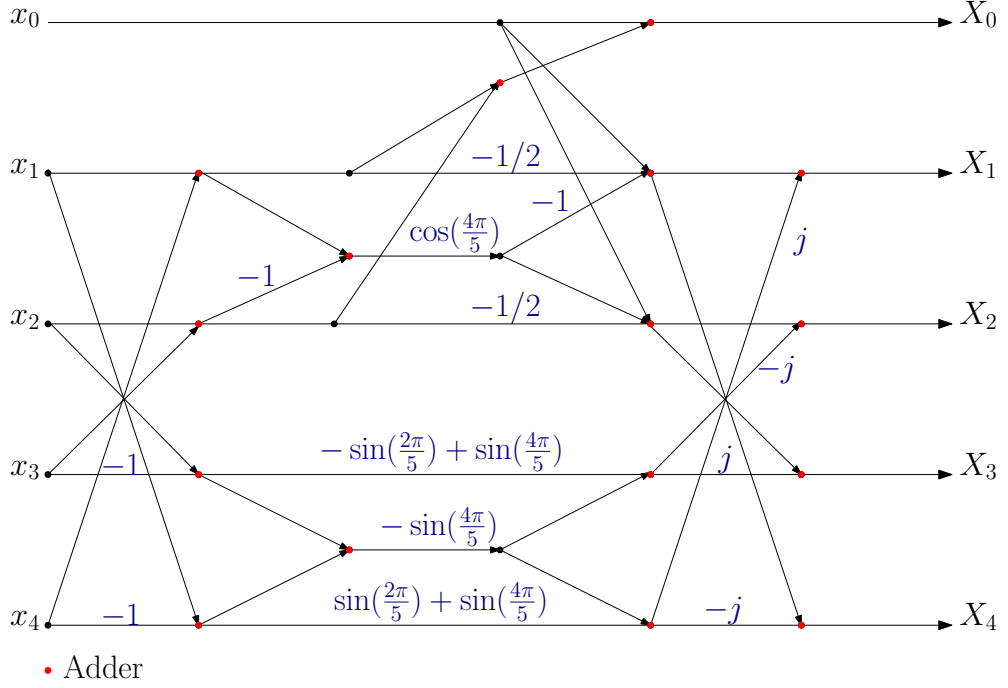


Figure 3.2: Radix-5 FFT implemented using purely real or imaginary gains as presented in [94].

3.2.3 Complexity

This work considers the implementation of complex multiplications using 3 real-valued multiplications and 5 real-valued additions [95]. It is assumed that there are no overheads for sample re-organisation, as it comes at a very low cost in comparison to computation as long as the FPGA is not overcrowded. Using the computational complexity of a radix-5 FFT stated in Section 3.2.2, and with an 8-point radix-2 FFT requiring two non-trivial complex-valued multiplication-accumulation (MAC) operations, i.e. 6 real-valued multiplications and 10 additions, as well as 48 real-valued additions to account for the requirements of the butterfly structures, a further 26 complex multiplications are needed to implement the twiddle factors, the overall complexity in terms of real-valued operations of a 40-point FFT, as presented in Figure 3.1, can be expressed as

$$\mathcal{C}_{\text{multipliers}} = 8 \cdot 12 + 5 \cdot 6 + 26 \cdot 3 = 204 \quad (3.18)$$

$$\mathcal{C}_{\text{adders}} = 8 \cdot 36 + 5 \cdot (48 + 10) + 5 \cdot 26 = 708. \quad (3.19)$$

This can be contrasted to the 40^2 complex multiply accumulate operations, if the transform was implemented by a standard DFT, requiring 4800 real-valued multiplications and 8000 real-valued additions. Additionally, the 64-point FFT previously used for

Table 3.1: Stage 1 filter characteristics

Size	40-point	64-point
Length L_1	65	60
Oversampling factor K_1	6	4
f_s (MHz)	1920	2048
$B_{T,1}$ (MHz)	240	352
$B_{P,1}$ (MHz)	160	160

TVWS FBMC system requires, when using a radix-2 architecture 264 real-valued multiplication and 1032 real-valued additions [96], an implementation cost still higher than the proposed design.

3.3 Filter Design

The prototype filters h_1 and p_2 are designed using similar masks to the one presented in Section 2.3.1 after taking into account the reduction in the number of available TVWS channels mentioned in Section 3.1.

3.3.1 Stage 1 Filter

Although the final implemented design on the FPGA does not include stage 1; it is used for simulation purposes allowing us to compare the performances, reconstruction and compliance to regulation, of the proposed design against a 64 channels FBMC system.

Design

As proposed in [54], the filter for stage 1 is designed using a mini-max method [97], the magnitude of the frequency responses for the 64-point and 40-point FBMC systems are shown in Figures 3.3 and 3.4 respectively. Due to the greater amount of unused channels the filter for the 64-point system exhibits a wider transition band compared to the filter for a 40-point system.

In both systems, the passband $B_{P,1}$ is selected to be 320 MHz wide and centered to 0, while the transition band width for a N_{FFT} points transform is computed as

$$B_{T,1} = \frac{40}{N_{\text{FFT}}K_1} \times f_s. \quad (3.20)$$

With a higher oversampling factor $K_1 = 6$ in stage 1, the 40 channels system requires a sharper transition band of $B_{T,1} = 240$ MHz than the 64 channels system. The latter

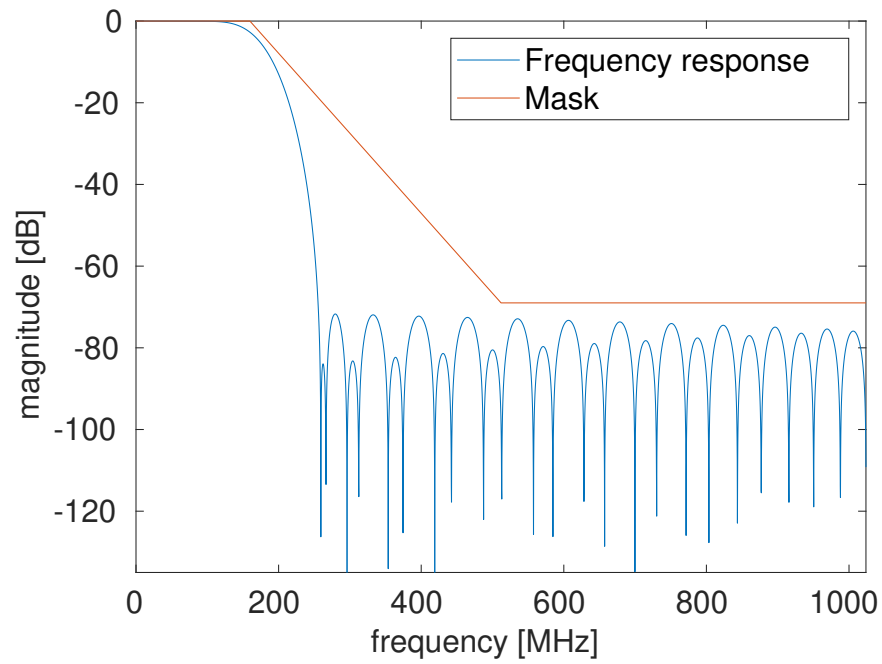


Figure 3.3: Stage 1 filter 64-point FFT FBMC frequency response $|H_1(e^{j2\pi f/f_s})|$ and corresponding spectral mask.

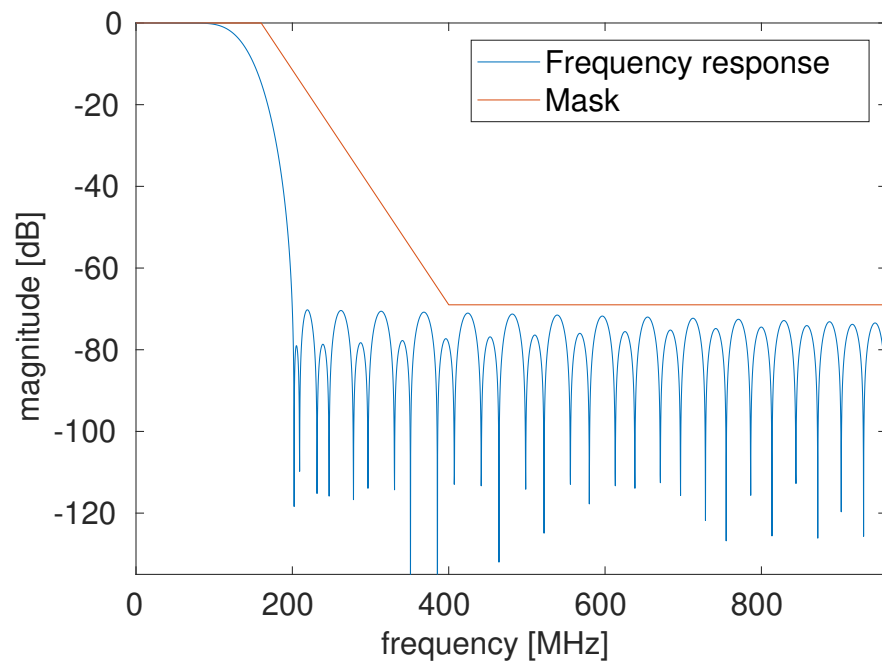


Figure 3.4: Stage 1 filter 40-point FFT FBMC frequency response $|H_1(e^{j2\pi f/f_s})|$ and corresponding spectral mask.

with its oversampling factor $K_1 = 4$, which combined with a higher number of unoccupied channels and overall higher sampling rate f_s of 2048 MHz against 1920 MHz at the output of stage 1, allows for a much wider transition band of $B_{T,1} = 352$ MHz. The stop-band is set to a minimum attenuation of 69 dB, which ensures that the system respect the emissions constraints set by the regulator: office of communications (OfCom) [22]. The pass-band constant across both design is set to cover 30 channel, i.e. 240 MHz.

Complexity

The 64-point system allows for a wider transition band $B_{T,1}$ in the design of the prototype filter h_1 , and thus permitting a shorter filter length than a 40-point system. However, the reduction in usable TVWS channels still provides the 40-point system with sufficient flexibility and transition bands for the design of the prototype filter h_1 . Supposing a polyphase implementation of the filter h_1 , the number of MAC required per second for stage 1 is computed as follow

$$C_{\text{MAC}} = L_1 \times K_2 \times 8 \text{ MHz} , \quad (3.21)$$

where L_1 is the length of the prototype filter h_1 , $K_2 = N_{\text{FFT}}$ the oversampling factor in stage 2 and 8 MHz the sample frequency of a single channel at the input of stage 2. The oversampling factor K_1 in stage 1 does not intervene in the complexity computation because of the poly-phase implementation of stage 1. Using the formula above and parameters presented in Table 3.1, one can determine the cost in kMAC/s of each system. The lower operating frequency $K_2 \times 8\text{MHz}$ of the stage 2 of the 40 channel results in a requirement of 20.8 kMAC/s, to be compared to the 30.72 kMAC/s needed for the 64 channels systems. This, despite the longer prototype filter for stage 1, leads to a cheaper implementation for the 40 channels system than the 64-point design.

3.3.2 Stage 2 Filter

The filters of stage 2 are designed using a least-square approach, the respective frequency responses $|P_2(e^{j2\pi f/f_s})|$ for the 64 and 40 channels systems are shown in Figures 3.5 and 3.6. The filter lengths L_2 , 360 and 384 coefficients for the 40 and 64 channels systems respectively, are chosen to simplify the implementation of stage 2 into a poly-phases network, as such $L_2 = l \times K_2$, $l \in \mathbb{N}$ and detailed in Section 3.4.2.

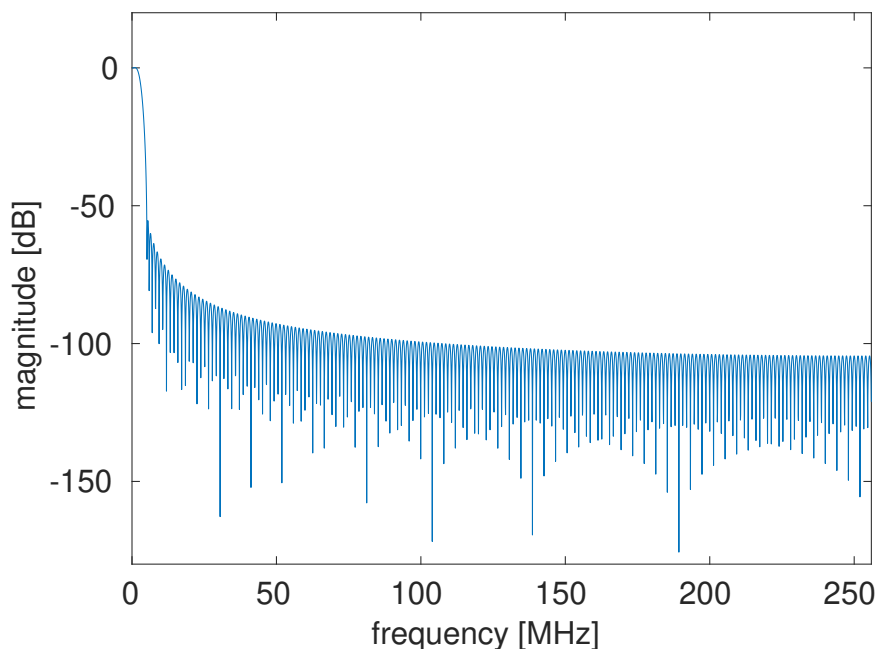


Figure 3.5: Stage 2 filter 64-point FFT FBMC frequency response $|P_2(e^{j2\pi f/f_s})|$.

3.4 FPGA Implementation

In the following, we simulate a TVWS transceiver using a Xilinx FPGA-based software defined radio (SDR) platform, presented in Section 2.2.2, the platform is composed of a ZC706 FPGA evaluation board and a radio frequency (RF) daughter-board AD-FMCOMMS4. While this SDR system can not cover the full TVWS spectrum, due to bandwidth limitations of the daughterboard, it is a typical setup for SDR, which shares its architecture with systems capable of higher performances such as the USRP N310. Furthermore, this system should be representative of a TVWS SDR transceiver, and could be easily scaled up using a high performance FPGA and RF daughterboard.

For this work, in order to reduce the system complexity and guarantee convergence of the synthesis and implementation algorithms, the FBMC system is implemented, as presented in Figure 3.7, i.e. without stage 1 or any of the annex subsystems required in a real-life scenario, including synchronisation and equalisation processes. All version of the system are designed using Simulink[®] models and then implemented using the SDR hardware (HW)/software (SW) codesign workflow from MATLAB[®], described in Section 2.2.3.

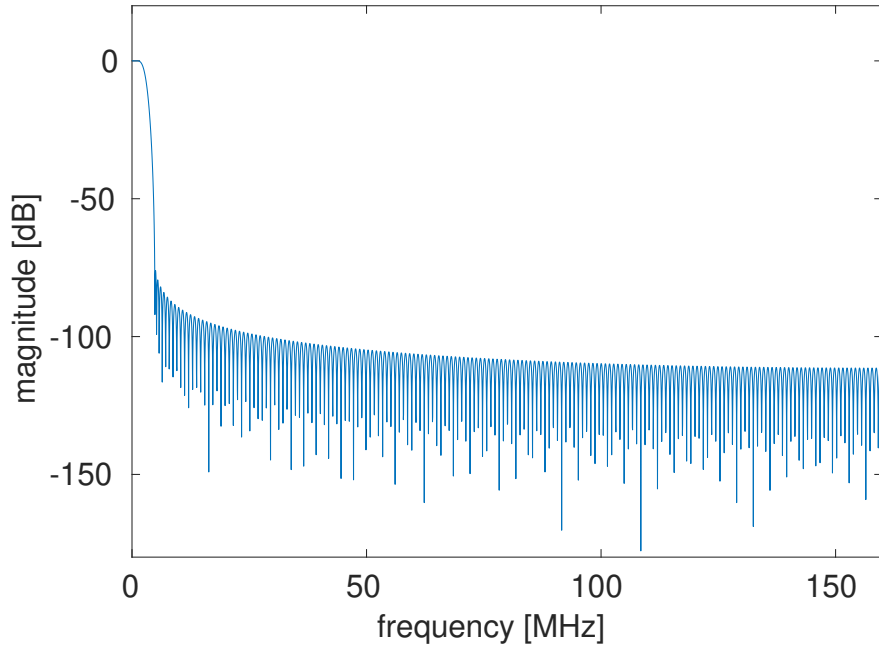


Figure 3.6: Stage 2 filter 40-point FFT FBMC frequency response $|P_2(e^{j2\pi f/f_s})|$.

3.4.1 Word-Length Considerations

In [54], it was established that in order to keep the out-of-band emissions to adjacent TVWS channels below the -69dB currently suggested by the regulator [61], a minimum word length of 12 bit must be used at RF. Incorporating the resolution gain in the up- and downconversion stages, samples and coefficients at baseband should be resolved with 16 bits. While these parameters are important, the wordlength limiting factors reside in the hardware, presented in Section 2.2.1. The DSP48E1 blocks of a Xilinx FPGA discourage word lengths above 18 bits [41, 42], additionally most digital-to-analogue converter (DAC) used in SDR platforms are limited to 14 bits, 12 bits for the

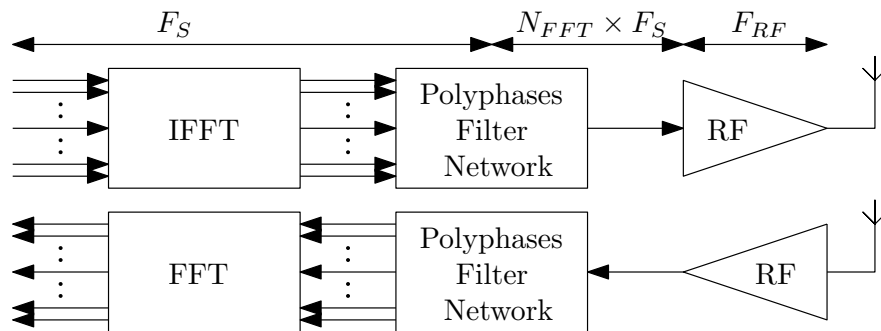


Figure 3.7: Oversampled FFT modulated FBMC system, as implemented in this work.

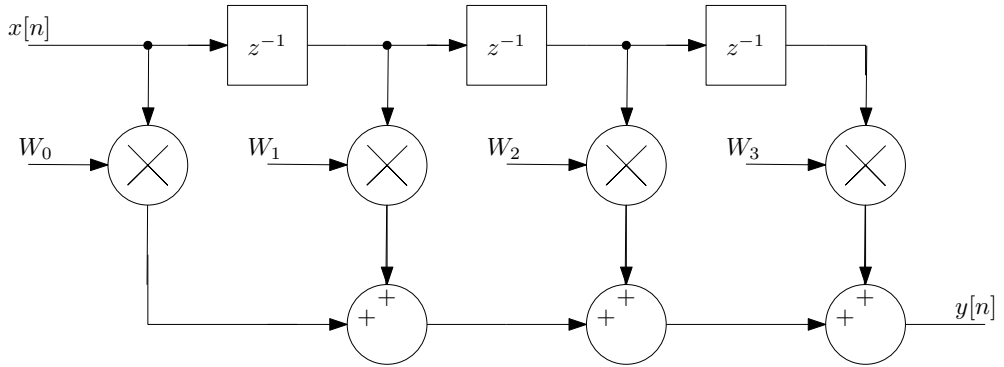


Figure 3.8: Implementation of a 4-tap direct-form finite impulse response (FIR) filter.

selected platform. For all implementations performed in this work, 18 bits is used as a generic wordlength upper bound across the entire system.

3.4.2 Serialisation of the Filters

FFT modulated FBMC systems can be implemented into the structures presented in Figure 3.10 and Figure 3.11 for the synthesis and analysis filter-banks respectively. This structure is however an inefficient implementation in terms of area usage on the FPGA, due to the high requirements in multipliers, furthermore the low operating frequency of such system does not take full advantage of the performance achievable by a modern FPGA.

The prototype filters for stage 2, i.e. p_2 , require a lot of MAC operations, most likely exceeding the DSP48E1 resources available on the FPGA, if the filter bank was to be implemented using this fully parallel structure from Figures 3.10 and 3.11. While the polyphase filter design of the FBMC system is based on the work presented in [57], here the use of multiplications has been serialised as much as possible to limit the number of DSP48E1s required, by way of approaches similar to the serialisation of the FIR filter in Figure 3.8 into the structure shown in Figure 3.9.

In Figure 3.9, considering a serialisation factor $l = 4$ the samples $x[n]$ are fed at a sampling frequency F_s into an addressable first-in first-out (FIFO) memory of width $K = \frac{L}{l} = 1$ and depth $l = 4$, where $L = 4$ is the filter length. The multiplier is provided with the sample $x[n]$ and corresponding coefficient w_n from their respective memory, addressed using a bounded (from 0 to $L - 1$) counter running at $l \times F_s$, the result of the multiplication is then passed to an accumulator, when the counter reaches l , the value $y[n]$ is output and the accumulator reinitialised at a frequency F_s , as a new

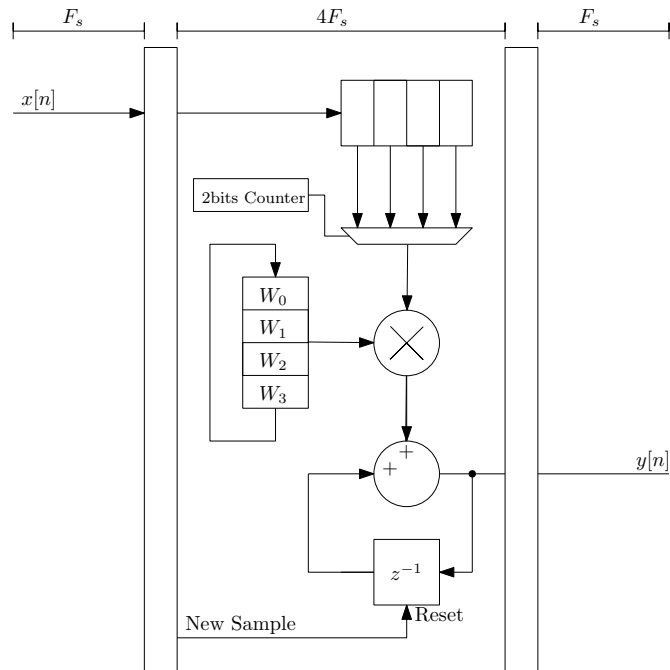


Figure 3.9: Implementation of a 4-tap FIR filter serialised by a factor of 4.

sample $x[n]$ comes in.

For simplicity of design, i.e. avoiding the introduction of various delays in the different branches of the polyphase architecture, the serialisation factor l is chosen such that the FFT length K_2 can be expressed as $K_2 = \frac{L_2}{l}, l \in \mathbb{N} \setminus \{0\}$. As the system is operating at a scaled down frequency and a relatively small FPGA a value of $l = K_2$ was used, but in a real system a factor $l = K_2/n, n \in \{2, 4, 8\}$ would be required to operate at a reasonable frequency for implementation onto an FPGA. The choice of a maximum serialisation is motivated by the relatively small FPGA on the used SDR platform in this experiment.

3.4.3 Transform Structure

In order to determine the most efficient implementation two structures for the considered FFTs are designed and implemented, a fully parallel version and a serial structure of the FFT presented in Figures 3.1 and 3.12 respectively. The serial version of the 40-point FFT uses a 5-point FFT block as first stage operating at eight times the input sampling frequency F_s of 8 MHz and a 8-point FFT running at five times the input sampling frequency as second stage. This design reduces the required number of multiplication slices by a factor of eight for the radix-5 stage and respectively five for the

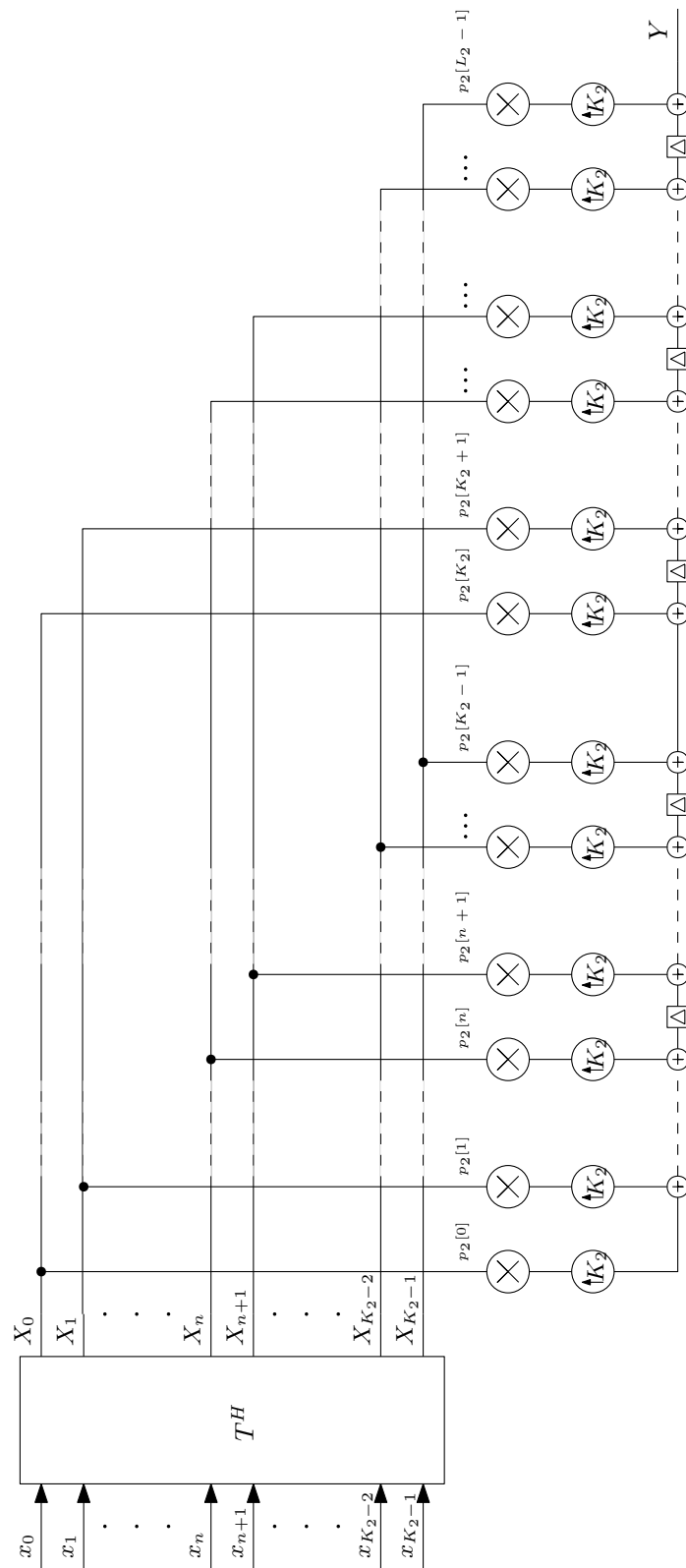


Figure 3.10: Unserialised FBMC synthesis bank.

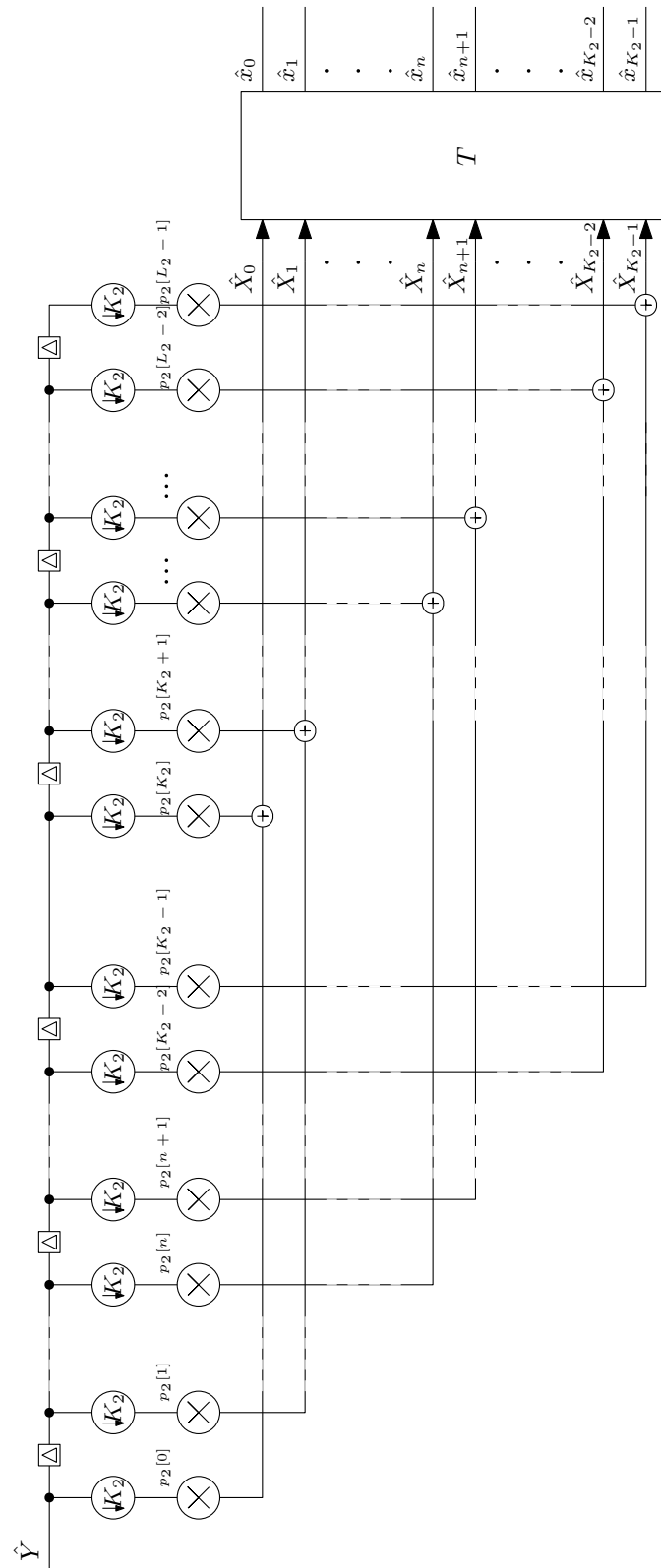


Figure 3.11: Unserialised FBMC analysis bank.

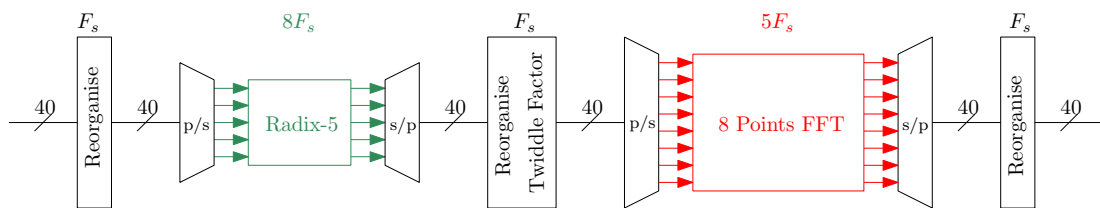


Figure 3.12: Serialised 40-point mixed-radix FFT.

8-point FFT stage, trading area usage for running frequency. Although this approach increase the latency of the overall system, it is deemed an acceptable trade-off.

3.5 Results

This section introduces the results for the implementation of various mixed-radix FFTs as the modulating transforms of oversampled DFT modulated FBMC systems.

3.5.1 System Performance

While the systems implemented on FPGA in this chapter do not include stage 1, it is added to the simulation designs in order to test compliance to OfCom regulations as well as reconstruction performance of the 40 and 64 channels systems.

Compliance to Spectral Requirement

The power spectral density (PSD) at the output of stage 1 is shown in Figures 3.13 and 3.14; the 40-point and 64-point systems both satisfy the requirement, when all TVWS channels are in use, by keeping emissions outside of the TV spectrum below -69 dB.

To test the compliance of out of band emissions between channels in the TVWS spectrum, data is first transmitted onto a single channel. Figures 3.15 and 3.16 show the output of stage 2 for the 40-point and 64-point systems respectively. The margins between the mask and the actual output of the system ensure that the spectral requirements are respected, even when multiple channels are used, as shown in Figures 3.17 and 3.18.

Reconstruction

To check the implementation and reconstruction performance of the system, 30 randomly generated quadrature phase-shift keying (QPSK) signals, fully occupying the TV

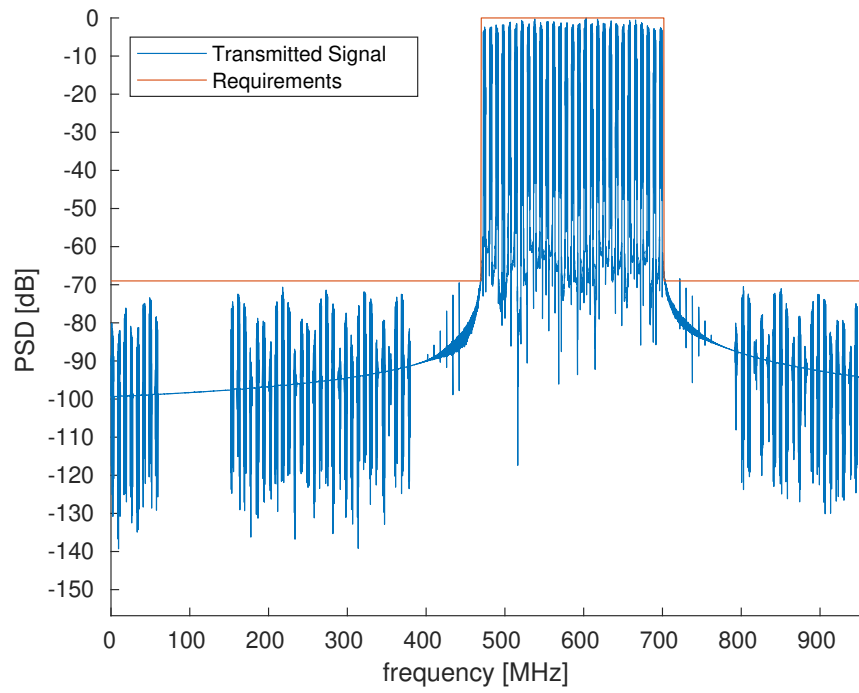


Figure 3.13: PSD after stage 1 in 40-point system, all available channels active.

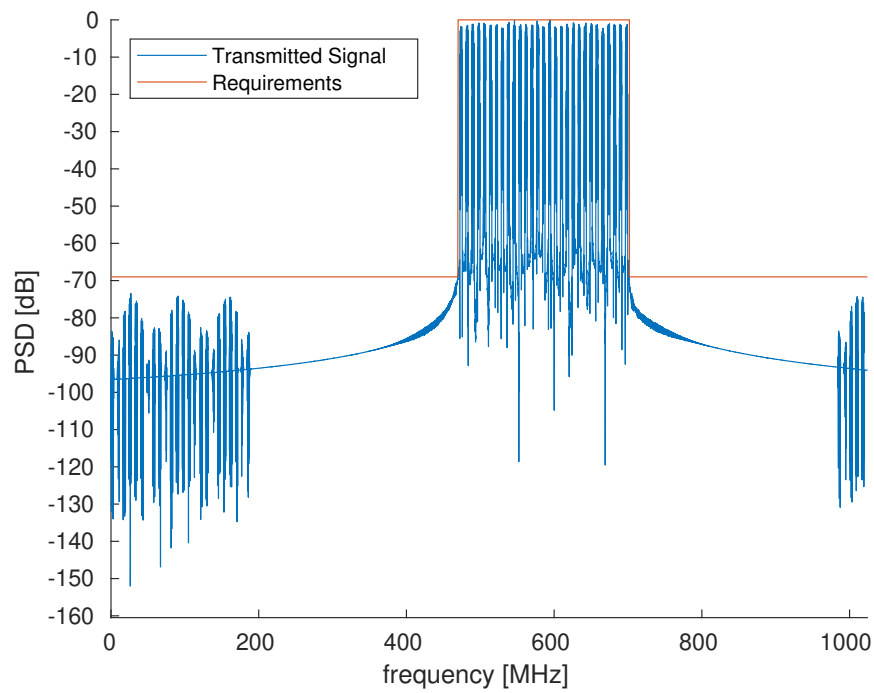


Figure 3.14: PSD after stage 1 in 64-point system, all available channels active.

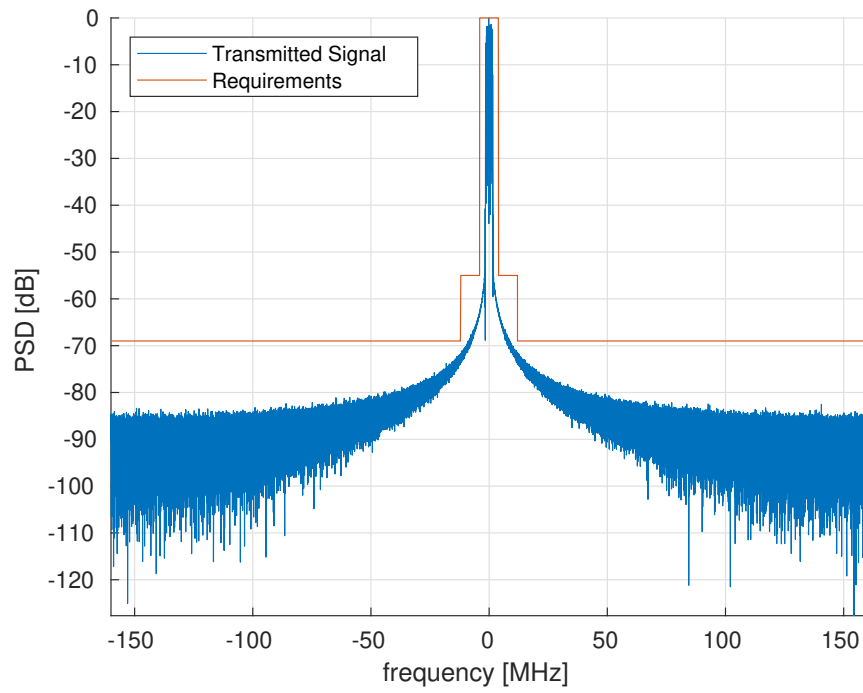


Figure 3.15: PSD after stage 2 in 40-point system, 1 active channel.

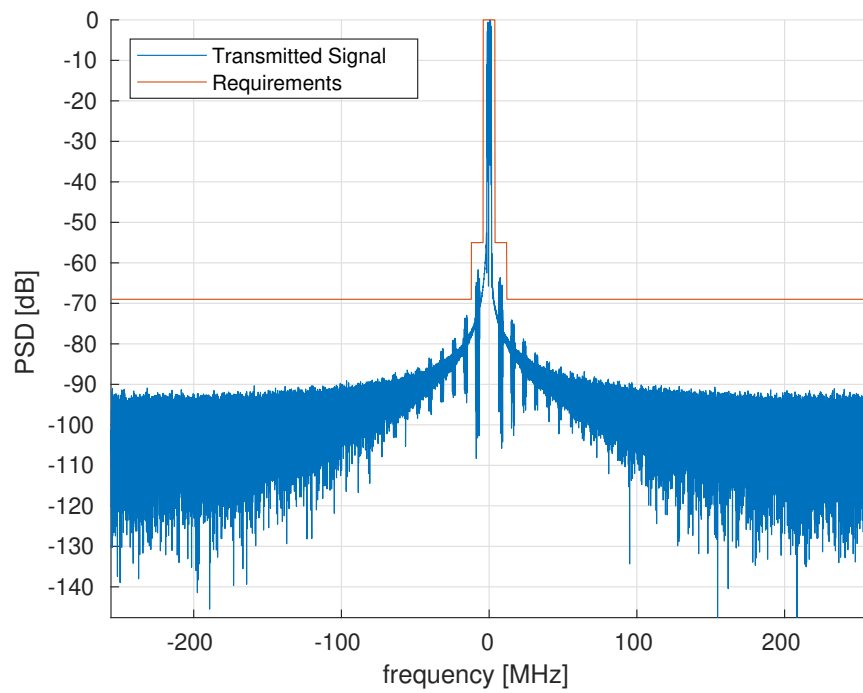


Figure 3.16: PSD after stage 2 in 64-point system, 1 active channel.

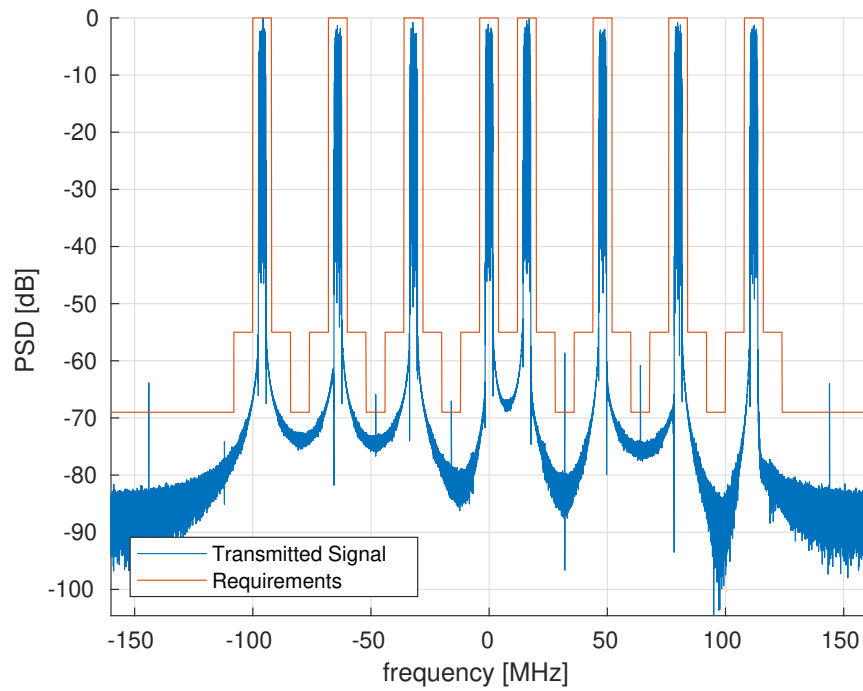


Figure 3.17: PSD after stage 2 in 40-point system, 8 active channels.

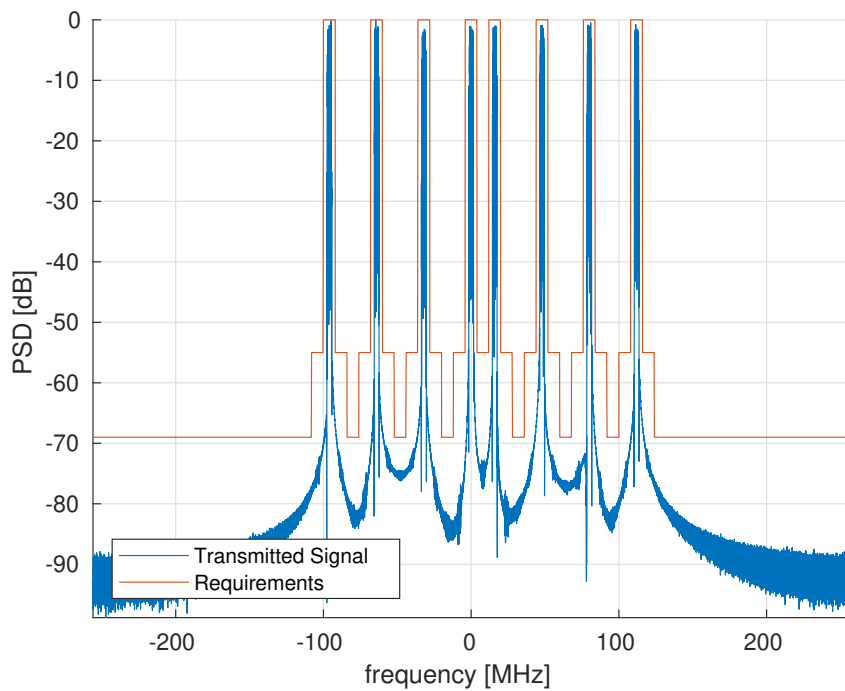


Figure 3.18: PSD after stage 2 in 64-point system, 8 active channels.

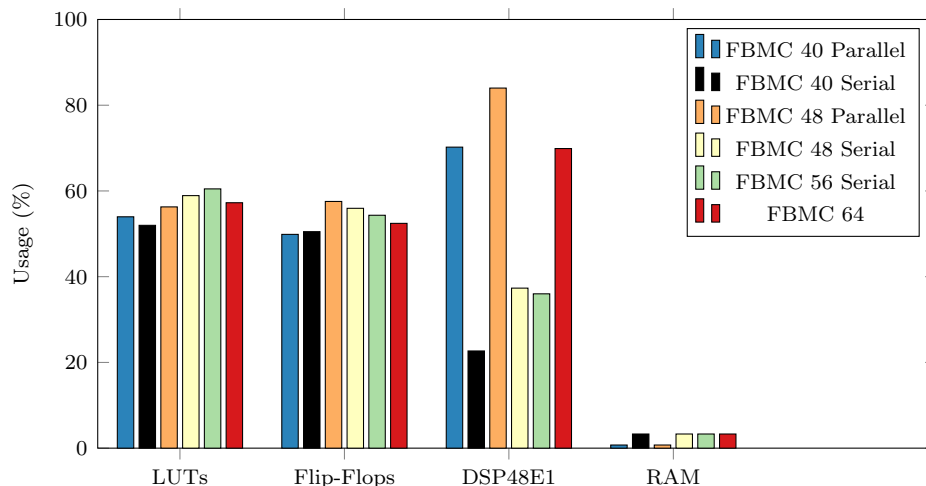


Figure 3.19: Area usage on Zynq Z7045, are displayed the main type of resources: look-up table (LUT), flip-flops, DSP48E1 and RAM blocks.

spectrum, are transmitted. The transmission channel impulse response is composed of a single sample delayed impulse, such as the system is perfectly synchronised, allowing for optimum reconstruction. A reconstruction error is computed as follows:

$$e_n[t] = 20 \times \log_{10} \left(|\hat{x}_n[t - \delta_t] \times e^{j\phi_n} - x_n[t]| \right), \quad (3.22)$$

where $x_n[t]$ is the input signal of the n^{th} channel on the transmitter side and $\hat{x}_n[t]$ the corresponding output channels on the receiver side after timing adjustment δ_t and constant phase correction ϕ_n . The implemented systems provide an average of -25 dB and -33 dB of reconstruction error across all channels for the 64 and 40 channels systems respectively, largely sufficient to ensure a bit error rate (BER) equal to zero when using a QPSK modulation scheme.

3.5.2 Footprint

The area used on the FPGA, by each of the implemented systems is presented in Table 3.2 and Figure 3.19, where "FBMC N " designates the system using an N -point fully parallel FFT and "FBMC N Serial" the serialised version of the transform as introduced in Section 3.4.3, i.e. by using a single transform block per stage within a transform, as in Figure 3.12. For signal processing applications the most critical resources on a FPGA are the MAC units, as highlighted in Section 2.2.1 contained in the DSP48E1 slices of Xilinx's FPGAs. To that respect, the serialised versions of the FFT have proved more resource-efficient than their parallel counterparts, allowing the

Table 3.2: Oversampled FFT modulated FBMC, FPGA area footprint, Xilinx Z7045.

FPGA resource	LUTs	Flip-Flops	DSP48E1	RAM
available	214065	437200	900	545
FBMC 40 Parallel	117989	218017	632	4
FBMC 40 Serial	113621	220783	204	18
FBMC 48 Parallel	123033	251615	756	4
FBMC 48 Serial	128770	244616	336	18
FBMC 56 Serial	132220	237517	324	18
FBMC 64	125144	229289	629	18

larger transforms, such as the the 56-point and 64-point FFT to fit on the FPGA, when a parallel version would use more resources than available. The reduced use of DSP48E1 however comes at the price of an increase in the number of random access memory (RAM) slices necessary; they are most likely mapped to the serial-to-parallel and parallel-to-serial conversions. This trade-off is however very advantageous as it make use of an otherwise unused resource, allowing to reassign the DSP48E1 block for other tasks, such as equalisation and/or synchronisation [1, 98, 99], which will be presented in Chapter 4.

The most area-efficient version of the system is the FBMC system implementing the 40-point serial version of the FFT, showing reduced slice use against the 64-point FFT version in all type of resources.

3.5.3 Power Consumption

Power consumption data is obtained using the implemented power report from Vivado and results are shown in Figure 3.20, to help with clarity only the FPGA dynamic power consumption is displayed. The overall power consumption can be deduced by adding the Zynq z7045 static overhead of 230mW, the advance reduced instruction set computing (RISC) machine (ARM) processor consumption of 1.57W and a 100mW off-chip consumption to the figures displayed in Figure 3.20, adding 1.9W to reach the total power consumption of the ZC706 board.

The results shown in Figure 3.20 confirm the conclusions of Section 3.5.2, as the 40-point FFT serial version is the most energy efficient solution, with a 230mW saving compared to the previously designed 64-point version [54]. In those experiments, the area usage is the most critical variable when it comes to the power consumption. While the increase of the working frequency leads to a higher power consumption from

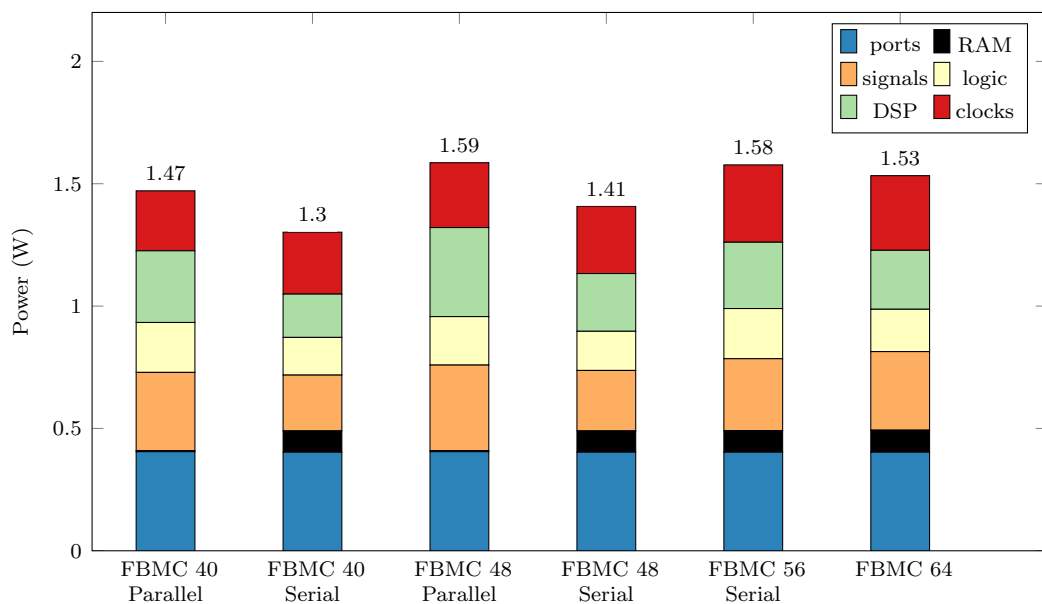


Figure 3.20: Dynamic power consumption estimate, for each of the proposed designs.

the clocks and the signals (transfers of data between slices), the saving on the power consumption of the DSP48E1 slices largely counterbalances the increase related to the augmentation of the processing rate.

The lower computational efficiency of the non power-of-two FFTs, i.e. the number of operation per FFT coefficient, makes the 48-point FFT parallel and 56-point FFT serial version less energy-efficient, once again showing a strong correlation between the resources utilisation shown in Table 3.2 and the power consumption.

3.6 Chapter Summary and Conclusions

In this chapter a new approach to the design and FPGA implementation of oversampled FBMC systems for TVWS transmission is provided, by moving away from the standard power-of-two FFT and considering a 40-point mixed-radix FFT. This approach, when implemented on a Zynq z7045, has proven to be both less costly in terms of computational resources and more energy-efficient by 230mW, representing a 6.7% energy saving for the overall transceiver compared to previous designs. In a complete transceiver system, i.e. including stage 1 as well as equalisation and synchronisation, the later detailed in Chapter 4, this proposed approach might prove even more advantageous as systems upstream of the FBMC system in the receiver would run at a sampling frequency 30% lower than a 64-point FFT system [2].

Chapter 4

Per-Band Equalisation for Oversampled FBMC Systems

This chapter introduces a new approach to the equalisation of a single channel of a fast Fourier transform (FFT) modulated oversampled filter-bank multi-carrier (FBMC) system, this study is completed by an field programmable gates array (FPGA) implementation. Equalisation performance, implementation cost and power consumption estimations are compared with state-of-the-art approaches. The proposed equaliser relies on a concurrent constant modulus (CM) and decision directed (DD) algorithm in a fractionally-space structure, offering better equalisation performance in simulation than a classic CM algorithm. Section 4.1 introduces the motivations for this work, while the considered equaliser design is described in Section 4.2. The implementation cost and algorithm performance are presented in Section 4.4, with details on the methodology used for the FPGA implementation are given in Section 4.3. As this work pre-dates the designs in Chapter 3, the implemented equalisers were tested with a 64 channels multicarrier system as presented in [54].

4.1 Motivation and Rationale

Compared to orthogonal frequency-division multiplexing (OFDM), FBMC system are generally expected to be more robust to synchronisation errors [100]. Critically sampled FBMC approaches such as FBMC offset-quadrature amplitude modulation (OQAM) still suffer from inter-carrier interference (ICI), and the advantage of high spectral efficiency comes at the cost of a complicated equaliser requiring cross-terms between at least adjacent channels [74, 75]. In contrast, the oversampled FBMC systems considered in this thesis can include a guard band, and even in a doubly-dispersive channel, ICI can be assumed negligible.

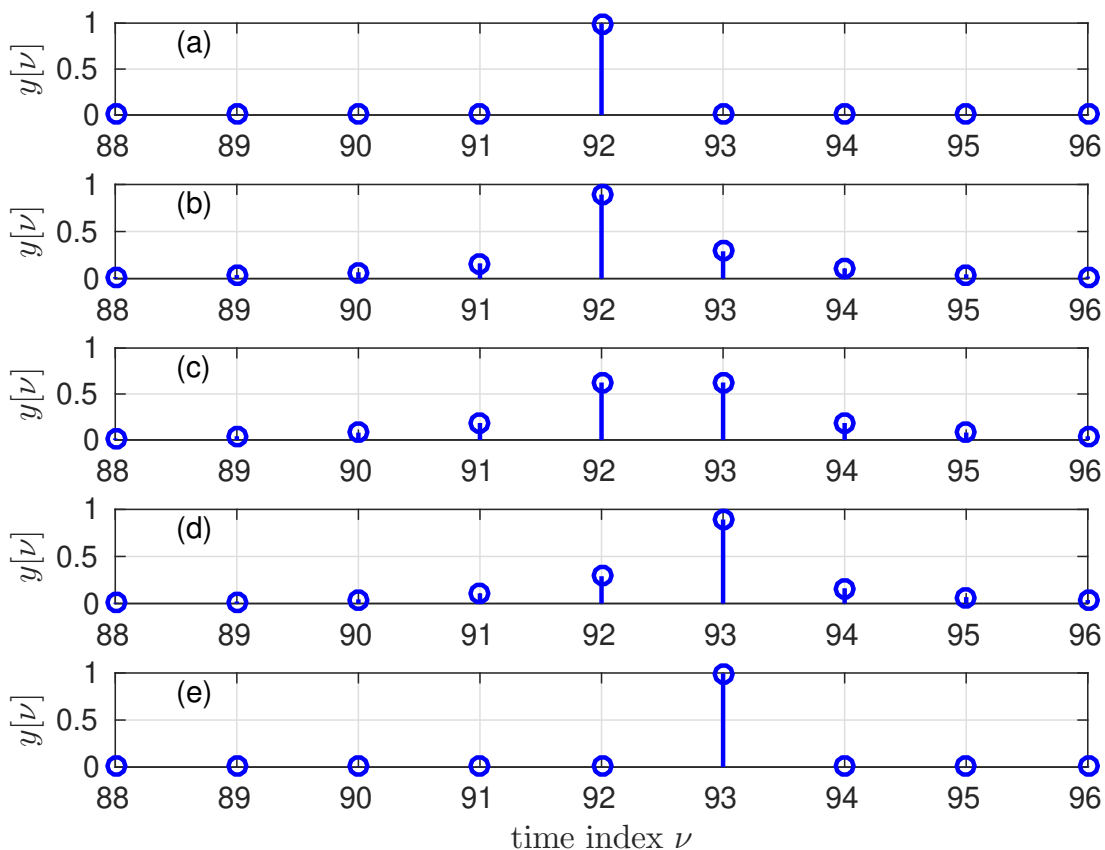
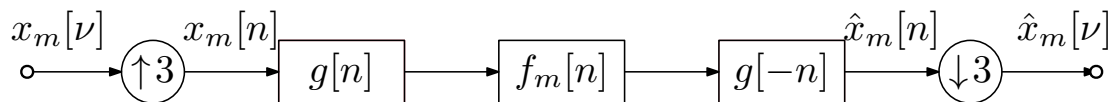


Figure 4.1: Example of impact of radio frequency (RF) delays of (a) 0, (b) 96, (c) 192, (d) 288, and (e) 384 samples on the impulse response of a transceiver system subchannel impulse response.

Even though subchannels in FBMC systems can be treated as independent from each other, i.e. without the use of cross-terms, they still are broadband. As such they exhibit frequency-selective fading in dispersive channels, and hence must be equalised. In the absence of dispersive channel conditions, the FBMC system still requires careful synchronisation, as the sampling point is critical [101].

Figure 4.1 shows the impact of different delays in the RF path on the overall response of one subchannel from transmitter to receiver for a 64-point FBMC system as implemented in [54] and Chapter 3, with filter $h_1[\ell]$ and $p_2[n]$, described in Section 2.3, being $K_1^{(i)}$ and $K_2^{(i)}/2$ -band systems respectively. To fit a simple wideband signal into an 8 MHz wide TV white space (TVWS) channel, a 5.3 MHz single carrier signal $x[\nu]$ is used in a $1/3^{\text{rd}}$ -band square-root Nyquist system $g[n]$. Figure 4.2 shows the transmission over the m^{th} subchannel $f_m[n]$ running at 16 MHz by means of matched

Figure 4.2: Transmission over the m th subchannel $f_m[n]$.

transmitter and receiver filters; the latter form a 3-band Nyquist system, with inputs and outputs $x[\nu]$ and $\hat{x}[\nu]$ operating at a sampling rate of $5.\bar{3}$ MHz. With respect to this baseband signal, a delay at RF translates into a fractional delay [102], which even in a non-dispersive channel can introduce significant inter-symbol interference (ISI), hence motivating the use of an equaliser for each individual subcarrier.

4.2 Equaliser Design

This section gives details on the equaliser design selected for this study.

4.2.1 Equaliser Structure

To be robust towards the type of fractional delays shown in Figure 4.1 that a dispersive channel and/or unsynchronised transceiver system cause at baseband, this work employs a fractionally-space equaliser (FSE). While a symbol-spaced equaliser would generally be required to be of infinite length, with a FSE an exact inverse exists for a finite length equaliser, provided that the roll-off of the receiver filter — shown as $g[-n]$ in Figure 4.2 — is not too steep. For fractionally spaced equalisation, there generally is no advantage to go beyond a twice oversampled, or $T/2$ -spaced system, but because of the fact that the subchannel data in this implementation is clocked at $5.\bar{3}$ MHz, here a thrice oversampled or $T/3$ -spaced fractional equaliser is used.

The polyphase representation of this equaliser is shown in Figure 4.3, with the three polyphase components $w_{m,i}[\nu]$, $i = \{0, 1, 2\}$ and $m \in \{1, 2, \dots, 40\}$ the channel number, such as the oversampled time index n is defined as $n = 3\nu + i$, followed by a carrier frequency and phase correction $\phi_m = \Omega_{\Delta,m} + \varphi_m$ to compensate for potential carrier frequency and phase offsets $\Omega_{\Delta,m}$ and φ_m , respectively.

4.2.2 Concurrent Constant Modulus / Decision Directed Algorithm

In order to implement a robust synchronisation and equalisation scheme, this work opts for a blind approach based on the CM algorithm [103], described in Section 2.4, which is applicable to CM constellations such as quadrature phase-shift keying (QPSK). The CM algorithm adapts relatively slowly compared to schemes such as the least mean

square (LMS) algorithm; to increase the convergence rate, the CM update is combined with a DD process. The DD approach however requires the equaliser to be already sufficiently well adjusted such that correct decisions are reached at its output. A suitable approach to combine the strength of both CM and DD approaches is by means of a concurrent adaptation [80, 104]. In the concurrent CM/DD algorithm, every iteration first involves a CM update step; if the CM process is deemed to guarantee a correct decision, an additional DD update step is performed.

The use of a concurrent CM/DD architecture allows to blindly equalise the received signal, it however leaves the signal with a constant rotation in the constellation. While this could be an issue in other applications, in a wireless broadband system the rotation could be corrected using known characteristics of the signal such as start of frame sequences.

A concurrent CM/DD algorithm splits the coefficients $\mathbf{w}_{m,i}$ of the equaliser into two components,

$$\mathbf{w}_{m,i}[\nu] = \mathbf{w}_{m,i}^{(\text{CM})}[\nu] + \mathbf{w}_{m,i}^{(\text{DD})}[\nu], \quad (4.1)$$

where $\mathbf{w}_{m,i}^{(\text{CM})}[\nu]$ is updated by a CM algorithm, and $\mathbf{w}_{m,i}^{(\text{DD})}[\nu]$ is adjusted in DD mode. A length $L_{m,i}$ is assumed for each polyphase components, such that $\mathbf{w}_{m,i}^{(\text{CM})}[\nu], \mathbf{w}_{m,i}^{(\text{DD})}[\nu] \in \mathbb{C}^{L_{m,i}}$. The equaliser output is calculated as

$$v_m[\nu] = \sum_{i=0}^2 \mathbf{w}_{m,i}^H[\nu] \mathbf{x}_{m,i}[\nu], \quad (4.2)$$

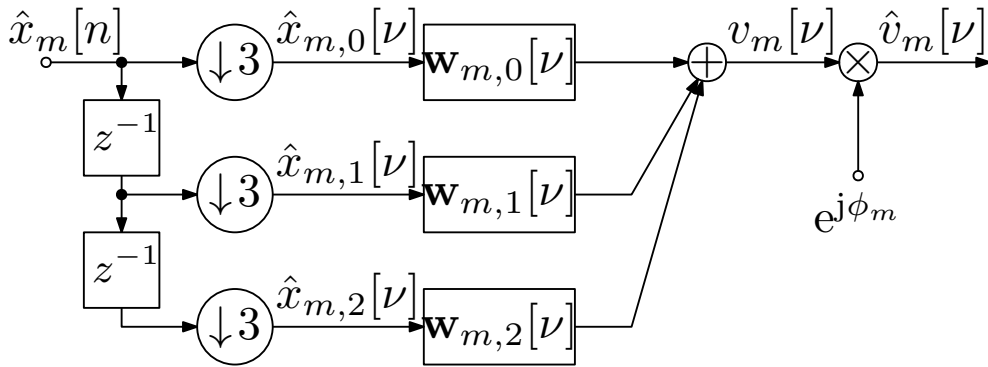


Figure 4.3: $T/3$ -spaced subchannel equaliser with carrier frequency and phase correction, and decision device.

where $\mathbf{x}_{m,i}[\nu]$ is a tap-delay-line vector containing a data window of the polyphase signal $\hat{x}_{m,i}[\nu]$ in Figure 4.3, such that

$$\mathbf{x}_{m,i}[\nu] = \begin{bmatrix} \hat{x}_{m,i}[\nu] \\ \hat{x}_{m,i}[\nu - 1] \\ \vdots \\ \hat{x}_{m,i}[\nu - L_{m,i} + 1] \end{bmatrix}. \quad (4.3)$$

The output $\hat{v}_m[\nu]$ is obtained after correction of the constant rotation ϕ_m of the constellation such as,

$$\hat{v}_m[\nu] = v_m[\nu]e^{j\phi_m}. \quad (4.4)$$

The CM-part coefficients of the equaliser are updated using the update equation defined in Section 2.4, leading within the FSE structure to

$$\mathbf{w}_{m,i}^{(\text{CM})}[\nu + 1] = \mathbf{w}_{m,i}^{(\text{CM})}[\nu] + \Delta\mathbf{w}_{m,i}^{(\text{CM})}[\nu] \quad (4.5)$$

with

$$\Delta\mathbf{w}_{m,i}^{(\text{CM})}[\nu] = \mu_{\text{CM}}(1 - |v_m[\nu]|^2)v_m^*[\nu]\mathbf{x}_{m,i}[\nu]. \quad (4.6)$$

The adjustment related to the DD process of the equaliser coefficients in $\mathbf{w}_{m,i}[\nu]$ requires a decision device $\mathcal{F}(\cdot)$, which e.g. for QPSK constellation takes the form

$$\mathcal{F}(v_m[\nu]) = \frac{1}{\sqrt{2}}\{\text{sgn}(\text{Re}\{v_m[\nu]\}) + j \cdot \text{sgn}(\text{Im}\{v_m[\nu]\})\}, \quad (4.7)$$

with the signum function

$$\text{sgn}\{a\} = \begin{cases} -1, & a < 0 \\ 0, & a = 0 \\ +1, & a > 0, \end{cases} \quad (4.8)$$

for $a \in \mathbb{R}$. This function allows to accurately equalise rotation of the received signal contained in $[0; \frac{\pi}{2}[$ for a QPSK signals. For the DD part of the algorithm, the update of the coefficients $\mathbf{w}_{m,i}^{(\text{DD})}[\nu]$ is performed using the indicator function

$$\delta b = |b| > \varepsilon \quad (4.9)$$

with $b \in \mathbb{C}$ and ε a very small constant. The indicator function enables the DD update

if the CM update is deemed to have reached a correct decision. Whether or not a correct decision has been reached is assessed by whether or not the CM update alters the result of the decision device \mathcal{F} in (4.7). Then the update for the DD component of the equaliser is expressed as,

$$\mathbf{w}_{m,i}^{(\text{DD})}[\nu + 1] = \mathbf{w}_{m,i}^{(\text{DD})}[\nu] + \mu_{\text{DD}} \Delta \mathbf{w}_{m,i}^{(\text{DD})}[\nu], \quad (4.10)$$

with μ_{DD} the update step size and

$$\Delta \mathbf{w}_{m,i}^{(\text{DD})}[\nu] = \delta \left(v_m[\nu] - \mathcal{F}(v_m^{(\text{CM})}[\nu]) \right) \cdot (\mathcal{F}(v_m[\nu]) - v_m[\nu])^* \mathbf{x}_{m,i}[\nu], \quad (4.11)$$

with the output of the CM part of the equaliser

$$v_m^{(\text{CM})}[\nu] = \sum_{i=0}^2 \left(\mathbf{w}_{m,i}[\nu] + \Delta \mathbf{w}_{m,i}^{(\text{CM})}[\nu] \right)^{\text{H}} \mathbf{x}_{m,i}[\nu]. \quad (4.12)$$

In addition to increasing the rate of convergence of a standard CM algorithm, the inclusion of a DD scheme also partially locks the phase ambiguity. This equaliser is referred to as FSE-CM/DD. The concurrent scheme can be reconfigured easily into a pure FSE-CM equaliser by setting $\mu_{\text{DD}} = 0$.

4.3 FPGA Implementation

This section presents the FPGA realisation of the equaliser described in Section 4.2 on a Xilinx Virtex 7. The use of a Virtex 7 instead of the Zynq 7 introduced in Section 2.2 is justified by the fact that this work pre-dates the work in Chapter 3 and that the Zynq based platform had not yet been selected at the time of the work presented in this chapter, motivating the use of a platform employed in a previous study [54]. Furthermore, the similarities between the Virtex 7 and Zynq 7 architecture make it likely that the result of the synthesis and implementation would be similar in terms of resource usage from one device to the other. This work used the hardware description language (HDL) Coder Blockset from Simulink[®] and the code generation tools to export the models to very high speed integrated circuit (VHSIC) HDL (VHDL). Thereafter, the generated code is forwarded to the Vivado tools for synthesis and implementation.

4.3.1 Word-Length Considerations

As described in Chapters 2 and 3 and established in [54], to keep the out-of-band emissions to adjacent TVWS channels below the -69 dB currently suggested by the

regulator [61], at RF a word length of 12 bits must be used. Incorporating the resolution gain in the up- and downconversion stages, samples and coefficients at baseband should be resolved with 16 bits. With the DSP48E1 block of a Xilinx FPGA discouraging word lengths above 18 bits, the following word lengths have been selected for the various equalisers. Based on the unit norm of the QPSK signal transmitted and received, it is deemed sufficient to employ 18 bits words with 4 integer and 14 fractional bits, which provides adequate amplitude and precision during simulations. With 18 bits representations of the filter coefficients for CM and FSE-CM equalisers lacking precision in the feedback loop, larger words (36 bits) have to be used for the adaptive filter coefficient in order to provide sufficient convergence. The inclusion of the DD-mode in the coefficient update reduces the dynamic range in the feedback path and permits a restriction to 18 bits words for the filter coefficients of the FSE-CM/DD equaliser.

4.3.2 Step Size Representation

To keep the propagation time in the feedback loop of the adaptive algorithms low, the step sizes μ_{CM} and μ_{DD} are chosen as powers of two. Multiplications therefore can be replaced by logic shifts, which in turn results in a shortening of the critical path in the FPGA realisation. In contrast, a long feedback loop requiring pipelining is likely to slow convergence, particularly for the DD scheme when based on the LMS coefficient update [81].

4.4 Results

This section presents the equalisation performance of the algorithm and the implementation cost on FPGA, compared to other state-of-the-art approaches.

4.4.1 Performances

This section details the equalisation performance for the FSE-CM/DD algorithm; the considered implementation uses a 24 coefficients equaliser based on the fixed-point design, laid out in Section 4.3.1. The equaliser outputs after rotation correction, $\hat{v}_m[\nu]$ is compared to the transmitted sequence $x_m[\nu]$. The error $e[n]$ after identifying the delay τ is defined at steady state such that

$$E\{|e_m[\nu]|^2\} = \min_{\nu, \tau \in \mathbb{Z}} E\{|x_m[\nu] - \hat{v}_m[\nu - \tau]|^2\} , \quad (4.13)$$

where $E\{\cdot\}$ is the expectation over time. The convergence curves are averaged over different RF channel realisations with randomised propagation delays, and different levels

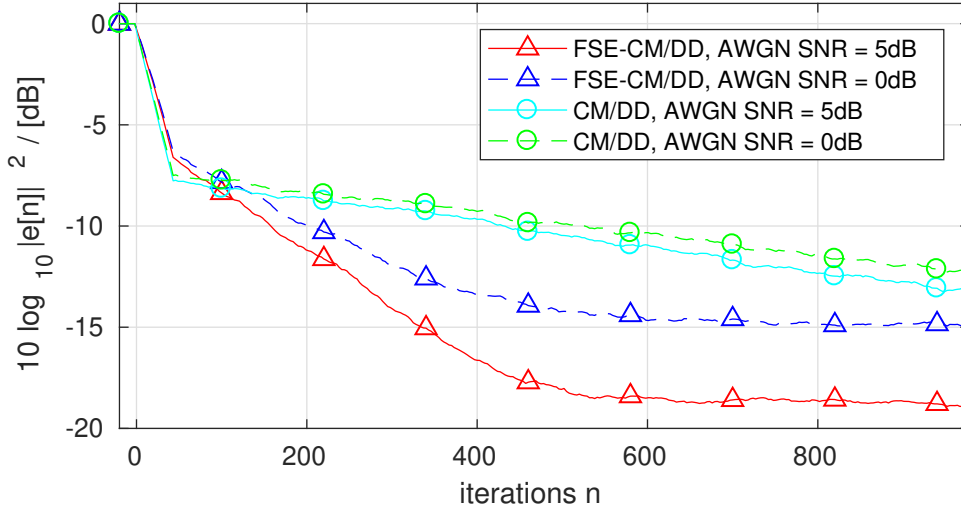


Figure 4.4: Results for FSE-CM/DD adaptive algorithm, showing ensemble-averaged errors for different SNRs.

of interference by additive white Gaussian noise (AGWN) applied to the transmitted signal at RF. Note that the applied noise is wideband at the RF sampling rate; while signal-to-noise ratio (SNR) figures may appear low, a large proportion of the noise is out-of-band w.r.t. the considered TVWS channels, and its impact reduced by the over-sampling resulting from the conversion.

Figure 4.4 shows the performance of a CM/DD algorithm with respect to the error defined in (4.13). The ensemble-averaged error converges reasonably quickly due to the concurrent CM/DD scheme, which maintains the robustness of the CM algorithm while offering the enhanced convergence speed of a DD update. The DD process removes some of the phase ambiguity of the CM scheme, and locks rotations of the QPSK constellation, with respect to the input signal. Although not shown here and despite the greater phase ambiguity, a sole CM scheme compares poorly in terms of convergence rate to the CM/DD approach. For CM/DD, the steady-state error generally improves with increased SNR, but has been found to saturate above 5 dB here due to a truncation of the ideal equaliser, which generally would require more than 8 coefficients per polyphase component.

Table 4.1: Resources requirements CM algorithm, Virtex 7 7VX550T.

FPGA Resources	Number used	Available	Percentage used
LUTs	7098	554240	1.28%
Flip-Flops	2561	692800	0.37%
DSP48E1	294	2880	10.21%

Table 4.2: Resources requirements FSE-CM, Virtex 7 7VX550T.

FPGA Resources	Number used	Available	Percentage used
LUTs	5375	554240	0.97%
Flip-Flops	2804	692800	0.4%
DSP48E1	294	2880	10.21%

4.4.2 Footprint

The resources used for the implementation of the symbol-spaced CM, FSE-CM, symbol-spaced CM/DD and FSE-CM/DD equalisers are summarised in Table 4.1, Table 4.2, Table 4.3 and Table 4.4 respectively, listing look-up tables (LUTs), flip-flops and DSP48E1 slices. For the symbol space systems, CM and CM/DD, the length of the equaliser, $L_m = 24$ is equal to the sum of all polyphase components $L_{m,i} = 8 \ i \in \{0, 1, 2\}$, i.e. $\sum^i L_{m,i} = L_m = 24$, for the corresponding fractionally spaced systems, FSE-CM and FSE-CM/DD.

Since the overall number of coefficients is the same, there is no cost disadvantage in going from a symbol-spaced to the $T/3$ -spaced equaliser. Further, the inclusion of the DD mode is advantageous, as it permits to lower the wordlength and this leads for the FSE-CM/DD algorithm to a reduction by 22% of the DSP48E1 blocks needed, 26% for the flip-flops and 42% for the LUTs when compared to the CM/DD system.

Table 4.3: Resources requirements CM/DD, Virtex 7 7VX550T.

FPGA Resources	Number used	Available	Percentage used
LUTs	3714	554240	0.67%
Flip-Flops	1864	692800	0.27%
DSP48E1	202	2880	7.01%

Table 4.4: Resources requirements FSE-CM/DD, Virtex 7 7VX550T.

FPGA Resources	Number used	Available	Percentage used
LUTs	4441	554240	0.80%
Flip-Flops	1916	692800	0.28%
DSP48E1	204	2880	7.1%

4.4.3 FPGA Timing Constraints

Information about the implementation's timing is obtained from Xilinx Vivado, with a longest logical propagation delay of 9.3ns and 12ns for the FSE-CM/DD and CM/DD algorithms, respectively, the system can easily be executed within the 188ns sampling period of the 5.3 MHz system.

4.4.4 Power Consumption

For the generated VHDL code of the equalisers, Xilinx Vivado allows to assess the power consumption. In addition to a static power consumption of 327mW of the Virtex 7, Figure 4.5 shows the dynamic power consumption. Of the different equalisers, the FSE-CM/DD is the most energy efficient, requiring approximately 30% less than the symbol-spaced CM implementation for the same number of coefficients.

As in Chapter 3, the main source of power consumption are the DSP48E1 units, which are approximately the same for all designs. However, the FSE approaches operate three branches in parallel, thus reducing the overall length of the logic path. Since each branch is shorter, hardware resources for each branch are more compactly placed in terms of area compared to a single branch, permitting shorter interconnections

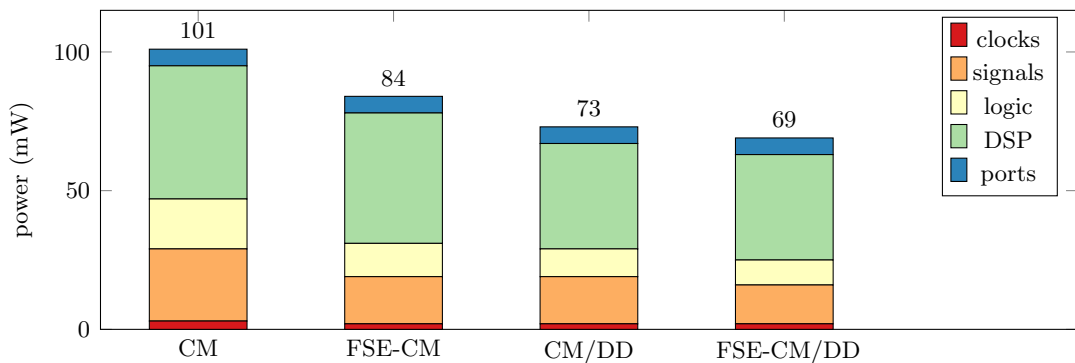


Figure 4.5: Dynamic power consumption of different equalisers.

within the FPGA, as shown by the signalling related part of the power consumption in Figure 4.5. As interconnections are expensive in terms of energy, reducing these also diminish the power consumption of the FSE designs.

4.5 Chapter Summary and Conclusions

This work focused on a low-complexity equalisation for an oversampled FBMC system used as frequency-agile TVWS transceiver system. In order to enable transmission, a per-band equalisation and synchronisation has been introduced. Amongst different options, we have selected a robust and fast blind approach based on a fractionally-spaced concurrent CM and DD algorithm.

The selected approach is capable of synchronising and equalising a frequency-selective channel. The use of a fractionally-spaced architecture has demonstrated advantages in terms of power consumption, when compared to a symbol-spaced approach based. Furthermore, the concurrency of a DD scheme together with a CM approach permits a lower bit resolution compared to a pure CM approach, hence also resulting in a lower implementation cost. The implementation cost of presented algorithm added to that of the system implemented in Chapter 3 has demonstrated that a number of equaliser can be operated together with the transceiver system on a Xilinx Virtex 7, and enable low-power base stations.

Chapter 5

Multi-Radio Access Network Assignment

This chapter introduces two new approaches to the user assignment problem for off-grid base station using multiple radio access technology (RAT), used to provide broadband access to remote communities. The base station is powered by renewable energy harvesters. A resources management scheme based on detailed modelling and using a dynamic programming algorithm is proposed. The two proposed schemes differ by the formulation of the respective optimisation problems: one implements a cost function influenced solely by load balancing between the radios, while the second also takes into account a power consumption related cost. The proposed schemes are able to substantially improve both power consumption and quality of service (QoS), when compared to an unmanaged base station. Motivation and rationales are given in Section 5.1; the design of the base station is described in Section 5.2, while the corresponding models used for simulation purposes are detailed in Section 5.3. The load focussed approach and load/energy balanced approach are presented in Sections 5.4 and 5.5 respectively. The dynamic programming algorithm is detailed in Section 5.6 and simulation results are described in Sections 5.7 and 5.8.

5.1 Motivation and Rationale

Typical broadband access solutions use an optical fibre network that is then locally distributed to users through the copper twisted-pairs legacy phone network. However, the deployment of optical fibres is a very expensive process, which makes this technology unprofitable for service providers in low density areas.

The suitability of wireless technologies for rural broadband has been studied in

developing [15–18] and developed countries [14, 19, 20], both from a technical and economical standpoint. Several wireless technologies were proposed in the context of rural broadband access, including Wireless Fidelity (WiFi) and TV white space (TVWS) approaches. The remoteness of a base station used for rural broadband might require the introduction of energy harvesters to supply power [24–26]. The introduction of renewable energy harvesting strongly affects the available power, two approaches are then possible to maintain service, either the energy system need to be overdimensioned to guarantee a minimum service [19], requiring large and expensive energy systems, or resource management has to be introduced [27].

The rural broadband scenario is particularly well suited for the introduction of resource management schemes. The spacial distribution of users in rural environments, in the form of clusters—villages—surrounded by sporadically placed users renders the rural area well suited for the use of multiple RATs with different propagation characteristics, allowing to serve both the close-by and farther away users, while optimising the user data rate [28]. Several studies showed that energy savings and QoS improvements are achievable by optimising the user assignment in a heterogeneous network scenarios [31, 32].

In this chapter, we aim to determine the optimum reach, i.e. the farthest distance to which service can be provided, of the WiFi network of the rural broadband multi-radios base station presented in Section 5.2; said reach can be adjusted by changing the transmit power of the WiFi radio. This work aims to determine the optimum reach policy $r_{\text{opt}}(t) \in A$ of the WiFi radio at a given time t to both improve on QoS and base station power consumption, over the operation time of the base station. The function $r_{\text{opt}}(t)$ is the function that maps an instant t in time to the optimum WiFi reach distance; all possible functions $r(t)$ are contained within a space $A \subset B(\mathbb{R})$, with $B(\mathbb{R})$ the space of continuous bounded functions of \mathbb{R} .

$$\begin{aligned} r : \mathbb{R}^+ &\rightarrow [0; r_{\text{GHz,max}}[\\ t &\mapsto r(t) \end{aligned}, \tag{5.1}$$

with $r_{\text{GHz,max}}$ the maximum distance reachable by the WiFi radio.

The optimisation take into account user activity and energy harvesting forecast as well as base station power consumption and battery level and other parameters such as constraints on minimum battery level and maximum load of the TVWS network. The optimisation is perform for each time step, i.e. every 30 minutes, using a dynamic

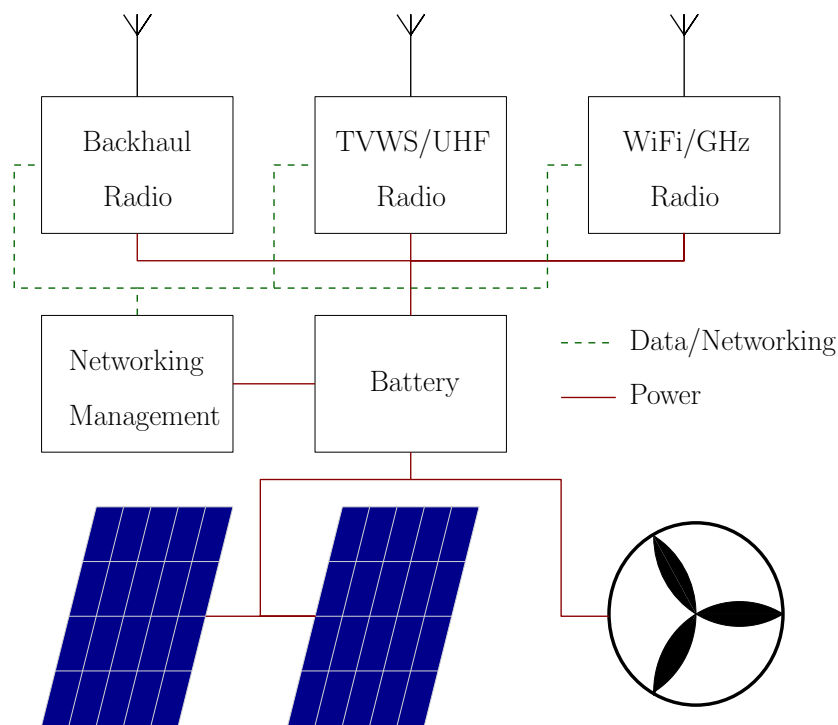


Figure 5.1: Multi-radio off-grid base station, system block diagram.

programming algorithm operating in a 24-hour sliding window.

5.2 Base Station Design

The base station considered in this thesis is based on the design proposed in [19]. It is equipped with three radio: one for point to point (PTP) backhaul, and two radios that distribute services locally, as presented in Figure 5.1, while solar panels, a wind turbine and batteries provide power to the base station.

5.2.1 Radio Systems

The base station is equipped with three different radio systems; a PTP high throughput wireless link provides the backhaul connection to the internet, while the service is redistributed locally using two point to multi-points (PTMP) radios operating in different parts of the electromagnetic spectrum. For rural communities spread on large areas, the use of a TVWS ultra high frequency (UHF) radio system with long range capabilities is considered, due to the better propagation characteristics in the lower frequencies of the UHF band [29], allowing to cover larger areas with a single base station.

The capacity of such TVWS radio is however limited by the overcrowding of the TV spectrum [30], thus reducing the reachable throughput for broadband application. In order to provide satisfactory QoS to rural communities a previously proposed solution [19] is to combine the TVWS radio access network (RAN) with a higher throughput but shorter range WiFi RAN in the 2.4 GHz band. This design is also well suited for rural applications as it takes advantage of the typical distribution of users into villages surrounded by sparingly located properties, as shown in Figures 5.2 and 5.4 and described further in Section 5.3.2.

To allow the optimisation of the user assignment to either of the two PTMP networks, all users within the WiFi covered area are provided with radio hardware that can be automatically configured to operate either in the UHF or the GHz band. Connection requests and assignment messages are carried by the TVWS network, which is used by default by the radio hardware of the end users upon startup.

5.2.2 Power Supply and Storage

In this work, a benchmark energy harvesting system is established for use as a reference in the measurement of the performances of the implemented algorithms. This system implementing an over-dimensioned harvester system was tested in simulation and shown capable of maintaining service at all time, with variations of this system tested by previous studies [19, 20, 105, 106]. This work explores further changes in the power supply by experimenting with different ratios of available energy from two types of harvesters. The initial base station is equipped with a single wind turbine (SuperWind SW350) [28] with a peak output power of 350 W and two photovoltaic solar panels producing up to 250 W each. The use of such an hybrid power system was shown suitable for operation in Scotland (UK) [19] where both resources change prevalence alternatively during the year, with solar energy the source of choice during the summer months, while wind power production peaks during the winter. To maintain service at all times, the base station is also equipped with a battery bank of 7.2kWh.

5.2.3 Control System

The base station is equipped with a control and management system which can be used to run one of the proposed optimisation algorithms based of the formulations in Sections 5.4 and 5.5, in order to adjust the transmission power of the WiFi radio, thus changing the assignment of users between the two radios. The control systems also gathers weather forecast data which is used to estimate the amount of energy to be

harvested by the solar panels and wind turbines in the near future, information which is then fed to optimisation algorithms.

5.3 Models

This section presents the various models employed for the formulation of the cost and transition penalty functions used for the dynamic programming algorithm.

5.3.1 Time Keeping

In this chapter, time is sampled in 30 minutes intervals δ_t . It is not realistic to perform the optimisation over extended periods of time, as in a real system some of the data required for an erudite decision, such as forecasts for the amount of harvested energy or user activity predictions are not reliably available over extended period of time, thus justifying a local instead of a global optimisation. Two main time scales are used, with t being the absolute time within a simulation run, while τ is used to index time locally within a 24-hour optimisation window centred on an absolute time step t , such as an optimisation window can be defined with $\tau \in \{t - K\delta_t, \dots, t, \dots, t + K\delta_t\}$, with $K \in \mathbb{N}$ the number of time steps δ_t in 12 hours.

As renewable energy harvesting varies at various scales within a year and from year to year, the absolute time t is divided in months number m , day number $d \in [0; D(m)[$ within a month, where $D(m)$ is the function that gives the number of days within a given a month $m \in \mathbb{N}$, and $h \in [0; 24 - \delta_t]$ the time within a day in hour. Throughout this chapter the absolute time starts on the 1st of January at 00:01, such that t can be written as

$$t = m \times \left(\sum_{n=0}^{m-1} D(n) \right) + d \times 24 + h. \quad (5.2)$$

5.3.2 Network Model

In this work, a single base station serving a unique community is assumed. A community is composed of a single village surrounded by sparingly located users, wireless broadband is provided by a single base station using conjointly a TVWS UHF and a WiFi GHz radio, as shown in Figures 5.2 and 5.4. Any given community can be described using three main characteristics, in the form of community size, distribution of users and load modelling. Communities are constant over time, i.e. the numbers and positions of users are set at the start of a simulation.

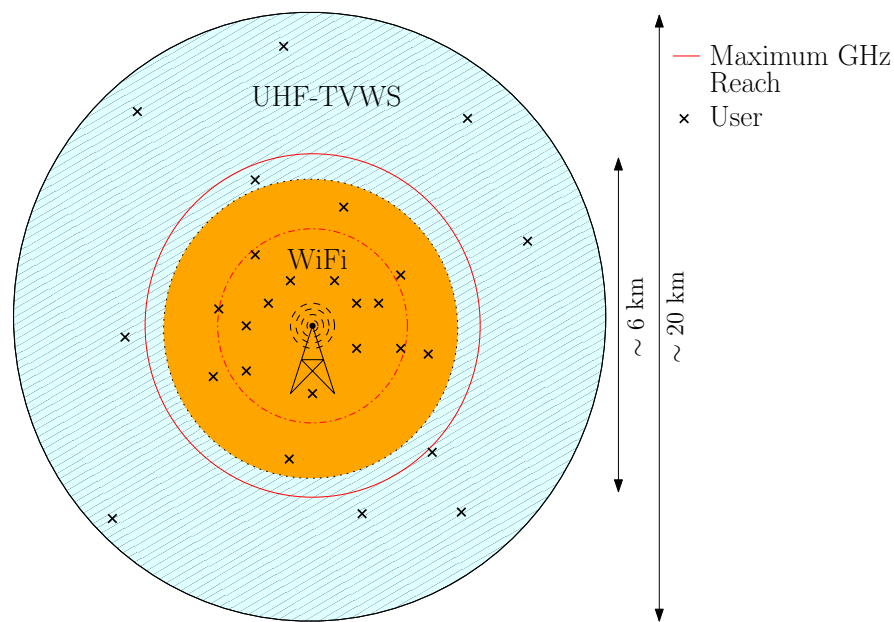


Figure 5.2: Multi-network access scenario, a community is served by a single base station located at the centre of the village.

Community Size

The size N of a community is assumed to vary between 20 and 50 users. This choice is mainly guided by the fact that the application for such a base station with a single radio backhaul link would not be able to provide a high quality of service to a larger community. Furthermore, a larger community would require more PTMP radios, and/or multiple base stations to provide a satisfactory service, in a network configuration similar to that discussed in [19] and [3].

User Spatial Distribution

Rural environments are usually composed of clusters of houses (i.e. villages), while other houses are spread sparsely around the villages, sometime kilometres away from each other. Two types of scenarios are investigated in this work. In a first setting, the base station is located within the village as shown in Figure 5.2 and equipped with omnidirectional antennas. The second scenario implements a base station located at the edge of the village, such that the PTMP radios use sector antennas that covers the full extend of the village, as well as the users located in the countryside behind the village with respect to the base station, as shown in Figure 5.4. In both scenarios, the channels characteristics are assumed the same in all directions covered by the base station, which allows to simplify the models for the channel and spatial distribution of

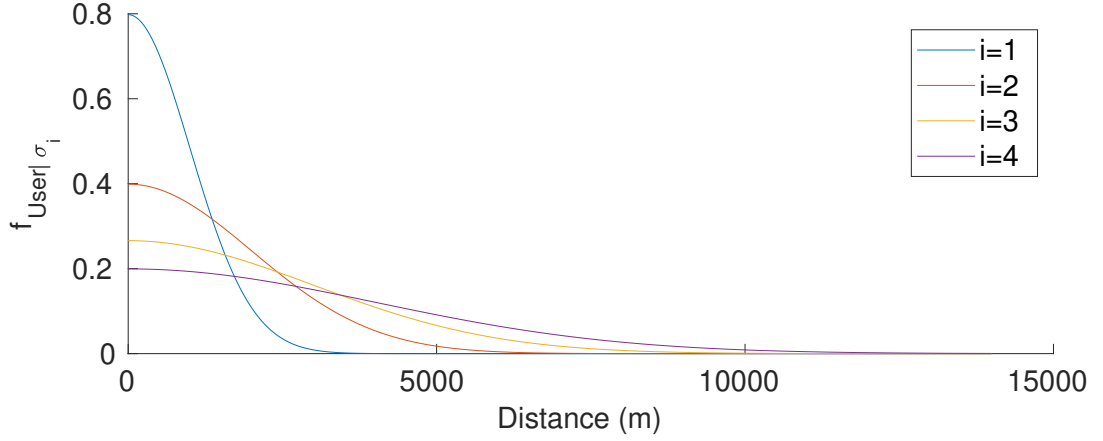


Figure 5.3: Half-normal spatial distributions of users, with respect to their distance from the base station.

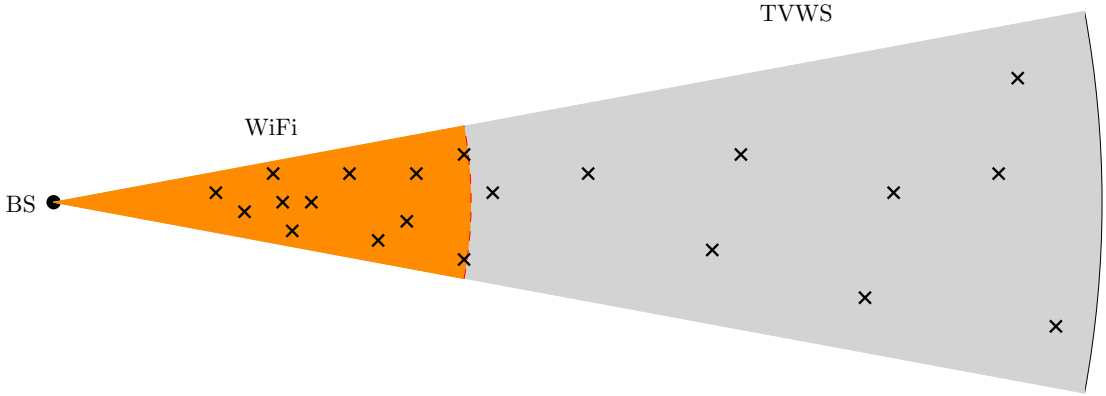


Figure 5.4: Multi-radio base station located on the side of the community.

user, as the position of all users can be expressed via their distance r from the base station.

To generate the positions of the users, two probability distributions associated with their respective scenarios are introduced. In the first scenario, in which the base station is in a central position, the user distribution is modelled using half normal distributions. The probability density functions $f_{\text{Users}|\sigma_i}$, presented in Figure 5.3, can be expressed as

$$f_{\text{Users}|\sigma_i}(r) = \begin{cases} \frac{\sqrt{2}}{\sigma_i\sqrt{\pi}} e^{\left(-\frac{r^2}{2\sigma_i^2}\right)} & r \geq 0, \\ 0 & \text{otherwise,} \end{cases} \quad (5.3)$$

with σ_i the standard deviations, detailed in Table 5.1a.

The second scenario, where the base station is situated on the edge of the village,

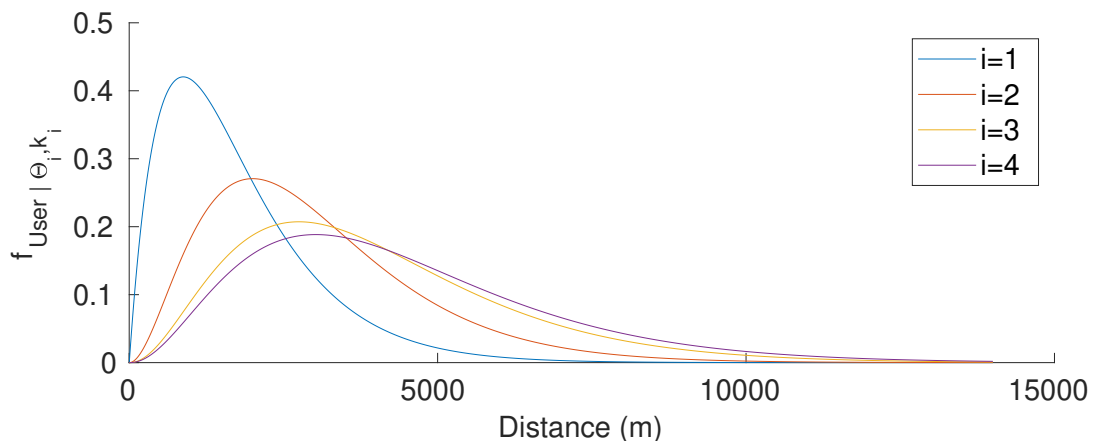


Figure 5.5: Gamma spatial distributions of users, with respect to their distance from the base station.

Table 5.1: User spatial distributions parameters.

Distribution	Standard deviation σ_i	Distribution	Shape k_i	Scale Θ_i
$f_{\text{User} \sigma_1}$	1	$f_{\text{User} \Theta_1, k_1}$	3.2	2.25
$f_{\text{User} \sigma_2}$	2	$f_{\text{User} \Theta_2, k_2}$	3.2	2.50
$f_{\text{User} \sigma_3}$	3	$f_{\text{User} \Theta_3, k_3}$	3.5	2.75
$f_{\text{User} \sigma_4}$	4	$f_{\text{User} \Theta_4, k_4}$	3.5	3.25

(a) Half-normal

(b) Gamma

employs Gamma distributions, shown in Figure 5.5 with a higher concentration of user within a given reach from the base station, determined by the parameters k_i and Θ_i , as shown in Table 5.1b, such that each distribution $f_{\text{Users}|\Theta_i, k_i}$ can be written as

$$f_{\text{Users}|\Theta_i, k_i}(r) = \frac{1}{\Gamma(k)\Theta_i^{k_i}} r^{k_i-1} e^{-\frac{r}{\Theta_i}}, \quad (5.4)$$

where k_i and Θ_i are the shape and scale parameters for the i^{th} distributions respectively, while the Gamma function is defined as $\Gamma(\alpha) = (1 - \alpha)!$.

Load Model

As in most communication networks the number of active users and thus the load on the base station varies throughout the day. A typical approach would be to use a Maier model [107] to represent the evolution of the traffic over time. However, previously a study [19] of the ADSL traffic on the Isle of Tiree (United Kingdom (UK)) has shown that the load varied following the model presented in Figure 5.6.

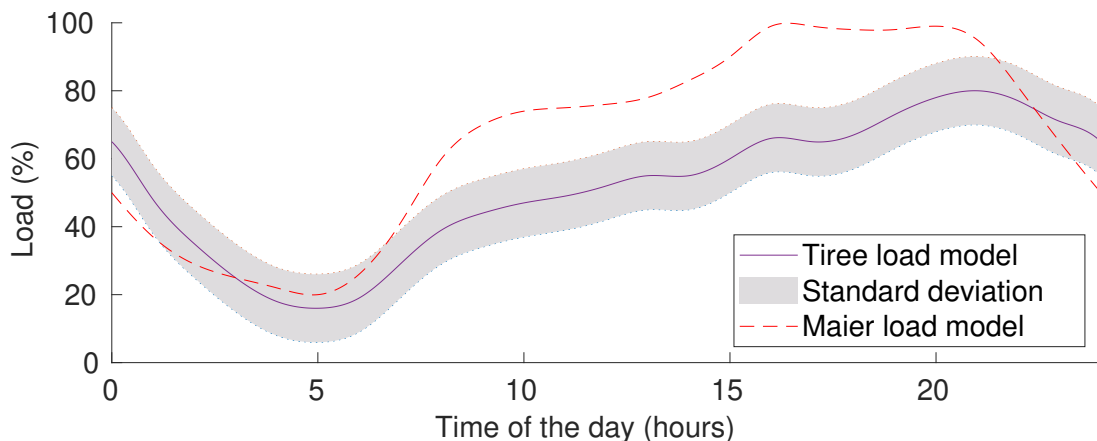


Figure 5.6: Mean load variation throughout the day, Tiree [19] and Maier [107] models.

The number of active user at a time step t , $N_a(t)$, is randomly selected following a normal distribution with a 10% standard deviation from the mean shown in Figure 5.6. In this work, it is assumed that at least one user is active at all times. This assumption, while in theory not perfect, represents a good approximation of a practical case in which the TVWS radio would be kept active in order to maintain service, as in the considered scenario the TVWS network is used by default, for establishing links and managing communications.

Simulated Community and Active Users

For a simulation, a fixed community of size N is created by randomly selecting distances r_n , $n \in \{0 \dots N-1\}$ following one of the distributions presented above, leading to a set of users ordered by increasing distance from the base station $R = \{r_0, \dots, r_n, \dots, r_{N-1}\}$. Given a simulated community of size N , with fixed (for the duration of the simulation) user distribution $R = \{r_0, \dots, r_n, \dots, r_{N-1}\}$ and a randomly selected number of active users $N_a(t)$, $N_a(t)$ users are uniformly picked from the set R , thus forming a subset $R_a(t)$ listing the positions, i.e. distances r_n , $n \in \{0, \dots, N-1\}$ of all active users from the base station.

5.3.3 Power Consumption Model

The power consumption of the base station P_{BS} can be divided into four main components corresponding to the different subsystems presented in Figure 5.1,

$$P_{BS}(t) = P_{UHF} + P_{Backhaul} + P_{System} + P_{GHz}(t), \quad (5.5)$$

where P_{UHF} , P_{Backhaul} and P_{System} are constants representing respectively the power consumption of the UHF PTMP radio, the backhaul link radio and the base station management computer respectively. The power consumptions P_{Backhaul} and P_{System} are estimated at 45 W and 9 W respectively, based on an existing low-power base station design [105, 106], while the power consumption of the PTMP radios are estimated using the model previously used in [21, 28] and detailed below. The value of P_{UHF} is determined by the transmit power required for the UHF radio to reach the farthest user in the network, and is thus constant for a given community. The GHz radio power consumption $P_{\text{GHz}}(t)$ however depends on the current user assignment and thus the most distant user that is assigned to the GHz radio.

PTMP Radio Power Consumption

The power consumption $P_a(r)$ (in Watts) of a radio system $a \in \{\text{GHz}, \text{UHF}\}$ is set to reach a distance r from the base station, where GHz and UHF refer to the GHz and UHF radio access networks, respectively, can be expressed as follows:

$$P_a(r) = \alpha_a (P_a^{tx}(r) - G_a^{tx})^{\beta_a} + \gamma_a. \quad (5.6)$$

The parameters $\alpha_a, \beta_a, \gamma_a$ are coefficients characterising the UHF/GHz radio power consumption model determined empirically by fitting (5.6) to power consumption data from the radio in [19, 21, 28]. The parameter G_a^{tx} is the transmitting antenna gain and $P_a^{tx}(r)$ is the minimum transmission power in dB required to reach a user at a distance r of the base station

$$P_a^{tx}(r) = L_a(d) + P_a^{rx} - G_a^{rx}, \quad (5.7)$$

where G_a^{rx} is the receiving antenna gain, P_a^{rx} the minimum required receiving power. The value $r = r_{\text{max}}$ is set for the UHF network ($a = \text{UHF}$), where r_{max} is the distance to the farthest user from the base station. The simplified path loss $L_a(r)$, defined by [29], is

$$L_a(r) = K_a + \eta \times 10 \log(r). \quad (5.8)$$

Values of K_a and η were determined by path loss measurement on the Isle of Tiree (UK) in [21]. Using the parameters presented in Table 5.2, the power consumption of the GHz radio can be expressed as a function of the distance d reached by the link. The transmit power for unlicensed WiFi devices is limited to 30 dBm [108], thus providing a ceiling to the maximum power consumption of the GHz radio, as shown in Figure 5.7.

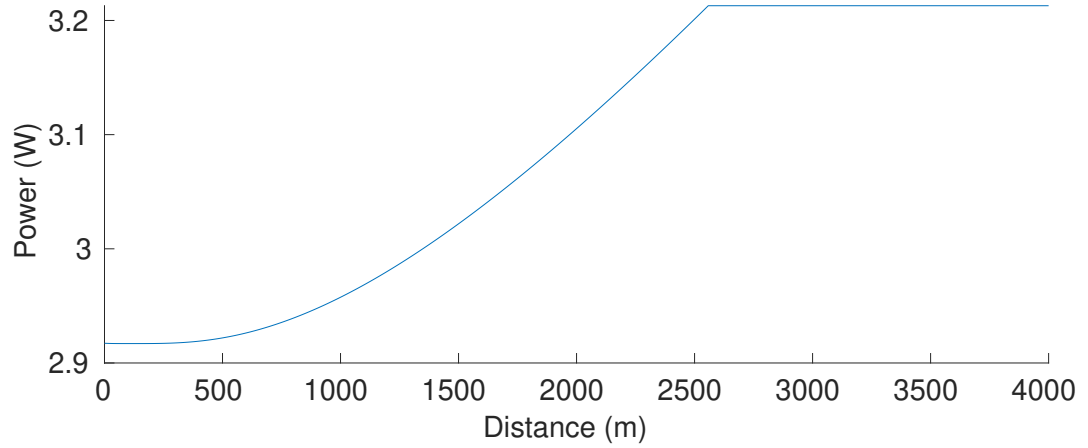


Figure 5.7: GHz radio power consumption for a given maximum reach from the base station.

Table 5.2: Power consumption model parameters extracted from [28].

Parameter	GHz	UHF
η		2.39
α_a	$1.135e^{-7}$	$3.395e^{-7}$
β_a	4.545	4.424
γ_a	2.342	2.555
K_a	-47.5dB	-28.43dB
P_a^{rx}	-90dB	-100dB
G_a^{rx}	10dB	10dB

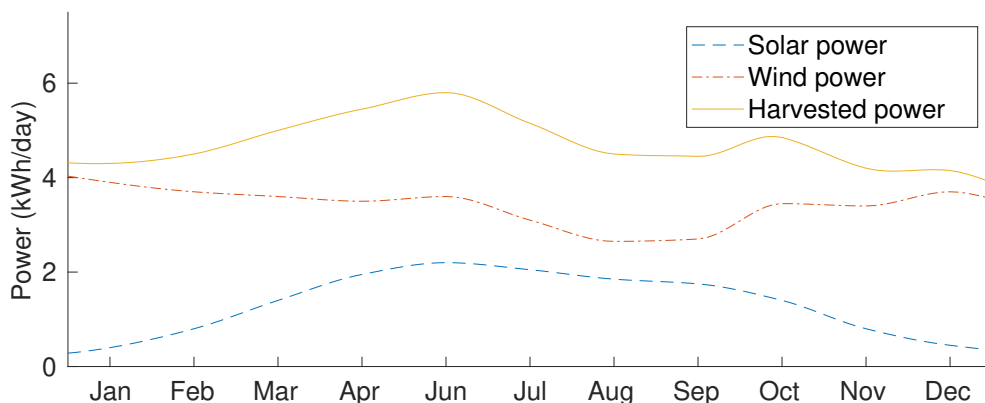


Figure 5.8: Average daily energy generation on Tiree, Scotland [19].

5.3.4 Power Generation and Storage Models

As with most renewable energy sources, the instantaneous power output of solar panels and wind turbines varies hourly, daily and monthly, thus a way to model the available power and to take into account the time distribution of each energy source is required [4, 5]. This work is based on data for energy harvested on the west coast of Scotland—Isles of Tiree and Bute—as presented in [19], the harvesting capabilities have however been increased, compared to previous designs [19, 21, 28], to fit some of the alterations to the base station design, such as an increase of the backhaul radio power consumption. The mean energy production of the two types of harvesters, listed in Section 5.2.2, is presented in Figure 5.8. These statistics show that the wind represents the main energy source all year round, it however decreases during the summer months, but the increase in solar energy during those months tends to counterbalances the lack of wind power.

Solar Power

Harvestable solar power varies greatly over time, and is particularly influenced by the weather, the time of the day and the season [4, 5]. The weather has a strong influence on the power output of solar panels, with energy figures on a rainy day dropping to 10% of the energy harvested on a sunny day [109]. For this purpose, a probability of the weather being sunny on a given month is defined as

$$P_{\text{sunny}} = \frac{(\text{hours of sunshine})}{(\text{average day length}) \times (\text{number of days})}. \quad (5.9)$$

This energy production also depends on the time of the day, especially when the solar panel is not equipped with a tracking system. Additionally, there is no energy harvested during the nights. To represent this variation, related to the angle of incidence of the

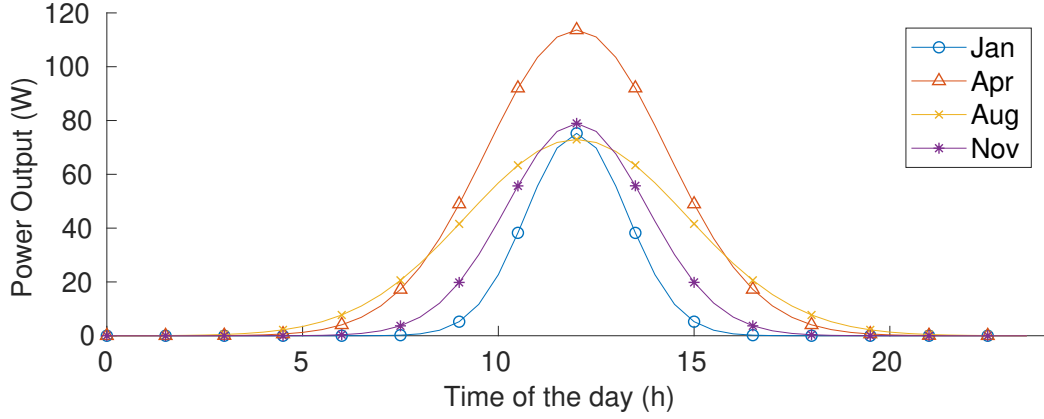


Figure 5.9: Sun power generation variation, average instant power against the time of the day.

sun, a bell shaped hourly distribution, shown in Figure 5.9, is used [110], the dimension of the distributions are tied to the length of the day, the average harvested energy for the month and the probability of a sunny day for the month. These parameters, specific to the geographical location of the solar panel, are based on measurements performed in previous work [19], as well as weather data [111].

As such, the energy output $E_S(t)$ of the solar panels at time t is determined as follow. Lets $X_S(m, d)$ be a random variable representing the amount of energy in Joules produced on a day d of month m , obeying to a normal distribution of mean $\mu_S(m, d)$ and standard deviation $\sigma_S(m, d)$. The average energy production $\mu_S(m, d)$ for a given day is extrapolated from the values shown in Figure 5.8, while the standard deviation is adjusted according to the value of P_{sunny} for a given month m . Once randomly selected, the total energy for the day $X_S(m, d)$ is then spread using the Gaussian functions of the time of the day, centred on noon, shown in Figure 5.9 and defined as

$$f_S^{(m,d)}(h) = \frac{1}{\sigma_h(m, d)} \frac{1}{2\sqrt{2\pi}} e^{-\frac{1}{2} \left(\frac{h-12}{\sigma_h(m,d)} \right)^2}, \quad (5.10)$$

where $\sigma_h(m, d)$ is set to 30 % of the daylight time of day d of month m [110], leading to the instant, i.e. within a time step δ_t , solar energy production being represented by a random variable $E_S(t)$, defined as

$$E_S(t) = f_S^{(m,d)}(h) \times X_S(m, d), \quad (5.11)$$

where h , m and d are related to t as defined in Section 5.3.1.

Wind Power

Compared to solar energy, wind power varies more slowly throughout the day [112], but can change greatly from one day to another. In our simulations, the energy output of the wind turbine for a single time step δ_t at $h = K$, i.e. at 12 p.m. (noon) of a day d of a month m is represented by a random variable $X_W(m, d)$ following a normal distribution centred on the mean wind energy production for a given month $\mu_W(m)$, with the standard deviation $\sigma_W(m) = \mu_W(m)/2$ [113]. The energy is then spread over the entirety of the day by way of linear interpolation such that,

$$E_W(t) = \frac{X_W(m, d) - X_W(m, d - 1)}{24} \times h + X_W(m, d - 1), \quad (5.12)$$

with the relation between t , m , d and h defined in Section 5.3.1.

Energy Storage

In this work, a simplified battery model is implemented, it considers both the battery self-discharge and the charge/discharge efficiency [4, 5]. For simplicity the charge/discharge efficiency is combined with the performance of the power conversion system, both consumption and production, leading to an overall efficiency η_B of 80% [114], such as

$$E_B(t) = (1 - \alpha_B)E_B(t - \delta_t) - \frac{1}{\eta_B}E_{BS}(t) + \eta_B(E_W(t) + E_S(t)). \quad (5.13)$$

$E_B(t)$ is the amount of energy stored in the battery, $E_W(t)$ the energy produced by the wind turbine, $E_S(t)$ the harvested solar energy and $E_{BS}(t)$ the base station power consumption. The parameter α_B is the self discharge coefficient corresponding to the simulation step-time, it is used to represent the energy losses within the power management system as well as the natural self-discharge of the battery.

5.4 Load Focussed Optimisation

This section introduces a load focussed approach to the user assignment optimisation problem.

5.4.1 Resources Optimisation

Considering the coverage areas presented in Figures 5.2 and 5.4 of a community comprising N users, this work aims to determine the boundary, located at a distance r of the base station, such that all users within are assigned to the GHz network, while all users outside are served using the UHF radio. The optimisation problem is formulated

with the objective to determine the optimum reach policy $r_{\text{opt}}(t)$ for the GHz network of the base station, such that the base station maintains a high level of QoS on average through the total time of operation. The measurement of the QoS at a time t is based on the use of a load factor of the UHF network, expressed as $E_{\text{Load}}(t, r(t))$ the function of the reach assignment function $r(t)$; thus to maintain an acceptable QoS we aim to run the base station such that the average load on the UHF network $\mathbb{E}\{E_{\text{Load}}(t, r(t))\}$ is as low as possible. The optimisation problem is formulated as

$$r_{\text{opt}}(t) = \underset{r(t) \in A}{\operatorname{argmin}} (\mathbb{E}\{E_{\text{Load}}(t, r(t))\}) \quad \text{s.t. } E_{\text{B}}(t, r_{\text{opt}}(t)) > E_{\text{B},\text{min}}, \quad (5.14)$$

$$\mathbb{E}\{E_{\text{Power}}(t, r_{\text{opt}}(t))\} > E_{\text{Power},\text{target}},$$

with $E_{\{\text{B},\text{Power}\}}(t, r(t))$ associated respectively with the battery energy level, the power balance of the base station. These describe how the energy harvesting and power consumption of the base station balance each others, while $E_{\text{Load}}(t, r(t))$ is linked to the load of the UHF network, with respect to a reach function $r(t)$. The function $E_{\text{Load}}(r(t))$ is defined as

$$E_{\text{Load}} : \mathbb{R}^+, A \rightarrow B(\mathbb{R})$$

$$t, r(t) \mapsto \frac{N_{\text{UHF}}(t, r(t))}{N_{\text{UHF},\text{max}}} \quad (5.15)$$

where $N_{\text{UHF}}(t, r(t))$ is the function that maps a given reach function of the time and the random variable $N_a(t)$, i.e. number of active users at a given time t as defined in Section 5.3.2, to a the number of users assigned to the UHF network; while $N_{\text{UHF},\text{max}}$ is the maximum number of users on such network for optimal operation, this value is based on the throughput achieved by TVWS networks in previous studies [19, 28].

The minimisation of E_{Load} is performed under a constraint on the minimum energy $E_{\text{B},\text{min}}$ to be left in the battery at any time. The constraint $\mathbb{E}\{E_{\text{Power}}(r_{\text{opt}}(t))\} > E_{\text{Power},\text{target}}$, with $\mathbb{E}\{\cdot\}$ the expectation operator over time, represents the idea that the overall energy balance of the base station needs to be within an acceptable range on average, i.e. in this formulation of the problem that the energy consumed by the GHz radio only represents an acceptable portion $E_{\text{Power},\text{target}}$ of the energy harvested. The quantity $E_{\text{Power}}(r_{\text{opt}}(t))$ is defined as

$$E_{\text{Power}}(t, r(t)) = \frac{E_{\text{S}}(t) + E_{\text{W}}(t)}{E_{\text{GHz}}(t, r(t))}, \quad (5.16)$$

where $E_{\text{S}}(t)$, $E_{\text{W}}(t)$ and $E_{\text{GHz}}(t, r(t))$ are the harvested solar, wind energy and the

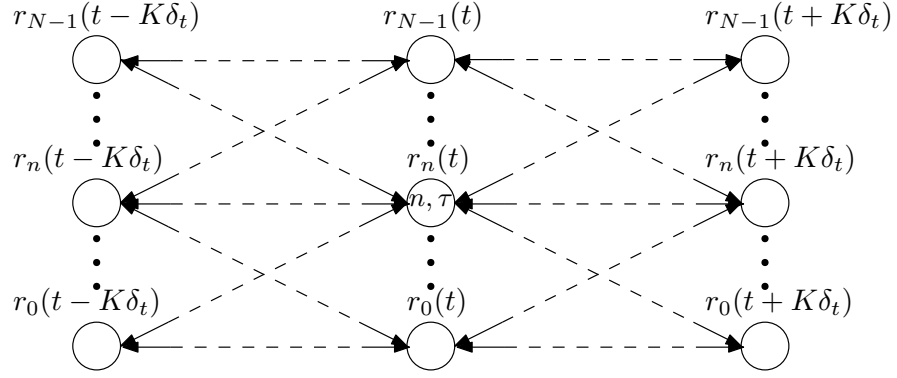


Figure 5.10: Set of the achievable states by the base station depending on the selected reach r .

energy consumption of the WiFi radio at time t and with a reach set at $r(t)$.

5.4.2 Reformulation for Dynamic Programming

It is not practical to solve the ill-posed problem expressed in (5.14) globally, furthermore some of the data required for an erudite decision, such as forecasts for the amount of harvested energy or user activity predictions are not reliably available over extended period of time, thus justifying a local instead of a global optimisation. Additionally, the dynamic programming solving technique, applied in this work, requires a finite number of reachable states within the Markov chain modelling the problem, shown in Figure 5.10. To this end, this work proposes to solve the optimisation problem (5.14) using a 24-hour sliding window indexed on a time variable τ and centred on the current time t , thus solving a succession of localised problems in time. This allows to benefit from the higher reliability of short-term weather forecasts, in turn increasing the accuracy of the energy harvesting predictions. The 24-hour window is then indexed using a discrete time variable τ , such as $\tau \in \{t - K\delta_t, \dots, t, \dots, t + K\delta_t\}$, with $K \in \mathbb{N}^+$ the number of time steps δ_t in 12 hours; this work selected a time step $\delta_t = 30$ minutes, consequently leading to $K = 24$ and the a total window length of $2K = 48$. To further reduce the search space, this work considers that the community has a given number of users N , as defined in Section 5.3.2, and that the positions of the users are constant over time; this enables to use a subset $\{r_0, \dots, r_n, \dots, r_{N-1}\}$ of the set of images $[0; r_{\max}[$ of reachable points by the GHz network, where r_n is the distance of the n^{th} users, when the set of users is sorted by increasing distance from the base station. The function

$r(t)$, defined in (5.1), can be reformulated as

$$r : \{t - K\delta_t, \dots, t, \dots, t + K\delta_t\} \rightarrow \{r_0, \dots, r_n, \dots, r_{N-1}\} \quad (5.17)$$

$$\tau \mapsto r(\tau)$$

The length of the window and the time discretisation step δ_t were heuristically found by way of simulation. As determining the optimum policy vector

$$\mathbf{r}_{\text{opt}}(t) = [r_{\text{opt}}(t - K\delta_t), \dots, r_{\text{opt}}(\tau), \dots, r_{\text{opt}}(t + K\delta_t)] \quad (5.18)$$

with the coefficients $r_{\text{opt}}(\tau) \in \{r_0, \dots, r_n, \dots, r_{N-1}\}$ is equivalent to determining a vector $\mathbf{n}_{\text{opt}}(t) = [n_{\text{opt}}(t - K\delta_t), \dots, n_{\text{opt}}(\tau), \dots, n_{\text{opt}}(t + K\delta_t)]$ with coefficients $n_{\text{opt}}(\tau) \in \{0, \dots, N - 1\}$, the problem (5.14) can be rewritten as:

$$\mathbf{n}_{\text{opt}}(t) = \underset{\mathbf{n}(t)}{\operatorname{argmin}} \sum_{\tau=t-K\delta_t}^{t+K\delta_t} E_{\text{Load}}(n(\tau)) \quad \text{s.t.} \quad E_{\text{B}}(\mathbf{n}_{\text{opt}}(t)) > E_{\text{B},\text{min}} , \quad (5.19)$$

$$E\{E_{\text{Power}}(\mathbf{n}_{\text{opt}}(t))\} > E_{\text{Power},\text{target}} ,$$

where $E_{\text{Load}}(n)$, $E_{\text{B}}(n)$, and $E_{\text{Power}}(n)$ are the re-indexed version (from $r(t)$ to $n(t)$) of the functions presented in Section 5.5.1, and $E\{\cdot\}$ the expectation over τ . The reformulation from a global to a local problem allows to represent it as a finite state discrete time Markov space, such as the states relate to the TVWS network load, while the transitions are tied to the base station energy balance, turning (5.19) into a shortest path problem, which in turn can be solved using the dynamic programming algorithm, introduced in Section 5.6. This reduction of the search space and reformulation into a dynamic programming approach provides us with a finite number of states for which the associated costs can be listed in a matrix $C(t)$ at each global time step t .

5.4.3 Cost Function

The cost function is based on $E_{\text{Load}}(t)$, the finite number of reachable states by the system, within the localised problem expressed in (5.19). This allows to list all reachable states within a single 2D space $C(t)$ for the time step t of which the first dimension is indexed on τ and the second in n the user number. The cost space $C(t)$ represents the ratio between the numbers of users potentially assigned to each network, for $\tau \in \{t - K\delta_t, \dots, t + K\delta_t\}$ and $n \in \{0, \dots, N - 1\}$ the coefficients $c_{\tau,n}(t)$ are computed as

follows,

$$c_{\tau,n}(t) = \begin{cases} \frac{N_a(\tau)-n}{N_{\text{UHF,max}}} & n \in \{0, \dots, N_a(\tau)\}, \tau \in \{t, \dots, t + K\delta_t\} \\ \Phi_{\tau}(n) & \tau \in \{t - K\delta_t, \dots, t - \delta_t\} \\ 0 & \text{otherwise} \end{cases}, \quad (5.20)$$

with $N_a(\tau)$ the number of active users and $\Phi_n(\tau)$ defined as,

$$\Phi_{\tau}(n) = \begin{cases} 0 & n = n_{\text{opt}}(\tau) \\ 1 & \text{otherwise} \end{cases}. \quad (5.21)$$

This cost space represents a local estimate of all values attainable by the load balance cost function E_{Load} defined in (5.15), for the local optimisation problem. The function $\Phi_{\tau}(n)$ provides memory of previous decisions of the algorithm, by creating a canyon in the cost function, this constraints the algorithm to converge toward the same solutions in the states associated with past time steps. While the main part of the cost function $\frac{N_a(\tau)-n}{N_{\text{UHF,max}}}$ provides an increase cost with the number of users assigned to the TVWS network.

5.4.4 Transition Penalty Function

Two transition penalty matrices are defined for the cost aggregation step, described in Section 5.6.2, in this dynamic programming approach, such that the transition penalty reflects the constraints in problem (5.19). The spaces $P^{\text{up}}(t)$ and $P^{\text{down}}(t)$ are associated with an increase or decrease of the GHz reach respectively, such that the coefficients $p_{\tau,n}^{\{\text{up},\text{down}\}}(t)$ are defined as

$$p_{\tau,n}^{\{\text{up}\}}(t) = h_{\tau,n}(t), \quad (5.22)$$

$$p_{\tau,n}^{\{\text{down}\}}(t) = 2 - h_{\tau,n}(t). \quad (5.23)$$

The coefficients $h_{\tau,n}(t)$ of $H(t)$ represent the instantaneous energy balance of the base station for each states of the cost space, such as

$$h_{\tau,n}(t) = \frac{E_S(\tau) + E_W(\tau)}{E_{\text{GHz}}(r_n)} \times \frac{C_B}{E_B(\tau) - E_{B,\text{min}}}, \quad (5.24)$$

where $E_{B,\text{min}}$ is the targeted amount of energy the algorithm aims to keep in the battery at all times. The first part of the product in (5.24) is linked to the power balance related constraint on E_{Power} , while the second is linked to the constraint on battery level. The main objective of this formulation is to produce a transition penalty that increases with

an increase of reach between time steps, thus discouraging increase in reach between steps when the battery level is low.

5.5 Energy/Load Balanced Optimisation

This section introduces an approach based on a energy/load balanced cost function to the user assignment on the base station.

5.5.1 Optimisation Problem

Similarly to the one explored in Section 5.4.1, this approach aims to extract an optimum GHz radio reach breathing policy $r_{\text{opt}}(t)$ for the current time step t . However in this approach the problem takes into account the current energy balance of the base station and load on the TVWS network, considering both past and the forecasted values. The problem to determine the optimum policy $r_{\text{opt}}(t)$ is then defined as

$$r_{\text{opt}}(t) = \underset{r(t) \in A}{\operatorname{argmin}} (\mathbb{E}\{E(t, r(t))\}) \quad \text{s.t.} \quad E_{\text{B}}(t, r_{\text{opt}}(t)) > E_{\text{B},\text{min}}, \quad (5.25)$$

$$\mathbb{E}\{E_{\text{Power}}(t, r_{\text{opt}}(t))\} > E_{\text{Power},\text{target}},$$

where $E_{\text{B}}(r_{\text{opt}}(t))$ is the energy left in the battery after $r_{\text{opt}}(t)$ is selected. This battery level $E_{\text{B}}(r(t))$ is constrained to always be superior to a minimum value $E_{\text{B},\text{min}}$, which allows to power the base station for a predetermine time without any input from the harvesters.

Different to what is presented in Section 5.4, in this approach the information related to the power balance of the base station, i.e. $E_{\text{Power}}(r(t))$, is incorporated into the optimisation problem by use of the objective function $E(r(t))$, instead of the constraints introduced in (5.14). The objective function $E(r(t))$ is then related both to the energy generation, consumption at the base station site, by way of $E_{\text{Power}}(r(t))$ and QoS information through the energy function $E_{\text{Load}}(r(t))$. $E(r(t))$ is then defined as

$$E(r(t)) = E_{\text{Power}}(r(t)) + \mu_{\text{Load}} \times E_{\text{Load}}(r(t)), \quad (5.26)$$

where the energy functions E_{Power} and E_{Load} are balanced using a coefficient μ_{Load} , determined empirically.

5.5.2 Reformulation for Dynamic Programming

As detailed in Section 5.4.2 for the load based approach presented in Section 5.4, it is unrealistic to try to solve globally the continuous version of the problem (5.25) and thus a discrete version of the problem is introduced, such as

$$\mathbf{n}_{\text{opt}}(t) = \underset{\mathbf{n}(t)}{\operatorname{argmin}} \sum_{\tau=t-K\delta_t}^{t+K\delta_t} E(n(\tau)) \quad \text{s.t.} \quad E_{\text{B}}(\mathbf{n}_{\text{opt}}(t)) > E_{\text{b},\text{min}} , \quad (5.27)$$

$$E\{E_{\text{Power}}(\mathbf{n}_{\text{opt}}(t))\} > E_{\text{Power},\text{target}} ,$$

with

$$E(\mathbf{n}(t)) = E_{\text{Power}}(\mathbf{n}(t)) + \mu_{\text{load}} \times E_{\text{Load}}(\mathbf{n}(t)). \quad (5.28)$$

5.5.3 Cost Function

Based on the optimisation problem introduced in (5.27), the cost space $C(t)$ can be built as follows,

$$C(t) = C^{\text{power}}(t) + \mu_{\text{load}} \cdot C^{\text{load}}(t). \quad (5.29)$$

As the objective function in (5.28), it is a linear combination of a cost $C^{\text{power}}(t)$ associated with the power consumption of the GHz network and the TVWS network load $C^{\text{load}}(t)$, with a balance control factor μ_{load} . This factor μ_{load} provides a finer control over the influence of the load and power balance over the cost function, its value is determined empirically by way of simulation. The coefficients $c_{\tau,n}^{\text{power}}(t)$ and $c_{\tau,n}^{\text{load}}(t)$, indexed on τ and n of the cost spaces $C^{\text{power}}(t)$ and $C^{\text{load}}(t)$ respectively are described below. The power consumption related cost coefficients are expressed as

$$c_{\tau,n}^{\text{power}}(t) = \frac{E_{\text{GHz}}(\tau, n) + E_{\text{UHF}} + E_{\text{misc}} + E_{\text{backhaul}}}{E_{\text{GHz},\text{max}} + E_{\text{UHF}} + E_{\text{misc}} + E_{\text{backhaul}}}, \quad (5.30)$$

i.e. as the ratio between the base station energy consumption associated with $E_{\text{GHz}}(\tau, n)$ and the maximum power consumption of the base station, linked to the maximum GHz radio energy consumption $E_{\text{GHz},\text{max}}$. Within the cost function C^{power} , the energy used by the GHz network is balanced with respect to the energy requirements for the rest of the base station, more specifically are included the energy consumption of the TVWS radio hardware E_{UHF} , as well as the energy consumption E_{backhaul} of the backhaul link radio, and the consumption E_{misc} of other subsystem in the base station are added. While the cost $c_{\tau,n}^{\text{power}}(t)$ increases with the coverage of the GHz network, the $c_{\tau,n}^{\text{load}}(t)$ decreases with it. The load related cost coefficients $c_{\tau,n}^{\text{load}}(t)$ can be formulated

as

$$c_{\tau,n}^{\text{load}}(t) = \begin{cases} \left| \frac{N_a(\tau) - n}{N_a(\tau) - N} \right| & \text{when } N_a(\tau) < N \\ \Gamma_{\text{load}} & \text{when } N_a(\tau) = N \end{cases}, \quad (5.31)$$

where $N_a(\tau)$ is the number of active number in the community at time τ . To prevent an infinite cost a high value Γ_{load} is used when the number of active users $N_a(\tau)$ is equal to the total number of users N . The value Γ_{load} is always set to be greater than any other $c_{\tau,n}^{\text{load}}(t)$.

5.5.4 Transition Penalty Function

Two transition penalty matrices are defined for the cost aggregation step, described in Section 5.6.2, for this dynamic programming approach. The spaces $P^{\text{up}}(t)$ and $P^{\text{down}}(t)$ are associated with an increase or decrease respectively, of the GHz reach, such as

$$p_{\tau,n}^{\{\text{up},\text{down}\}}(t) = \mu^{\{\text{up},\text{down}\}}(t) \cdot g_{\tau,n}(t) \quad (5.32)$$

where $g_{\tau,n}(t)$ is a coefficient of the penalty space $G(t)$ such as

$$g_{\tau,n}(t) = \frac{E_W(t + \tau) + E_S(t + \tau)}{\max_t (E_W(t) + E_S(t))}, \quad (5.33)$$

where $E_W(\cdot)$ and $E_S(\cdot)$ are the energy produced by the wind turbine and the solar panels, respectively. To keep the penalty values of similar order of magnitude to the cost $C(t)$, $G(t)$ is normalised using the maximum energy ever produced by the base station harvesters. The parameter $\mu^{\{\text{up},\text{down}\}}(t)$, constant over the considered 24-hour window is determined by using battery level information from the previous time step $t - \delta_t$:

$$\mu^{\text{up}}(t) = \max \left(\frac{E_B(t - \delta_t) - E_{B,\text{min}}}{C_B}, 0 \right), \quad (5.34)$$

$$\mu^{\text{down}}(t) = 1 - \mu^{\text{up}}(t), \quad (5.35)$$

with C_B the battery energy capacity expressed in Joules and $E_B(t - \delta_t)$ the energy available in the battery at the current time step t on which the considered window is centred.

5.6 Dynamic Programming

The algorithm to solve the optimisation problem is similar for both the load focused and energy/load balanced problems, formulated in Sections 5.4 and 5.5 respectively. Dynamic programming approaches are often used to solve shorter path type problem, offering reliably accurate approximation of a global minimum.

5.6.1 Algorithm

For each given time t , the following steps are applied [115]: firstly a cost space $C(t)$ of size $N \times 24\text{h}$, with N the number of users in the community, is build as presented in Section 5.4.3 and Section 5.5.3. The cost is then aggregated both in positive and negative time direction within the cost space $C(t)$ to produce an aggregated cost space $\hat{C}(t)$, as detailed in Section 5.6.2. Using two directions of aggregation allows a smoother aggregated cost $\hat{C}(t)$ and an easier optimum selection. Lastly the aggregated cost $\hat{C}(t)$ is used to determine the optimum reach $r_{\text{opt}}(t)$, as described in Section 5.6.3, and the battery level is updated for the next time step t , using equation (5.13).

5.6.2 Cost Aggregation

The cost aggregation is a well-known part of dynamic programming algorithms [115]. For this work purpose, two directions of aggregation are introduced, within the cost space, both in positive and negative time steps, i.e. on path coming from the past $\hat{C}^{(-)}(t)$ or the future $\hat{C}^{(+)}(t)$ respectively. The coefficients $\hat{c}_{\tau,n}^{(-)}(t)$ and $\hat{c}_{\tau,n}^{(+)}(t)$ for these aggregated cost spaces are computed as follow,

$$\hat{c}_{\tau,n}^{(-)}(t) = c_{\tau,n}(t) + \min \left(\min_{i \leq n} (p_{\tau,n}^{\text{up}}(t) + \hat{c}_{\tau-\delta_t,i}^{(-)}(t)), \min_{i \geq n} (p_{\tau,n}^{\text{down}}(t) + \hat{c}_{\tau-\delta_t,i}^{(-)}(t)) \right), \quad (5.36)$$

$$\hat{c}_{\tau,n}^{(+)}(t) = c_{\tau,n}(t) + \min \left(\min_{i \leq n} (p_{\tau,n}^{\text{up}}(t) + \hat{c}_{\tau+\delta_t,i}^{(+)}(t)), \min_{i \geq n} (p_{\tau,n}^{\text{down}}(t) + \hat{c}_{\tau+\delta_t,i}^{(+)}(t)) \right), \quad (5.37)$$

where $p_{\tau,n}^{\{\text{up},\text{down}\}}(t)$ are the coefficients of the transition penalty matrices $P^{\{\text{up},\text{down}\}}(t)$, defined as in Sections 5.4.4 and 5.5.4 for the load focussed and balanced approach respectively. The positively and negatively aggregated cost space, $\hat{C}^{(+)}(t)$ and $\hat{C}^{(-)}(t)$ respectively, are summed to construct the overall aggregated cost space \hat{C} ,

$$\hat{C}(t) = \hat{C}^{(+)}(t) + \hat{C}^{(-)}(t). \quad (5.38)$$

The multiple directions of aggregation allow for past and future states to influence any given state of the Markov process presented in Figure 5.10, and thus for more information to be factored into the optimum selection.

5.6.3 Optimum GHz Range Selection

Using the aggregated cost $\hat{C}(t)$, the optimum policy $\mathbf{n}_{\text{opt}}(t)$ is then selected such as

$$\mathbf{n}_{\text{opt}}(t) = \underset{\mathbf{n}(t)}{\operatorname{argmin}} \left(\hat{C}(t) \right), \quad (5.39)$$

allowing to determine the corresponding reach $r_{\text{opt}}(t)$. The battery level is then updated for the next time step t using the storage model (5.13) presented in Section 5.3.4,

$$\begin{aligned} E_{\text{B}}(t) = & \alpha_{\text{B}} E_{\text{B}}(t - \delta_t) + \eta_{\text{B}} (E_{\text{W}}(t) + E_{\text{S}}(t)) \\ & - \frac{1}{\eta_{\text{B}}} (E_{\text{GHz}}(r_{\text{opt}}(t)) + E_{\text{UHF}} + E_{\text{BS}} + E_{\text{backhaul}}), \end{aligned} \quad (5.40)$$

using the selected reach $r_{\text{opt}}(t)$ to compute the GHz radio power consumption E_{GHz} , as detailed in Section 5.3.3, the coefficient α_{B} accounting for the battery self discharge and η_{BS} the efficiency of the power conversion systems. The algorithm is then ready for the next time step $t + \delta_t$, and building the new associated Markov process.

5.7 Load/Energy Balanced Approach: Results

This section presents the results of the load/energy balanced approach described in Section 5.5.

5.7.1 Test Scenarios and Methodology

In order to test the performances of the algorithm, simulations with a year worth of randomly generated data are performed using the models described in Section 5.3. Two energy harvesting scenarios are pondered, the first considers the harvesting performances described in Section 5.2, while the second implements a base station equipped with harvesters providing only 25% of the energy output from the first scenario. The value of 25% is chosen empirically using simulation, the aim being to allow the algorithm to work at its limit, while still maintaining a battery level above 10% at all time. This reduced harvesting capacity simulation enabled a better understanding of the behaviours of the algorithm and considers the possibility to reduce the harvesting capacity of future base station designs.

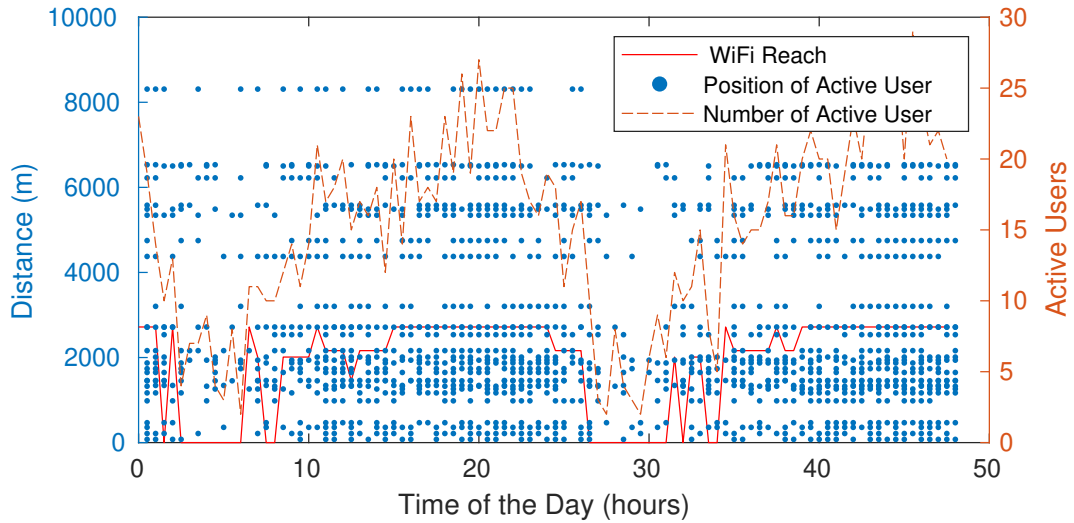


Figure 5.11: Two days simulation in January at full harvesting capacity.

Three metrics are used to judge the algorithm behaviour: the reach, the power consumption of the GHz radio and the number of users assigned to the TVWS network. The reach variation is observed through the day for different month in order to compare the algorithm behaviours under different loads and harvesting conditions; monitoring the power consumption of the GHz radio allows the quantification of the energy saving offered by the use of the breathing algorithm, while observation of the average load of the TVWS network offers a suitable measure of QoS, as the TVWS radio only allows for limited broadband throughput.

5.7.2 Results and Analysis

The metrics, presented in Section 5.7.1, are measured after each decision and averaged on a monthly basis. Figure 5.11 shows the positions of active users as well as the reach for the GHz network selected by the algorithm with respect to those positions over a two-day window. The number of active users confirms that the algorithm behaves as expected by adapting the GHz reach to the user activity, increasing the reach when numerous users are connected to internet and reducing it to a shut-down of the GHz radio when all users can be provided with service by sole mean of the TVWS network. Figure 5.12 presents the hourly average reach of the GHz network of the month of January and July, under the two considered scenario whereby January and July represent month with high and low harvested energy, respectively [3]. The algorithm reduces

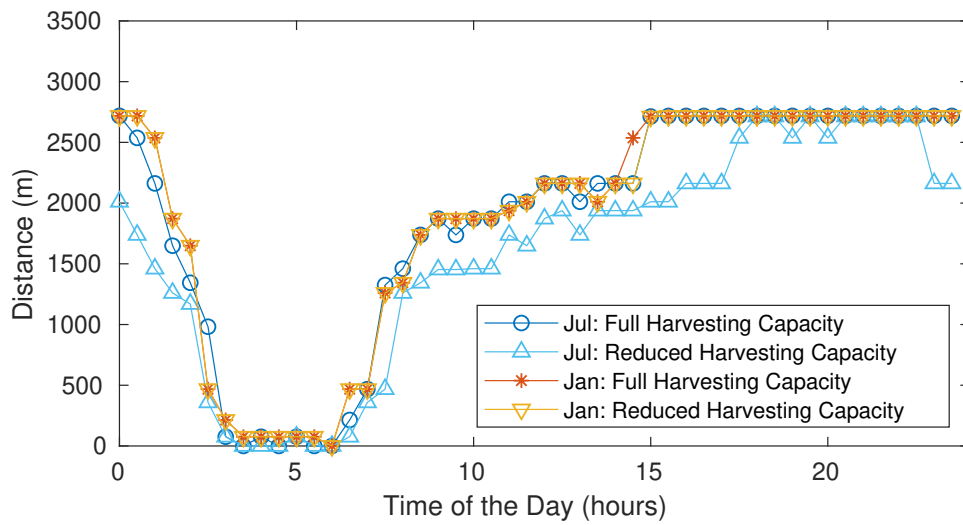


Figure 5.12: Mean hourly GHz network reach on a day in January and July under full and reduced harvesting capacity.

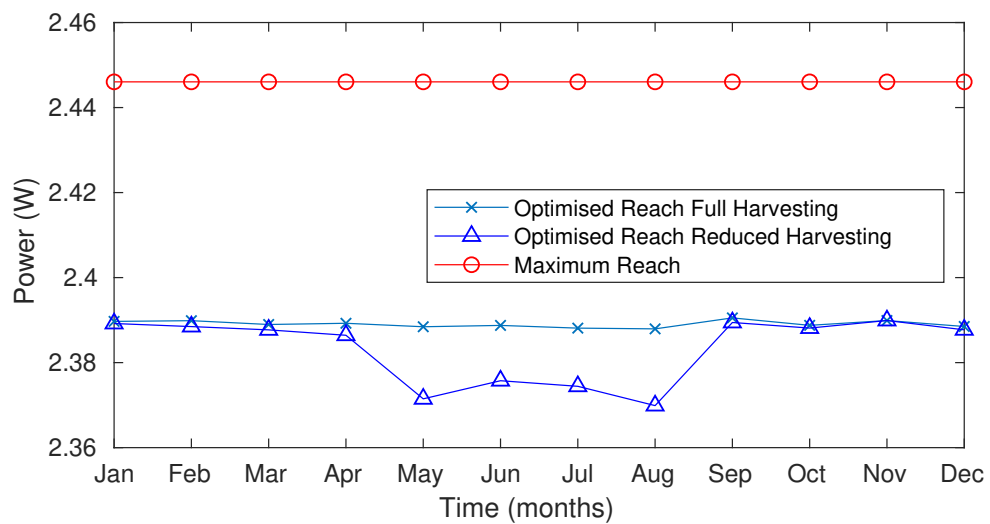


Figure 5.13: Mean GHz radio power consumption.

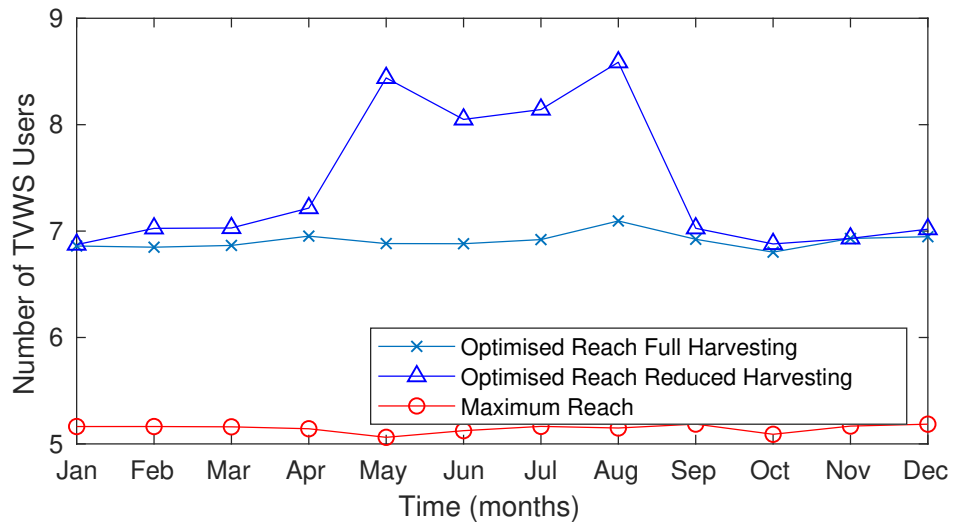


Figure 5.14: Average numbers of TVWS users.

the reach of the GHz radio in low energy condition, this is especially visible for the month of July under reduced harvesting capacity. This behaviour is corroborated by the reduction in power consumption for the GHz radio shown in Figure 5.13, which is linked to the increase in the number of users assigned to the TVWS network as evident from Figure 5.14.

5.8 Load Focused Approach: Results

This section presents the results of the load focused approach described in Section 5.4.

5.8.1 Test Scenarios and Methodology

The load focussed approach of this work pondered several variations in the considered scenario. The algorithm is first submitted to changes in community size, as well as variation in load models and user spatial distribution, presented in Section 5.3.2. Secondly, as in Section 5.7.1, the design of the base station itself is adjusted by changing the energy harvesting capabilities of the solar panels and wind turbine.

As mentioned in Section 5.3.2, previous studies have shown that traffic in rural areas obey to a different model than the typical Maier load model [19]. Simulations are then performed varying community size under the Maier and Tirie models. In a

second set of simulation, two types of spatial distributions are considered, half-normal and Gamma distributions as defined in (5.3) and (5.4) respectively; to facilitate the observation of the influence of the distribution on the results, the simulations are performed using a community of 30 users, under a Ttree type load model, while varying the parameters shown in Table 5.1, leading to the distributions depicted in Figure 5.3 and Figure 5.5.

As the energy harvesting plays an essential part within the algorithm, this work ought to test the approach performance against different base station designs, with various energy harvesting capabilities. To that end both the solar and wind harvesting capacities, as well as the ratio between those two are adjusted. For each of the harvesters, the harvesting capacity varies between 50% and 200%.

Several metrics are introduced, in order to compare the performances of the algorithm when operating in the scenarios above. The battery level and algorithm decision in terms of optimum reach are saved. While the battery level is a good indicator of the algorithm performances, it does not suffice on its own; indeed the optimum solution in terms of energy saving is to switch off the GHz network all together and provide the service solely using the TVWS radio. This configuration would however not allow for a satisfactory QoS during the hours of high traffic; to check that the algorithm does not have a tendency to use this easy solution, a load-related metric is introduced. This load factor $\nu(t)$ of the TVWS network is defined as

$$\nu(t) = \frac{N_{\text{UHF}}(t)}{N_{\text{UHF,max}}}. \quad (5.41)$$

This ratio allows to determine what proportion of active users receive a worse than expected QoS.

For each of the scenarios, numerous (between 50 and 100) one-year-long simulations are performed, thus providing a large amount of data points to extract statistically viable conclusions. Mean values of the metrics are displayed with an 90% percentiles range, allowing a better understanding of how the algorithm performs. The results are plotted together with metrics for scenarios both considering a TVWS only base station and a base station with the WiFi set at full power continuously. With respect to the battery level, the algorithm performances are measured using the 10% lower percentile; indeed this value represents a better metric as it is more representative of the lower charge the battery would ever reach, while the mean tends to smooth away

those extremes, and with it the ability of the metric to represent the likelihood of a failure of the base station.

5.8.2 Result and Analysis

Community Size

For this set of simulation, the size of the community varied between $N = 20$ and $N = 50$ users, under two load models, the Maier model and one based of measurement on the Isle of Tiree [19], as presented in Section 5.3.2. The Maier model, as well as being a standard model, submits the system to higher loads, pushing the algorithm to its limits; while the more realistic Tiree model allows for a smoother load profile, closer to the actual environment of the base station.

The algorithm tends to perform better for the smaller community, compared to bigger size communities, with battery levels closer to a TVWS-only base station. The performance metrics related to small communities are shown in Figures 5.15a and 5.15b, which shows the use of the optimisation algorithm improving on the lower 10% percentile of the battery level compared to a base station with a fixed WiFi reach set at maximum power. Larger communities are depicted in Figures 5.15g and 5.15h, which reflect scenarios in which the use of the optimisation algorithm seems to improve the battery level only marginally, with a 10% lower percentile very similar to those of a base station using a WiFi radio set at full power.

However, the algorithm produces lower overload compared to a TVWS only base station under high load scenarios, with the algorithm performing better under the Maier model, for which the mean load level and traffic peak are higher than with the Tiree model, as shown in Figure 5.16 where the algorithm smooths the impact of the traffic peak under a Maier model than the Tiree one. This behaviour is due to the fact that small communities lead to a compacter cost space and smaller and more discontinuous cost values, this increases the impact of the transition penalty functions and thus reducing the smoothness of the aggregated cost space, leading to the selection of sub-optimum reach values. The main consequence is that the algorithm is more likely to overload the TVWS network in low population communities, as the reach selection process does not benefit from the smoothness of larger cost spaces.

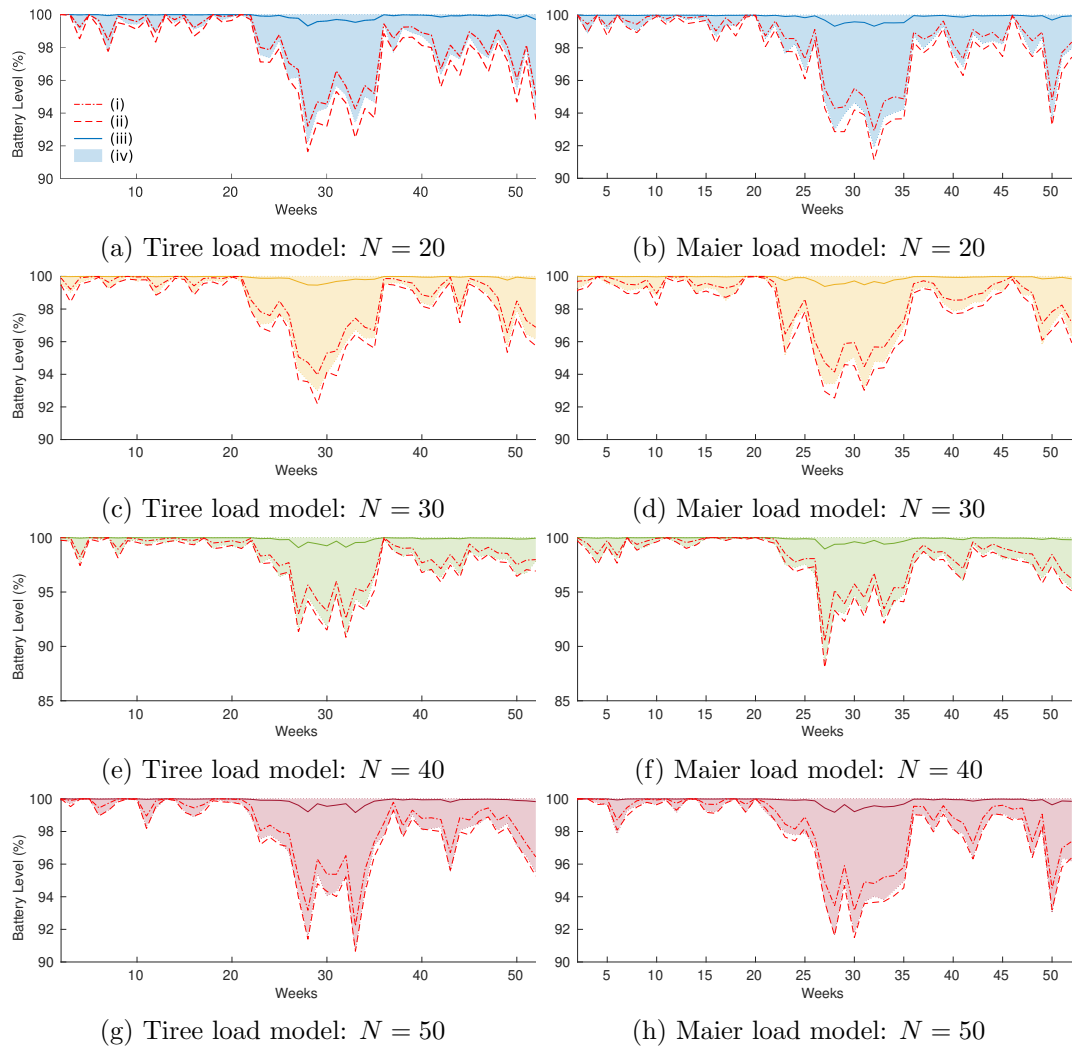


Figure 5.15: Community size: battery level, (i) 10% lower percentile with a TVWS only base station, (ii) lower percentile with the WiFi network at full power, (iii) mean battery level under optimisation and (iv) 90% percentiles under optimisation.

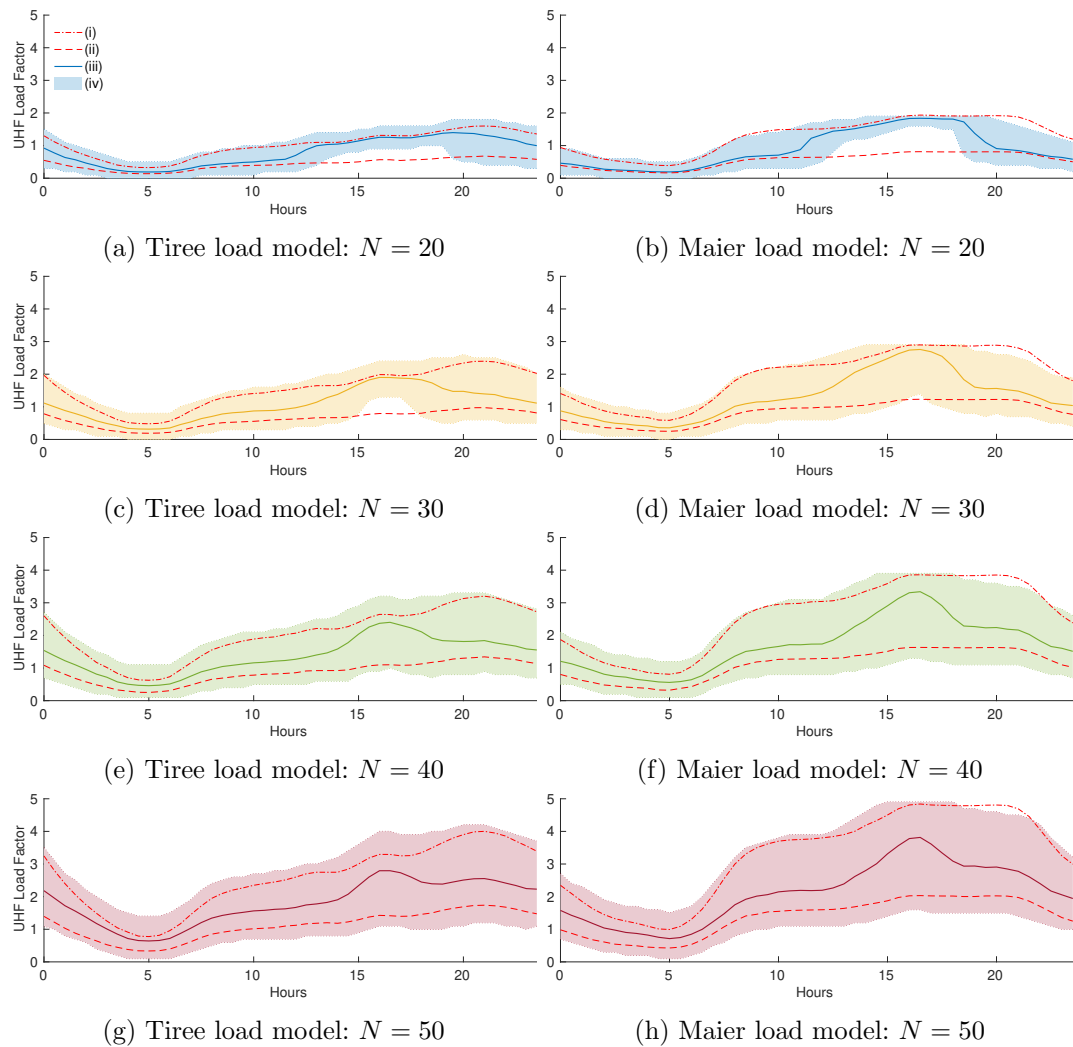


Figure 5.16: Community size: TVWS network load factor $\nu(t)$ over the course of a day, (i) 90% upper percentile with a TVWS only base station, (ii) 90% upper percentile with the WiFi network at full power, (iii) mean under optimisation and (iv) 90% percentiles under optimisation.

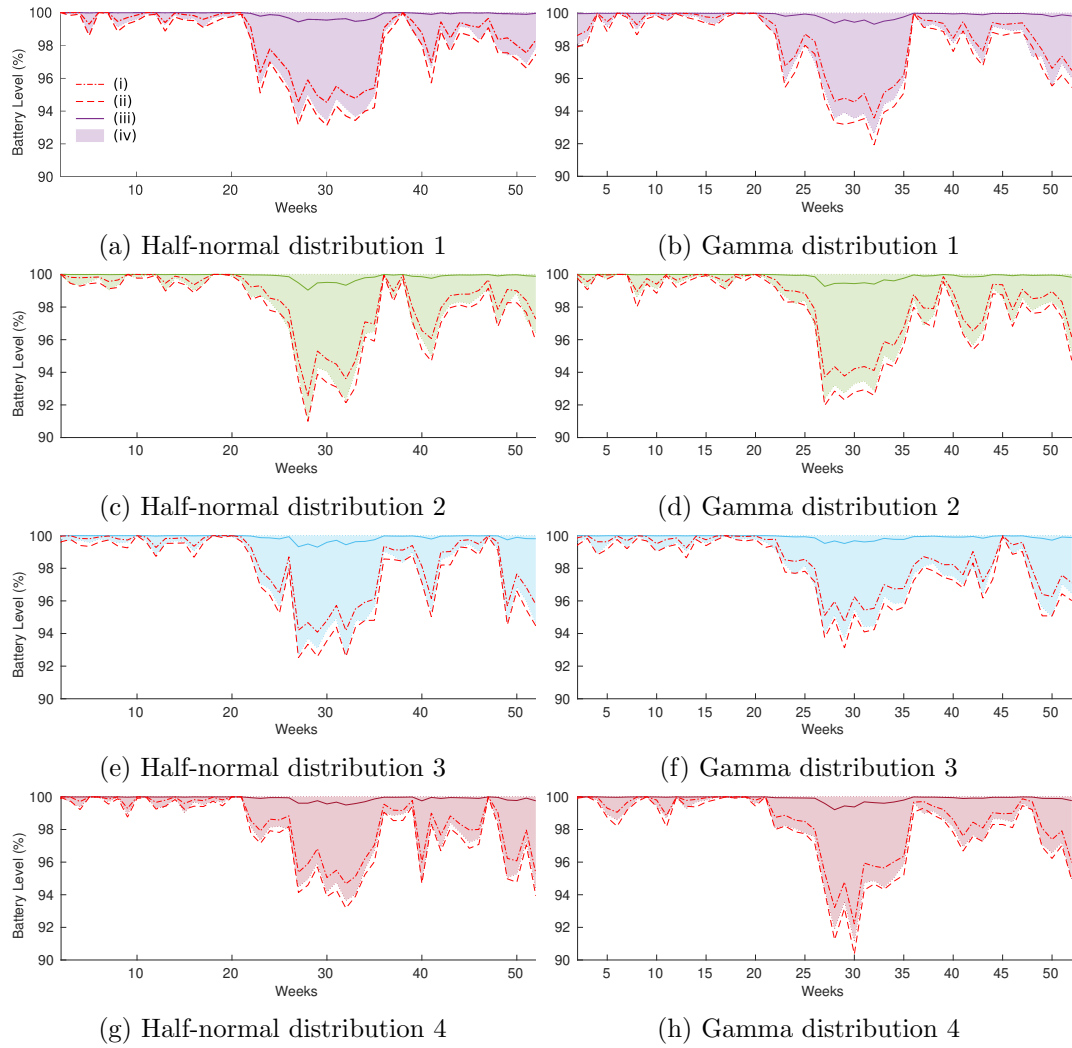


Figure 5.17: User distributions: battery level, (i) 10% lower percentile with a TVWS only base station, (ii) lower percentile with the WiFi network at full power, (iii) mean battery level under optimisation and (iv) 90% percentiles under optimisation.

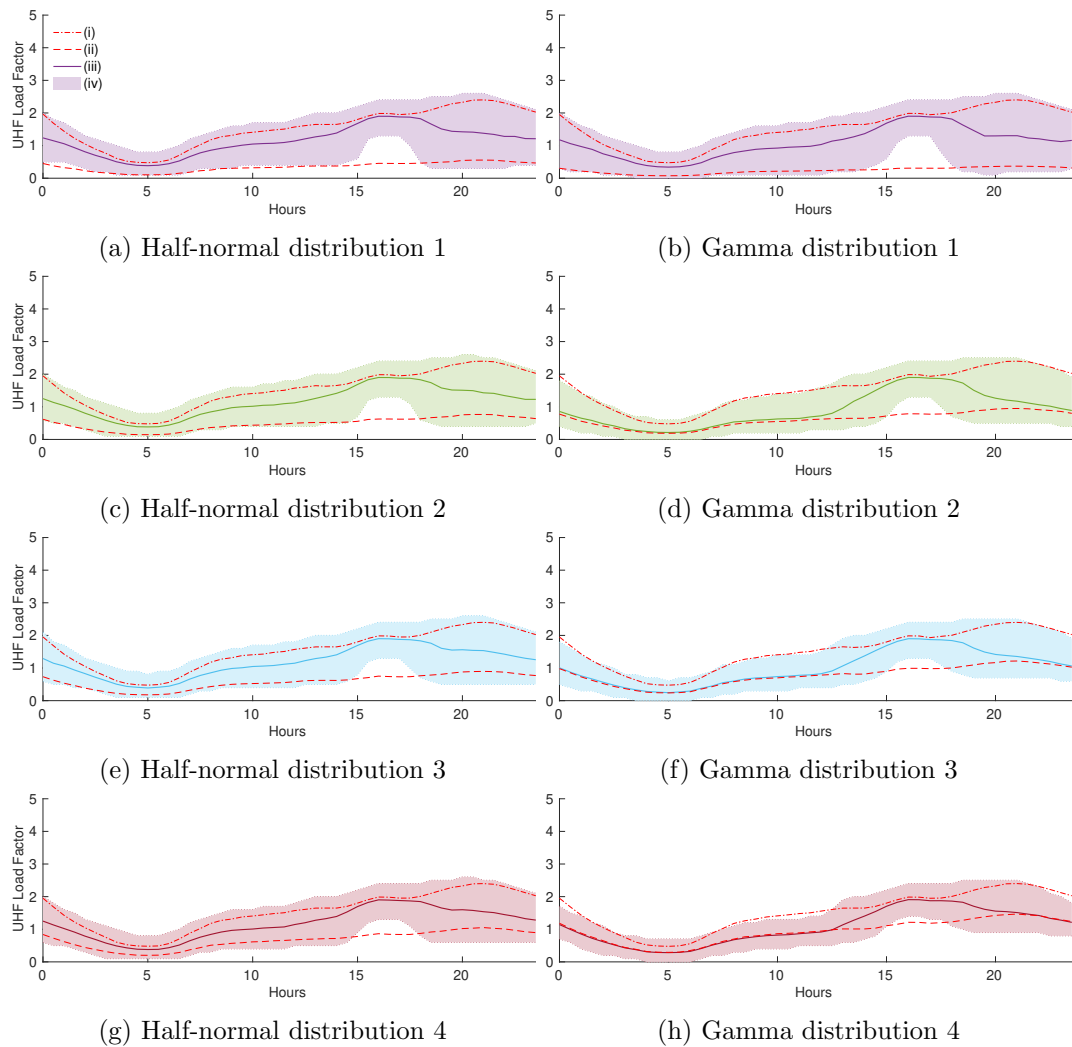


Figure 5.18: User distributions: evolution of the TVWS network load factor $\nu(t)$ over the course of a day, (i) 90% upper percentile with a TVWS only base station, (ii) 90% upper percentile with the WiFi network at full power, (iii) mean under optimisation and (iv) 90% percentiles under optimisation.

User Distribution Shape

This section elaborates on the impact of the spatial distribution of users on the performance of the algorithm. Figure 5.17 shows the strong influence of the shape of the spatial distribution of the users; more specifically the main parameter affecting the algorithm behaviour is the location of the bulk of the users with respect to the base station, with half-normal distributions seeing most users next to the base station, while Gamma distributions locates most users at a given distance from the base station.

The algorithm tends to select less energy efficient policies when presented with Gamma distributions of user, it however performs significantly better in terms of TVWS overload. Indeed the algorithm maintains a similar QoS to a configuration in which the WiFi network is set at full power, apart from the mid-afternoon during which the algorithm tends to overload the TVWS network in order to save energy for the evening traffic peak, which often correspond to an energy harvesting low, as shown in Figure 5.18.

Harvesters Performances

This work uses a conservative approach in terms of energy usage, this reduces the stress on the algorithm and allows a focus on the load while maintaining good performance under the initial design presented in Section 5.2.2. Testing under higher and lower energy harvesting scenarios, as explored in Section 5.7, permits a better understanding of the algorithm behaviour. The results shown in Figure 5.19 confirm the predominance of the wind turbine as the most reliable source of energy, shown by the lower variance in results in high wind harvesting conditions and as highlighted in the models presented Section 5.3.4.

As the cost function of the algorithm is based on the load balance, it tends to produce the same overload profiles when subjected to a similar loads, independently of the available power, see Figure 5.20. This is amplified by the fact that the WiFi radio power consumption variations are relatively small compared to the overall power consumption of the base station. However in most extreme case, like in low energy harvesting scenarios, shown in Figure 5.19b, the algorithm tends to save energy compared to a base station with the WiFi radio at full power.

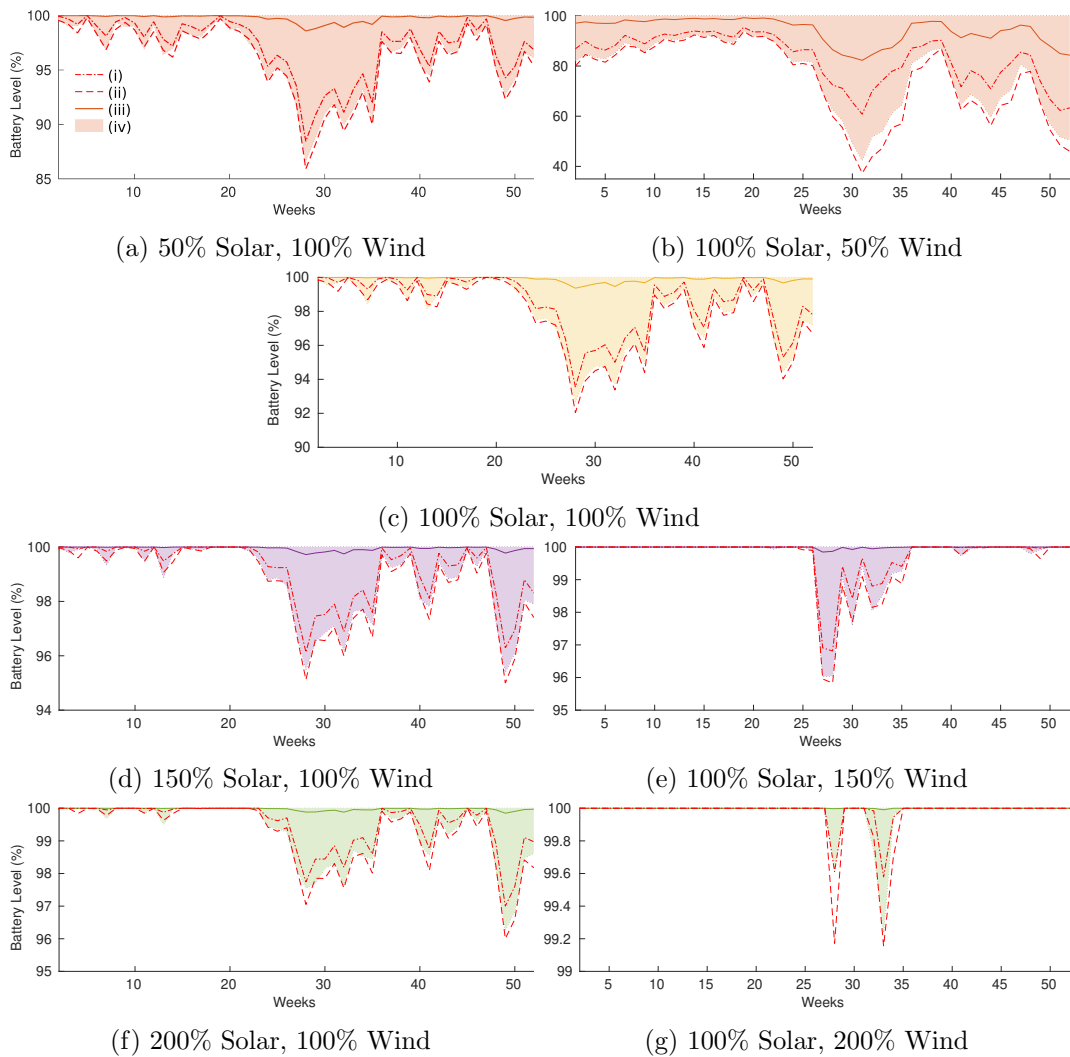


Figure 5.19: Harvesters performances: battery level, (i) 10% lower percentile with a TVWS only base station, (ii) lower percentile with the WiFi network at full power, (iii) mean battery level under optimisation and (iv) 90% percentiles under optimisation.

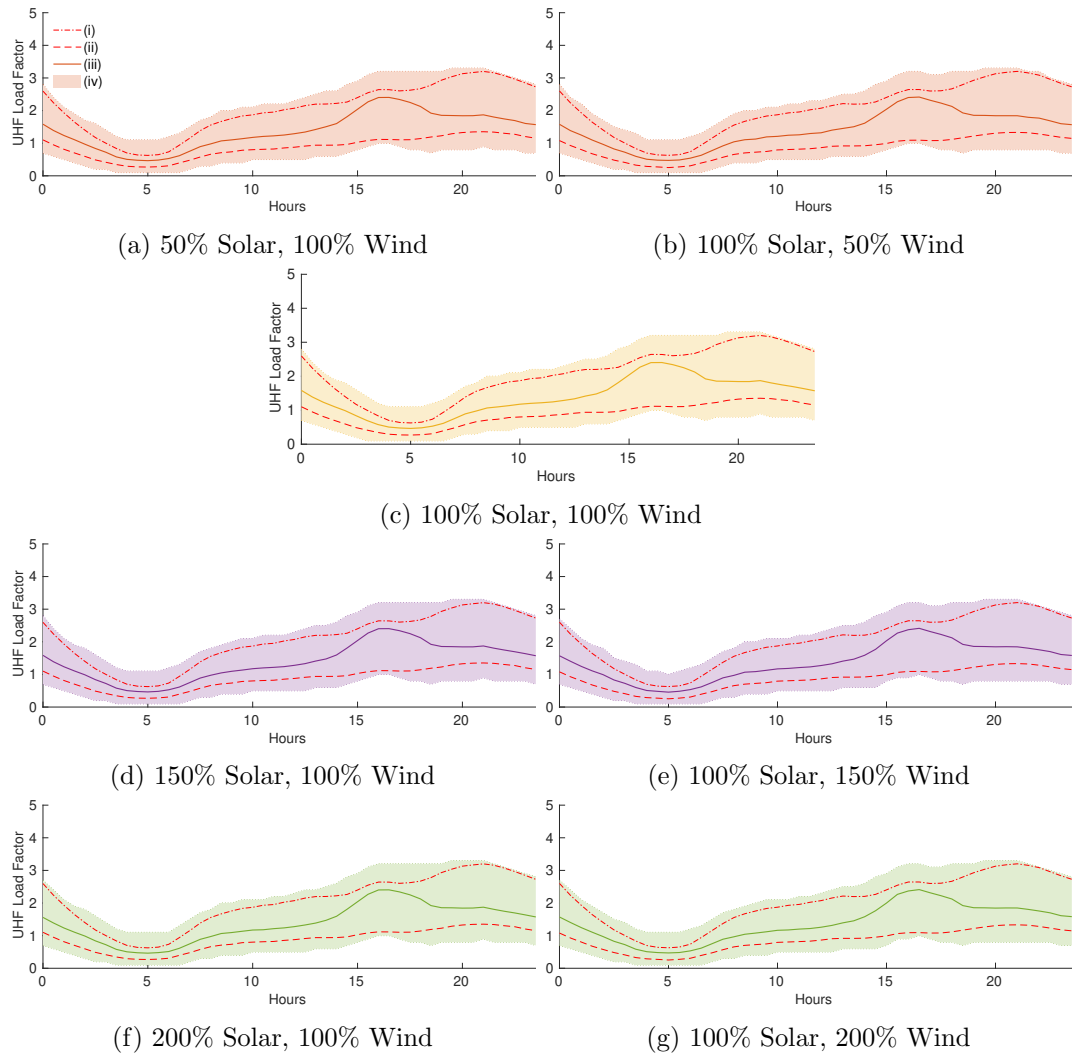


Figure 5.20: Harvesters performances: evolution of the TVWS network load factor $\nu(t)$ over the course of a day, (i) 90% upper percentile with a TVWS only base station, (ii) 90% upper percentile with the WiFi network at full power, (iii) mean under optimisation and (iv) 90% percentiles under optimisation.

5.9 Chapter Summary and Conclusions

This chapter presented two approaches to a load balancing problem for energy harvesting multi-network base station under energy constraints. We considered a load-oriented formulation of the optimisation problem and a more balanced approach using a linear combination of cost functions associated with load and energy performances of the base station, increasing the impact of the energy level on the decision. After providing details about the various models related to rural broadband off-grid wireless base stations, we reformulated the problems to enable a dynamic programming-based optimisation. The resulting algorithms were submitted to multiple scenario variations, allowing to highlight the advantages and drawbacks of each approach and comparing the algorithm performance using metrics based on battery level and TVWS network load.

Such resource management allows together with alterations to the baseband signal processing, such as the ones presented in Chapters 3 and 4, can improve the energy efficiency of base stations. This improvement of energy efficiency is especially critical in energy harvesting communication network, where the power supply is limited.

Chapter 6

Conclusions & Future Work

6.1 Thesis Summary

As detailed in Chapters 1 and 2, broadband access can be challenging in rural areas, mainly because of the large investments required to deploy typical broadband technologies and the fact that those investment are not balanced by large number of users. Previous studies [14–20] introduced wireless base station as suitable solutions for rural broadband access. Furthermore, in a world where the environmental impact of information and communications technology (ICT) is growing, there is a need for energy efficient communication networks. A proposed solution is the introduction of renewable energy harvesters. This thesis in the context of the sustainable cellular network harvesting ambient energy (SCAVENGE) project aimed to address some of the challenges related to the context above.

To this end, in this thesis, we presented further studies of the design of energy harvesting base stations for rural broadband access, by focussing at first on the software defined radio (SDR) implementation of baseband unit signal processing for energy efficient TV white space (TVWS) transceivers, followed by the development of optimisation algorithms for the management of energy harvesting multi-radios base stations.

6.1.1 FFT Size Optimisation for FBMC Systems

In Chapter 3, we provided a new approach to the design and field programmable gates array (FPGA) implementation of oversampled filter-bank multi-carrier (FBMC) systems for TVWS transmission, by moving away from the standard power-of-two fast Fourier transform (FFT) and considering a 40-point mixed-radix FFT. This approach has proven to be both less costly in terms of area and more energy efficient by 6.7% when compared to previous designs. In a complete transceiver system, our approach

might prove even more advantageous, as systems upstream (e.g. stage 1 in Figure 2.9) of the FBMC system in the receiver would run at a sampling frequency 30% lower than with a 64-points FFT system.

6.1.2 Per-Band Equalisation for Oversampled FBMC Systems

We introduced, in Chapter 4, an equalisation technique for oversampled FFT-modulated FBMC. Different from orthogonal frequency-division multiplexing (OFDM), FBMC systems allow for per-channel equalisation. The equaliser is based on the concurrent use of a constant modulus (CM) and a decision directed (DD) process in a fractionally-space equaliser (FSE) structure. This approach allowed for a better equalisation than a standard CM, while leading to lower implementation cost on FPGA, and improved power consumption compared to other approaches.

6.1.3 Multi-Radio Access Network Assignment

In Chapter 5, we presented two approaches to the user assignment problem for an off-grid wireless base stations, with the problem formulation focussed on a cost associated with the load of the TVWS network in one instance, while in the second instance the cost is associated with the load and energy usage of the base station. The algorithms were submitted to several variation of scenario, presented in Chapter 5, showing that the use of the designed user assignment optimisation schemes can improve both energy efficiency and quality of service (QoS), compared to an unmanaged system.

6.2 Future Work

While this thesis addressed some of the challenges related to the implementation of wireless off-grid base station for rural broadband access, several topics remained unexplored and further research and development work can be performed to improve on the proposed design. This section gives some general research and exploration directions.

On the subject of the design of baseband units for TVWS communications, more variation in the design of the FBMC system can be considered; such variation could include FBMC-offset-quadrature amplitude modulation (OQAM) [72, 73]. Work to produce a working prototype covering the full TV spectrum would require to use a high performance SDR platform with analogue-to-digital converters (ADCs) and digital-to-analogue converters (DACs) able to convert up to beyond 40 TV channels. Another approach would be to down-convert the received signal directly as theorised in [54].

For the multi-network optimisation, there are many opportunities for further investigations, variations in both scenarios and solving techniques can be considered. Preliminary studies have brought us to consider that solving techniques such as dynamic programming [115] to oppose to the belief propagation technique previously presented in [28], but other techniques such as convex optimisation could be explored. While our work considers a cost function based on power consumption and use a bandwidth constrain, multi-objective optimisation can be used to provide a finer control on the balance between user bandwidth and power consumption. Variation in scenario could consider the use of more networks or different access technologies.

One could also take the optimisation one step further, by allowing the base station management algorithm to reconfigure part of the baseband unit, for example varying the number of running signal processing chains, i.e. the number of Wireless Fidelity (WiFi) or ultra high frequency (UHF) channels used, according to user activity and power input of the base station.

References

- [1] V. Anis, C. Delaosa, L. H. Crockett, and S. Weiss, “Energy-efficient implementation of a wideband transceiver system with per-band equalisation and synchronisation,” in *2018 IEEE Wireless Communications and Networking Conference*, (Barcelona, Spain), pp. 1–6, Apr. 2018.
- [2] V. Anis, J. Guo, S. Weiss, and L. Crockett, “FPGA Implementation of a TVWS Up- And Downconverter Using Non-Power-of-Two FFT Modulated Filter Banks,” in *2019 27th European Signal Processing Conference (EUSIPCO 2019)*, Sept. 2019.
- [3] V. Anis and S. Weiss, “Multi-Radio Access Network Assignment Using Dynamic Programming,” in *The 27th International Conference on Software, Telecommunications and Computer Networks (SoftCOM 2019)*, Sept. 2019.
- [4] Scavenge-Consortium, *D2.1-WP2 Energy Models: Intermediate Report*. Feb. 2018.
- [5] Scavenge-Consortium, *D2.2-WP2 Energy Models: Final Report*. Dec. 2019.
- [6] Scavenge-Consortium, *D4.1-WP4 Resources Optimisation: Intermediate Report*. Feb. 2018.
- [7] Scavenge-Consortium, *D4.2-WP4 Resources Optimisation– Final Report*. Aug. 2019.
- [8] L. Hilty and B. Aebischer, eds., *ICT Innovations for Sustainability*. Advances in Intelligent Systems and Computing, Springer International Publishing, 2015.
- [9] International Telecommunication Union (ITU), *Measuring Digital Development Facts and Figures 2020*. ITU Publications, 2020.
- [10] OfCom, “UK Home Broadband Performance: The performance of fixed-line broadband delivered to UK residential consumers,” *Research Report*, p. 94, 2018.

- [11] J. Mosenthal, B. Nleya, and N. Manthoko, "Broadband / future generation network services deployment in rural and remote areas," in *2009 2nd International Conference on Adaptive Science Technology (ICAST)*, pp. 128–132, Jan. 2009.
- [12] J. L. Riding, J. C. Ellershaw, A. V. Tran, L. J. Guan, and T. Smith, "Economics of broadband access technologies for rural areas," in *2009 Conference on Optical Fiber Communication - Includes Post Deadline Papers*, pp. 1–3, Mar. 2009.
- [13] OfCom, "Next Generation Access Glossary," tech. rep., Sept. 2008.
- [14] D. Zagar and V. Krizanovic, "Analyses and comparisons of technologies for rural broadband implementation," in *SoftCOM 2009 - 17th International Conference on Software, Telecommunications Computer Networks*, pp. 292–296, Sept. 2009.
- [15] S. Roberts, P. Garnett, and R. Chandra, "Connecting africa using the TV white spaces: From research to real world deployments," in *The 21st IEEE International Workshop on Local and Metropolitan Area Networks*, pp. 1–6, Apr. 2015.
- [16] A. Haider, R. Rahman, O. F. Noor, F. Alam, and R. M. Huq, "Towards an IEEE 802.22 (WRAN) based wireless broadband for rural Bangladesh — Antenna design and coverage planning," in *2017 International Conference on Electrical, Computer and Communication Engineering (ECCE)*, pp. 109–114, Feb. 2017.
- [17] D. Espinoza and D. Reed, "Wireless technologies and policies for connecting rural areas in emerging countries: A case study in rural Peru," *Digital Policy, Regulation and Governance*, Aug. 2018.
- [18] A. Singh, K. K. Naik, and C. R. S. Kumar, "UHF TVWS operation in Indian scenario utilizing wireless regional area network for rural broadband access," in *2016 International Conference on Next Generation Intelligent Systems (ICNGIS)*, pp. 1–6, Sept. 2016.
- [19] C. McGuire, M. R. Brew, F. Darbari, G. Bolton, A. McMahan, D. H. Crawford, S. Weiss, and R. W. Stewart, "HopScotch-a low-power renewable energy base station network for rural broadband access," *EURASIP Journal on Wireless Communications and Networking*, vol. 2012, no. 1, pp. 1–12, 2012.
- [20] F. Darbari, M. Brew, S. Weiss, and W. S. Robert, "Practical aspects of broadband access for rural communities using a cost and power efficient multi-hop/relay network," in *2010 IEEE Globecom Workshops*, pp. 731–735, Dec. 2010.

- [21] C. McGuire and S. Weiss, "Power-optimised multi-radio network under varying throughput constraints for rural broadband access," in *21st European Signal Processing Conference (EUSIPCO 2013)*, pp. 1–5, Sept. 2013.
- [22] OfCom, "Digital dividend: Cognitive access consultation on licence-exempting cognitive devices using interleaved spectrum," tech. rep., Feb. 2009.
- [23] Ofcom, "Decision to make the 700 MHz band available for mobile data - statement," tech. rep., Nov. 2014.
- [24] G. Schmitt, "The Green Base Station," in *4th International Telecommunication - Energy Special Conference*, pp. 1–6, May 2009.
- [25] J. Lorincz and I. Bule, "Renewable Energy Sources for Power Supply of Base Station Sites," *International Journal of Business Data Communications and Networking (IJBDCN)*, vol. 9, no. 3, pp. 53–74, 2013.
- [26] K. Samdanis, P. Rost, A. Maeder, M. Meo, and C. Verikoukis, *Green Communications: Principles, Concepts and Practice*. John Wiley & Sons, 2015.
- [27] F. Ahmed, M. Naeem, W. Ejaz, M. Iqbal, and A. Anpalagan, "Resource management in cellular base stations powered by renewable energy sources," *Journal of Network and Computer Applications*, vol. 112, pp. 1–17, June 2018.
- [28] C. McGuire and S. Weiss, "Multi-radio network optimisation using Bayesian belief propagation," in *2014 22nd European Signal Processing Conference (EUSIPCO)*, pp. 421–425, Sept. 2014.
- [29] A. Goldsmith, *Wireless Communications*. New York, NY, USA: Cambridge University Press, 2005.
- [30] O. Holland, S. Ping, A. Aijaz, J. M. Chareau, P. Chawdhry, Y. Gao, Z. Qin, and H. Kokkinen, "To white space or not to White Space: That is the trial within the Ofcom TV White Spaces pilot," in *2015 IEEE International Symposium on Dynamic Spectrum Access Networks (DySPAN)*, pp. 11–22, Sept. 2015.
- [31] Y. Hou and D. I. Laurenson, "Energy Efficiency of High QoS Heterogeneous Wireless Communication Network," in *2010 IEEE 72nd Vehicular Technology Conference - Fall*, pp. 1–5, Sept. 2010.
- [32] X. Zhang, Z. Su, Z. Yan, and W. Wang, "Energy-Efficiency Study for Two-tier Heterogeneous Networks (HetNet) Under Coverage Performance Constraints," *Mob. Netw. Appl.*, vol. 18, pp. 567–577, Aug. 2013.

- [33] “Software Defined Radios,” in *Green Software Defined Radios*, Series on Integrated Circuits and Systems, pp. 15–25, Springer, Dordrecht, 2009.
- [34] F. K. Jondral, “Software-defined Radio: Basics and Evolution to Cognitive Radio,” *EURASIP J. Wirel. Commun. Netw.*, vol. 2005, pp. 275–283, Aug. 2005.
- [35] MathWorks, “Hardware-Software Co-Design - MATLAB & Simulink.” https://uk.mathworks.com/help/hdlcoder/hardware-software-codesign-1.html?searchHighlight=hardware%20software&s_tid=srchtitle, 2020.
- [36] Xilinx, “UG892: Vivado design flows-overview,” 2020.
- [37] N. Piovesan and P. Dini, “Optimal direct load control of renewable powered small cells: A shortest path approach,” *Internet Technology Letters*, vol. 1, Jan. 2018.
- [38] O. Holland, S. Ping, N. Sastry, P. Chawdhry, J. M. Chareau, J. Bishop, H. Xing, S. Taskafa, A. Aijaz, M. Bavaro, P. Viaud, T. Pinato, E. Anguili, M. R. Akhavan, J. McCann, Y. Gao, Z. Qin, Q. Zhang, R. Knopp, F. Kaltenberger, D. Nussbaum, R. Dionisio, J. Ribeiro, P. Marques, J. Hallio, M. Jakobsson, J. Auranen, R. Ekman, H. Kokkinen, J. Paavola, A. Kivinen, T. Solc, M. Mohorcic, H. N. Tran, K. Ishizu, T. Matsumura, K. Ibuka, H. Harada, and K. Mizutani, “Some Initial Results and Observations from a Series of Trials within the Ofcom TV White Spaces Pilot,” in *2015 IEEE 81st Vehicular Technology Conference (VTC Spring)*, pp. 1–7, May 2015.
- [39] OfCom, “Future use of the 700MHz band,” Sept. 2016.
- [40] S. M. Trimberger, “Three Ages of FPGAs: A Retrospective on the First Thirty Years of FPGA Technology,” *Proceedings of the IEEE*, vol. 103, pp. 318–331, Mar. 2015.
- [41] R. Stewart and L. Crockett, “DSP for FPGA Primer,” *University of Strathclyde. Glasgow*, 2011.
- [42] Xilinx, “7 Series DSP48E1 Slice User Guide (UG479),” p. 58, 2016.
- [43] Xilinx, “Xilinx Power Estimator User Guide,” p. 132, 2020.
- [44] Xilinx, “Vivado Power Analysis Optimization Tutorial (UG997),” 2020.
- [45] Xilinx, “ZC706 Evaluation Board for the Zynq-7000 XC7Z045 SoC User Guide (UG954),” p. 103, 2019.

- [46] Analog Devices, “AD-FMCOMMS4-EBZ User Guide [Analog Devices Wiki].” <https://wiki.analog.com/resources/eval/user-guides/ad-fmcomms4-ebz>.
- [47] Xilinx, “Zynq-7000 SoC Data Sheet: Overview (DS190),” p. 25, 2018.
- [48] Analog Devices, “RF Agile Transceiver: AD9364,” 2014.
- [49] Ettus Research, “USRP N310,” 2020.
- [50] Ettus Research, “USRP N320,” 2020.
- [51] Xilinx, “UltraScale Architecture and Product Data Sheet: Overview (DS890),” p. 50, 2020.
- [52] MathWorks, “HDL Coder Documentation.” https://uk.mathworks.com/help/hdlcoder/index.html?searchHighlight=HDL-coder&s_tid=srchtitle, 2020.
- [53] MathWorks, “Fixed-Point Design - MATLAB & Simulink.” https://uk.mathworks.com/help/dsp/fixed-point-design.html?searchHighlight=fixed%20point%20toolbox&s_tid=srchtitle, 2020.
- [54] R. A. Elliot, M. A. Enderwitz, K. Thompson, L. H. Crockett, S. Weiss, and R. W. Stewart, “Wideband TV White Space Transceiver Design and Implementation,” *IEEE Transactions on Circuits and Systems II: Express Briefs*, vol. 63, pp. 24–28, Jan. 2016.
- [55] P. P. Vaidyanathan, “Multirate digital filters, filter banks, polyphase networks, and applications: A tutorial,” *Proceedings of the IEEE*, vol. 78, pp. 56–93, Jan. 1990.
- [56] W. Kester, “Taking the Mystery out of the Infamous Formula, ”SNR = 6.02N + 1.76dB,” and Why You Should Care,” p. 7, 2009.
- [57] S. Weiss and R. Stewart, “Fast implementation of oversampled modulated filter banks,” in *3rd European DSP Education and Research Conference*, 2000.
- [58] S. Weiss and R. Stewart, “Fast implementation of oversampled modulated filter banks,” *Electronics Letters*, vol. 36, pp. 1502–1503, Aug. 2000.
- [59] R. A. Elliot, M. A. Enderwitz, F. Darbari, L. H. Crockett, S. Weiss, and R. W. Stewart, “Efficient TV white space filter bank transceiver,” in *20th European Signal Processing Conference*, pp. 1079–1083, Aug. 2012.

- [60] M. Harteneck, S. Weiss, and R. W. Stewart, "Design of near perfect reconstruction oversampled filter banks for subband adaptive filters," *IEEE Transactions on Circuits and Systems II: Analog and Digital Signal Processing*, vol. 46, pp. 1081–1085, Aug. 1999.
- [61] S. J. Shellhammer, A. K. Sadek, and W. Zhang, "Technical challenges for cognitive radio in the TV white space spectrum," in *2009 Information Theory and Applications Workshop*, pp. 323–333, Feb. 2009.
- [62] J. Ahn and H. S. Lee, "Frequency domain equalisation of OFDM signals over frequency nonselective Rayleigh fading channels," *Electronics Letters*, vol. 29, pp. 1476–1477, Aug. 1993.
- [63] M. Speth, F. Classen, and H. Meyr, "Frame synchronization of OFDM systems in frequency selective fading channels," in *1997 IEEE 47th Vehicular Technology Conference. Technology in Motion*, vol. 3, (Phoenix, AZ, USA), pp. 1807–1811, IEEE, 1997.
- [64] L. Hanzo, C. H. Wong, and M. S. Yee, *Adaptive Wireless Transceivers: Turbo-Coded, Turbo-Equalised and Space-Time Coded TDMA, CDMA and OFDM Systems*. John Wiley & Sons, Mar. 2002.
- [65] K. Muralidhar, L. K. Hung, and Y. C. Liang, "Low-Complexity Equalisation Methods for OFDM Systems in Doubly Selective Channels," in *VTC Spring 2008 - IEEE Vehicular Technology Conference*, pp. 683–687, May 2008.
- [66] D. T. M. Slock, "Blind fractionally-spaced equalization, perfect-reconstruction filter banks and multichannel linear prediction," in *1994 IEEE International Conference on Acoustics, Speech, and Signal Processing, 1994. ICASSP-94*, vol. iv, pp. IV/585–IV/588 vol.4, Apr. 1994.
- [67] L. Vandendorpe, L. Cuvelier, F. Deryck, J. Louveaux, and O. van de Wiel, "Fractionally spaced linear and decision-feedback detectors for transmultiplexers," *IEEE Transactions on Signal Processing*, vol. 46, pp. 996–1011, Apr. 1998.
- [68] A. A. Nagy and S. Weiss, "Comparison of different filter-bank based multicarrier systems with fractionally spaced equalisation," in *11th IMA International Conference on Mathematics in Signal Processing*, pp. 1–4, GBR: Institute of Mathematics and its Applications, Dec. 2016.
- [69] A. Nagy and S. Weiss, "Synchronisation and equalisation of an FBMC/OQAM system by a polynomial matrix pseudo-inverse," in *2017 IEEE International Sym-*

- posium on Signal Processing and Information Technology (ISSPIT)*, pp. 311–316, Dec. 2017.
- [70] A. Nagy and S. Weiss, “Channel Equalisation of a MIMO FBMC/OQAM System Using a Polynomial Matrix Pseudo-Inverse,” in *2018 IEEE 10th Sensor Array and Multichannel Signal Processing Workshop (SAM)*, pp. 568–572, July 2018.
- [71] Y. J. Harbi and A. G. Burr, “On ISI and ICI cancellation for FBMC/OQAM system using iterative decoding and ML detection,” in *2016 IEEE Wireless Communications and Networking Conference*, pp. 1–6, Apr. 2016.
- [72] P. Siohan, C. Siclet, and N. Lacaille, “Analysis and design of OFDM/OQAM systems based on filterbank theory,” *IEEE Transactions on Signal Processing*, vol. 50, pp. 1170–1183, May 2002.
- [73] J. Nadal, C. A. Nour, A. Baghdadi, and H. Lin, “Hardware prototyping of FBMC/OQAM baseband for 5G mobile communication,” in *Proceedings of the 2014 25th IEEE International Symposium on Rapid System Prototyping, New Delhi, India*, vol. 1617, p. 7277, 2014.
- [74] A. Gilloire and M. Vetterli, “Adaptive filtering in subbands with critical sampling: Analysis, experiments, and application to acoustic echo cancellation,” *IEEE transactions on signal processing*, vol. 40, no. 8, pp. 1862–1875, 1992.
- [75] X. Mestre and D. Gregoratti, “A parallel processing approach to filterbank multicarrier MIMO transmission under strong frequency selectivity,” in *2014 IEEE International Conference on Acoustics, Speech and Signal Processing (ICASSP)*, pp. 8078–8082, May 2014.
- [76] J. Treichler and B. Agee, “A new approach to multipath correction of constant modulus signals,” *IEEE Transactions on Acoustics, Speech, and Signal Processing*, vol. 31, pp. 459–472, Apr. 1983.
- [77] I. Fijalkow, C. E. Manlove, and C. R. Johnson, “Adaptive fractionally spaced blind CMA equalization: Excess MSE,” *IEEE Transactions on Signal Processing*, vol. 46, pp. 227–231, Jan. 1998.
- [78] I. Fijalkow, A. Touzni, and J. R. Treichler, “Fractionally spaced equalization using CMA: Robustness to channel noise and lack of disparity,” *IEEE Transactions on Signal Processing*, vol. 45, pp. 56–66, Jan. 1997.

- [79] A. Heřmánek, J. Schier, and P. Regalia, “Architecture design for FPGA implementation of finite interval CMA,” in *2004 12th European Signal Processing Conference*, pp. 2039–2042, Sept. 2004.
- [80] F. C. C. D. Castro, M. C. F. D. Castro, and D. S. Arantes, “Concurrent blind deconvolution for channel equalization,” in *ICC 2001. IEEE International Conference on Communications. Conference Record (Cat. No.01CH37240)*, vol. 2, pp. 366–371 vol.2, June 2001.
- [81] M. Rupp and R. Frenzel, “Analysis of LMS and NLMS algorithms with delayed coefficient update under the presence of spherically invariant processes,” *IEEE Transactions on Signal Processing*, vol. 42, no. 3, pp. 668–672, 1994.
- [82] R. C. Gunning and H. Rossi, *Analytic Functions of Several Complex Variables*. Prentice-Hall, 1965.
- [83] T. Pering, Y. Agarwal, R. Gupta, and R. Want, “CoolSpots: Reducing the Power Consumption of Wireless Mobile Devices with Multiple Radio Interfaces,” in *Proceedings of the 4th International Conference on Mobile Systems, Applications and Services, MobiSys '06*, (New York, NY, USA), pp. 220–232, ACM, 2006.
- [84] J. Miao, Z. Hu, K. Yang, C. Wang, and H. Tian, “Joint Power and Bandwidth Allocation Algorithm with QoS Support in Heterogeneous Wireless Networks,” *IEEE Communications Letters*, vol. 16, pp. 479–481, Apr. 2012.
- [85] O. Galinina, S. Andreev, A. Turlikov, and Y. Koucheryavy, “Optimizing energy efficiency of a multi-radio mobile device in heterogeneous beyond-4G networks,” *Performance Evaluation*, vol. 78, pp. 18–41, Aug. 2014.
- [86] A. Damnjanovic, J. Montojo, Y. Wei, T. Ji, T. Luo, M. Vajapeyam, T. Yoo, O. Song, and D. Malladi, “A survey on 3GPP heterogeneous networks,” *IEEE Wireless Communications*, vol. 18, pp. 10–21, June 2011.
- [87] P. P. Vaidyanathan, “Filter banks in digital communications,” *IEEE Circuits and Systems Magazine*, vol. 1, no. 2, pp. 4–25, 2001.
- [88] C. F. Hsiao, Y. Chen, and C. Y. Lee, “A Generalized Mixed-Radix Algorithm for Memory-Based FFT Processors,” *IEEE Transactions on Circuits and Systems II: Express Briefs*, vol. 57, pp. 26–30, Jan. 2010.
- [89] J. W. Cooley and J. W. Tukey, “An Algorithm for the Machine Calculation of Complex Fourier Series,” *Mathematics of Computation*, vol. 19, no. 90, pp. 297–301, 1965.

- [90] F. Qureshi, M. Garrido, and O. Gustafsson, "Unified architecture for 2, 3, 4, 5, and 7-point DFTs based on Winograd Fourier transform algorithm," *Electronics Letters*, vol. 49, pp. 348–349, Feb. 2013.
- [91] A. Karlsson, J. Sohl, and D. Liu, "Cost-efficient mapping of 3- and 5-point DFTs to general baseband processors," in *2015 IEEE International Conference on Digital Signal Processing*, pp. 780–784, July 2015.
- [92] M. D. Macleod and N. L. Bragg, "Fast hardware implementation of the Winograd Fourier transform algorithm," *Electronics Letters*, vol. 19, pp. 363–365, May 1983.
- [93] M. D. Macleod, "Multiplierless Winograd and prime factor FFT implementation," *IEEE Signal Processing Letters*, vol. 11, pp. 740–743, Sept. 2004.
- [94] J. Löfgren and P. Nilsson, "On hardware implementation of radix 3 and radix 5 FFT kernels for LTE systems," in *2011 NORCHIP*, pp. 1–4, Nov. 2011.
- [95] D. E. Knuth, *The Art of Computer Programming, Volume 2 (3rd Ed.): Seminumerical Algorithms*. USA: Addison-Wesley Longman Publishing Co., Inc., 1997.
- [96] P. Duhamel and M. Vetterli, "Fast fourier transforms: A tutorial review and a state of the art," *Signal Processing*, vol. 19, pp. 259–299, Apr. 1990.
- [97] D. J. Shpak and A. Antoniou, "A generalized Remez method for the design of FIR digital filters," *IEEE Transactions on Circuits and Systems*, vol. 37, pp. 161–174, Feb. 1990.
- [98] S. Weiss, A. P. Millar, R. W. Stewart, and M. D. Macleod, "Performance of Transmultiplexers Based on Oversampled Filter Banks under Variable Oversampling Ratios," in *18th European Signal Processing Conference*, pp. 2181–2185, Aug. 2010.
- [99] S. Weiss, M. Harteneck, and R. Stewart, "On implementation and design of filter banks for subband adaptive systems," in *IEE Colloquium on Digital Filters: An Enabling Technology*, vol. 1998/252, pp. 12/1–12/8, Apr. 1998.
- [100] B. Farhang-Boroujeny, "OFDM Versus Filter Bank Multicarrier," *IEEE Signal Processing Magazine*, vol. 28, pp. 92–112, May 2011.
- [101] P. P. Vaidyanathan, *Multirate Systems and Filter Banks*. Englewood Cliffs: Prentice Hall, 1993.

- [102] T. I. Laakso, V. Valimaki, M. Karjalainen, and U. K. Laine, "Splitting the unit delay [FIR/all pass filters design]," *IEEE Signal Processing Magazine*, vol. 13, pp. 30–60, Jan. 1996.
- [103] R. Johnson, P. Schniter, T. J. Endres, J. D. Behm, D. R. Brown, and R. A. Casas, "Blind equalization using the constant modulus criterion: A review," *Proceedings of the IEEE*, vol. 86, no. 10, pp. 1927–1950, 1998.
- [104] M. Hedef and S. Weiss, "Concurrent constant modulus algorithm and decision directed scheme for synchronous DS-CDMA equalisation," in *Statistical Signal Processing, 2005 IEEE/SP 13th Workshop On*, pp. 203–208, IEEE, 2005.
- [105] M. Brew, F. Darbari, C. McGuire, G. Bolton, S. Weiss, and R. W. Stewart, "A low cost and power efficient TV white space technology solution for future rural broadband access networks," in *2011 IEEE GLOBECOM Workshops (GC Wkshps)*, pp. 1024–1028, Dec. 2011.
- [106] M. Brew, F. Darbari, L. H. Crockett, M. B. Waddell, M. Fitch, S. Weiss, and R. W. Stewart, "UHF white space network for rural smart grid communications," in *2011 IEEE International Conference on Smart Grid Communications (Smart-GridComm)*, pp. 138–142, Oct. 2011.
- [107] G. Maier, A. Feldmann, V. Paxson, and M. Allman, "On Dominant Characteristics of Residential Broadband Internet Traffic," in *Proceedings of the 9th ACM SIGCOMM Conference on Internet Measurement, IMC '09*, (New York, NY, USA), pp. 90–102, ACM, 2009.
- [108] ETSI, "ETSI EN 300 328 V1.8.1 (2012-06) Electromagnetic compatibility and Radio spectrum Matters (ERM); Wideband transmission systems; Data transmission equipment operating in the 2,4 GHz ISM band and using wide band modulation techniques; Harmonized EN covering the essential requirements of article 3.2 of the R&TTE Directive," 2012.
- [109] M. Gulin, M. Vařak, and N. Perić, "Dynamical optimal positioning of a photovoltaic panel in all weather conditions," *Applied Energy*, vol. 108, pp. 429–438, Aug. 2013.
- [110] J. V. Dave, P. Halpern, and H. J. Myers, "Computation of Incident Solar Energy," *IBM Journal of Research and Development*, vol. 19, pp. 539–549, Nov. 1975.
- [111] [climatedata.eu](https://www.climatedata.eu/), "Climate Glasgow - Scotland." <https://www.climatedata.eu/climate.php?loc=ukxx0061&lang=en>, 2019.

- [112] E. Hau and H. Von Renouard, *The Wind Resource*. Springer, 2006.
- [113] T. Burton, N. Jenkins, D. Sharpe, and E. Bossanyi, *Wind Energy Handbook*. John Wiley & Sons, May 2011.
- [114] Lijun Gao, Shengyi Liu, and R. A. Dougal, “Dynamic lithium-ion battery model for system simulation,” *IEEE Transactions on Components and Packaging Technologies*, vol. 25, pp. 495–505, Sept. 2002.
- [115] M. Sniedovich, *Dynamic Programming*. New York, NY, USA: Marcel Dekker, Inc., 1991.

